Jan-Henri Montonen

MODELING AND SYSTEM ANALYSIS OF ELECTRICALLY DRIVEN MECHATRONIC SYSTEMS

ACTA UNIVERSITATIS LAPPEENRANTAENSIS 1056

Jan-Henri Montonen

MODELING AND SYSTEM ANALYSIS OF ELECTRICALLY DRIVEN MECHATRONIC SYSTEMS

Dissertation for the degree of Doctor of Science (Technology) to be presented with due permission for public examination and criticism in the Auditorium of the Student Union House at Lappeenranta–Lahti University of Technology LUT, Lappeenranta, Finland on the 28th of November, 2022, at noon.

Acta Universitatis
Lappeenrantaensis 1056

Supervisors Professor Olli Pyrhönen
LUT School of Energy Systems
Lappeenranta–Lahti University of Technology LUT
Finland

Associate Professor Tuomo Lindh
LUT School of Energy Systems
Lappeenranta–Lahti University of Technology LUT
Finland

Reviewers Professor Stijn Derammelaere
Department of Electromechanics
University of Antwerp
Belgium

Assistant Professor Anton Rassõlkin
School of Engineering
Tallinn University of Technology
Estonia

Opponents Professor Stijn Derammelaere
Department of Electromechanics
University of Antwerp
Belgium

Assistant Professor Anton Rassõlkin
School of Engineering
Tallinn University of Technology
Estonia

ISBN 978-952-335-892-8
ISBN 978-952-335-893-5 (PDF)
ISSN 1456-4491 (Print)
ISSN 2814-5518 (Online)

Lappeenranta–Lahti University of Technology LUT
LUT University Press 2022

Abstract

Jan-Henri Montonen
Modeling and System Analysis of Electrically Driven Mechatronic Systems
Lappeenranta 2022
61 pages
Acta Universitatis Lappeenrantaensis 1056
Diss. Lappeenranta–Lahti University of Technology LUT
ISBN 978-952-335-892-8, ISBN 978-952-335-893-5 (PDF), ISSN 1456-4491 (Print), ISSN 2814-5518 (Online)

A mechatronic system consists of mechanics, power electronics, and control electronics. Thus, designing a mechatronic system requires multidisciplinary knowledge. As the capabilities of microprocessors have increased and prices have declined, various mechanical systems are now controlled by computer-based control systems.

To be able to design a control for such applications, a model of the system is required that describes the phenomena that are being controlled. This doctoral dissertation investigates different levels of complexity for a model of a system consisting of an inverter, an electric motor, and mechanics. In addition, the study addresses the questions of how the models to be applied should be selected and how the selections affect other submodels in the system. The use of multibody-dynamics-based virtual simulation and hardware-in-the-loop simulation as tools for system simulation is also studied. Further, literature references and the publications included in the dissertation are provided as examples. The included publications each report a modeling or control challenge, and different methods are employed to solve these challenges.

It was shown that the selection of the model or the modeling method (such as virtual simulation) was successful in each of the presented cases. The model applied in the cases could describe accurately enough the phenomena that were being studied. Thus, after achieving an accurate enough model of the system, the control problem could be approached. The study also demonstrated that building a model requires an analysis of the system and understanding of the phenomena that are present in the system.

Keywords: simulation, modeling, electric drive, inverter, electric motor, virtual simulation, HIL simulation

Acknowledgments

This work was carried out at the LUT School of Energy Systems at Lappeenranta–Lahti University of Technology LUT, Finland, between 2012 and 2022.

I would like thank ABB Oy for funding the tower crane and rod pump projects, Visedo Oy (now Danfoss Editron) for funding the Smart Drives project, and Wärtsilä Oy for funding the FESSMI and INTENS projects. These projects made the work related to this doctoral dissertation possible.

I would also like thank Professor Olli Pyrhönen and Associate Professor Tuomo Lindh for their supervision and guidance during this project, and Associate Professor Hanna Niemelä for editing the English language of the dissertation and the included publications.

I would also like thank my co-workers, especially the people of room 6416, for the refreshing and fruitful discussions during our coffee and lunch breaks.

Finally, I would like to thank my family and friends for their support during this process.

Jan-Henri Montonen
November 2022
Lappeenranta, Finland

“Research is what I’m doing when I don’t know what I’m doing.”

Wernher von Braun

Contents

List of publications

This dissertation is based on the following papers. The rights have been granted by the publishers to include the papers in the dissertation.

I. Montonen, J.-H., Nevaranta, N., Lindh, T., Alho, J., Immonen, P., and Pyrhönen, O. (2018). "Experimental Identification and Parameter Estimation of the Mechanical Driveline of a Hybrid Bus." *IEEE Transactions on Industrial Electronics*, 65(7), pp. 5921–5930.

II. Montonen, J.-H., Nevaranta, N., Niemelä, M., and Lindh, T. (2022). "Comparison of Extrainsensitive Input Shaping and Swing-Angle-Estimation-Based Slew Control Approaches for a Tower Crane." *Applied Sciences*, 12(12).

III. Lindh, T., Montonen, J.-H., Grachev, M., and Niemelä, M. (2015). "Generating Surface Dynamometer Cards for a Sucker-Rod Pump by Using Frequency Converter Estimates and a Process Identification Run." In *Proceedings of 5th International Conference on Power Engineering, Energy and Electrical Drives (POWERENG)*.

IV. Lindh, T., and Montonen, J.-H., Niemelä, M., Nokka, J., Laurila, L., and Pyrhönen, J. (2014). "Dynamic performance of mechanical-level hardware-in-the-loop simulation." In *2014 16th European Conference on Power Electronics and Applications*.

V. Montonen, J.-H., Lindh, T., Lana, A., Peltoniemi, P., Pinomaa, A., Tikkanen, K., and Pyrhönen, O. (2022.). "Comparison of Different Power Balance Control Methods for Battery Energy Storage Systems on Hybrid Marine Vessels." *IEEE Access*, 10, pp. 58578–58588.

Author's contribution

Author is the principal author and investigator in **Publications I**, **II**, and **V**. Author's contribution to **Publication I**: implementing the excitation algorithms to the hybrid bus control code, conducting the identification tests together with Dr. Tuomo Lindh, and building the data logging system to acquire data from the drive motor inverters. The application of the identification algorithms was carried out by Dr. Nevaranta.

In **Publication III**, Dr. Lindh was the corresponding author and conducted the study. Author participated in the writing of the publication and presented the publication in the conference.

In P**ublication IV**, Dr. Lindh was the corresponding author and conducted the study. Author participated in the experimental tests by making programs required for connecting components, conducting laboratory tests together with Dr. Lindh.

Nomenclature

In the present work, variables and constants are denoted using *slanted style*, vectors are denoted using **bold regular style**, and abbreviations are denoted using regular style.

Latin alphabet

B	viscous friction coefficient	
g	acceleration due to gravity	m/s^2
i	*AC* current	A
J	rotational inertia	kgm^2
k	torsional spring coefficient	Nm/rad
L	length	m
m	mass	kg
T	torque	Nm
u	AC voltage	V
r	radius	m

Greek alphabet

θ	rotational angle	rad
τ	torque	Nm
ω	rotational speed	rad/s

Dimensionless numbers

r	gear ratio, inertia ratio
N	number of tooth in a gear

Superscripts

´	referred value

Subscripts

a	phase a
act	actual
b	phase b
c	phase c
d	direction of d-axis
el	electrical
f	friction
J	inertia
L	load
m	motor

out	output
pri	primary
ref	reference
sec	secondary
x	direction of the x-axis
y	direction of the y-axis
q	direction of the q-axis
α	direction of the α-axis
β	direction of the β-axis

Abbreviations

AC	alternating current
BESS	battery energy storage
DC	direct current
DG	diesel generator
DP	dynamic positioning
DTC	direct torque control
DUT	device under test
FEM	finite element method
FRT	fault ride-through
HIL	hardware-in-the-loop
IOT	Internet of Things
IPC	industrial PC
LED	load-emulating drive
MBD	multibody dynamics
MHIL	mechanical-level-HIL
OSV	offshore supply vessel
PC	personal computer
PLC	programmable logic controller
PRBS	pseudo random binary sequence
SIL	software-in-the-loop

1 Introduction

A mechatronics system combines mechanical, electronical, computer, control, and telecommunication technologies (IGI Global, 2022). Mechatronic systems are used in various fields of industry, such as manufacturing, materials processing, automotive applications, aerospace, and defence systems. In Figure 1.1, an example of a mechatronic system is illustrated. A mechatronic system comprises a mechanical part, for example, a robotic arm or the driveline of a vehicle. An actuator moves the mechanics by converting electrical energy into kinetic energy. The actuator is mechanically connected to the mechanical system. Sensors provide information for the control system about the state of the system. Sensors can be used to measure, for instance, speed, torque, and position from the mechanical system. Sensors are used when accurate information from the state of the system is required. Sensors are connected mechanically to the system that they measure, and they communicate with other devices using fieldbuses, digital signals, or analog signals. Sensors, however, increase the cost of the system, and when failing, may stop the system or even cause an accident. In some applications, sensors can be replaced by estimating the values that would normally be measured by using sensors. Of course, some sensors are still required to provide information on which the estimation is based. The upper level control can be, for example, a programmable logic controller (PLC), an industrial PC (IPC), or an embedded system. Its task is to run the control algorithms and command the actuators accordingly. Depending on the application, the upper level controller communicates with the actuator using a fieldbus, digital signals, or analog signals. A fieldbus is typically used between a PLC or an IPC and an electric drive. In the robotic arm example, the upper level control calculates the position commands for each motor of the arm. An additional monitoring or user interface can be incorporated into the system to allow the operator to monitor the state of the system and the set reference values. In recent years, Internet of Things (IOT) has become more popular. IOT enables distant monitoring and control of the system over an Internet connection.

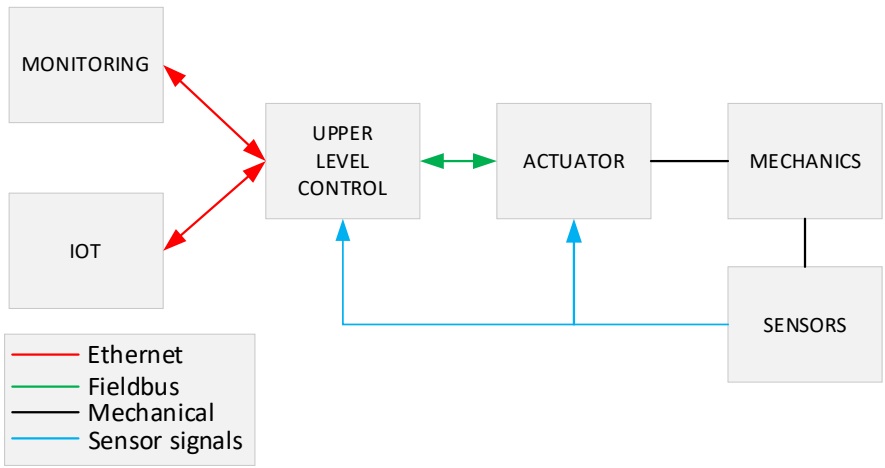

Figure 1.1 Block diagram of a mechanical system and connections between components.

Advances in computer technology in the last few decades have led to an increase in the use of electrical control systems in mechanical applications. Systems ranging from washing machines to antilock brakes of a car to various industrial robotic applications are now controlled by computer-based control systems (Capitol Technology University, 2018). AC drive technology has become more and more common in various applications, and it has opened new opportunities for the control of these applications. The use of inverter estimates for speed and torque reduce the need for instrumentation if estimates can be considered accurate enough for the application. The accuracy of inverter estimates for the speed and torque of a pump application has been investigated in (Ahonen et al., 2013). Some modern inverters have built-in PLCs, which allow users to execute programs directly in an inverter. This makes it possible to implement and run upper level control algorithms (see Figure 1.1) in an inverter and to use estimates provided by the inverter instead of measurements. All this makes it easier to implement upper level control for different applications.

The increased calculation power of consumer PCs allows real-time simulation of mechatronic systems. Multibody-dynamics-based virtual simulation technology allows to model the system (e.g., a vehicle or a mobile or nonmobile working machine) and run the model in a real environment, which helps to a create a real work cycle. This allows to test different constructions, dimensions, or control options quickly and safely without the need to build actual protypes, as building prototypes can be expensive and time consuming. Furthermore, environmental parameters, such as weather conditions or driving terrain, can be changed easily. Instrumentation is also easier as the wanted signals can be picked from the simulator. A downside of this is that constructing a detailed enough model can be challenging and requires special expertise (Aromaa, 2014). Increased processing power also allows autonomous vehicles, which can use sensors to get information of the surrounding environment and process the data in real time to be able to make decisions on their own (Sierra-García, 2020). As control systems become more complex and are more often connected to the Internet, also cyber security issues must be considered (Kotuszewski et al., 2021).

A mechatronic system often has a very specific task to run, and the task can have some performance requirements related to, for instance, energy efficiency, speed, accuracy, safety, and reliability. These requirements set specifications for the mechanical, electrical, and control design of such systems. Thus, designing systems of this kind requires a vast knowledge of different fields related to the system. Typically, the design of subsystems (mechanics, electronics, control) is divided among teams or individual engineers. The team is led by a system engineer, whose responsibility is to make sure that the subsystems can work together as intended (NASA, 2009).

Without a model of the system, it can be challenging to dimension the components, such as actuators, to ensure the required dynamic performance. Further, to be able to tune a controller for the system and to achieve a good control performance, an accurate enough model of the system is often required. If the system is not known, one can identify a model for the system by using system identification methods. If the system is known, it can be

modeled based on physical knowledge of the system. Here, modern modeling and simulation tools come in handy, as one can use them to build the model from fundamental blocks or use premade library blocks. In addition to physical models, there are a number of other types of model, such as numerical, identified, and multibody models. Selecting a suitable a model requires knowledge and experience. Furthermore, the complexity of the model must be chosen according to the research problem. The model should be accurate enough to represent the phenomena that are being studied or controlled. Using an overcomplicated model leads to an increase in the time spent for modeling, slower simulation times, and an increased number of parameters, and sometimes, it can be difficult to determine all the required parameter values.

Typical challenges of modeling a mechatronics system are delays between devices, different time constants, synchronization between components, and interaction between subsystems. These challenges must be considered when modeling the system. In addition, they also affect the simulation of such a system, especially if the simulation combines several software and hardware components, as SIL and HIL simulations typically do.

In this doctoral dissertation, selection of a suitable complexity for an electric drive and mechanics model is addressed. Different types of models are presented and compared, and it is described how they are used by the author and in the literature. The complexity of the models studied here is kept at a level suitable for modeling and simulation of mechatronic systems. The purpose of these inverter and electric motor models is not the development of such components or their control. Rather, the objective is to ensure accurate enough behavior of these components as part of a mechatronic system model. The models presented here are mainly time continuous, and they must be discretized before implementing to a discrete system. Some guidelines are given for the inverter and electric motor models on the suitable cycle time (discretization time).

1.1 Research methods and objective of the study

This doctoral dissertation aims to answer questions related to modeling of mechatronic systems, such as:

- How are the characteristics of different applications considered in the modeling of a mechatronic system; in particular, how should an electric drive be modeled in different situations?
- What application-specific characteristics should be considered when a system model is being built?
- How is the system model built so that
    - it describes the phenomena required for designing and analyzing a mechatronic system;
    - the complexity of the model is adequate, but not overcomplicated;

- it is based on analyzing the application and recognizing important modeling questions?

Different cases are studied in the related publications **Publication I**–**Publication V**. Each case presents a control or modeling challenge that is solved by applying the methods presented here.

Publication I introduces a modeling challenge. A dynamic model for a driveline of a hybrid bus is identified by using offline identification methods. The identification is carried out by superimposing an identification signal to the torque command of the inverters. Stationary and on-road tests are conducted. The identification is performed offline, and the resulting driveline models are compared with a physical reference model.

In **Publication II,** a control challenge is demonstrated. The objective is to suppress payload oscillation in a tower crane application. A traditional input shaper is compared with an estimator-based swing angle feedback method. Both methods are first tested and tuned by using multibody dynamics simulation and then tested with an experimental laboratory setup emulating one axis of a crane.

Publication III addresses the problem of generating a force–rod position plot of a sucker rod pump (type of an oil pump) without force and position measuring equipment. The problem is approached with a detailed model of the mechanics and the electric drive, because no actual sucker rod pump was available for the study. A method is constructed by first identifying the mechanics of the pump and then using the identified information about the mechanics and speed and torque estimates from the inverter model to build the rod force–rod position plot.

Publication IV presents a modeling challenge where a mechanical-level HIL is modeled and its dynamical performance is analyzed. An HIL simulator is constructed by using two back-to-back inverter–motor setups, in which one is acting as the application drive, in this case, the slew motor of a tower crane. The other is the load drive for the application drive. A transfer function model is then used to study the stability and performance of the system.

Publication V introduces a modeling and control challenge where the whole power distribution system of a hybrid marine vessel is modeled. The complexity of the model is an important aspect in this work. The model is made detailed enough to be able to study, for example, the frequency of the AC grid. However, some components, such as the diesel engine, are modeled using time constants, because the diesel engine itself is not under investigation. Suitable dynamic behavior can be achieved with a few transfer functions. This reduces the computational load of the already computationally heavy model. An off-shore supply vessel is used as the case vessel, and real load power data from an actual vessel are used as the load for the simulator. The load power data used in the study are from a time period when the case vessel is in the dynamic positioning mode. The vessel uses its thrusters to stay in place, which causes transients to the load power. Different

power balancing methods for a battery energy storage are tested, and their effect on the AC frequency and loading of the diesel gensets is compared.

1.2 Summary of scientific contributions

In **Publication I**, a resonating model for the mechanical driveline of a hybrid city bus is identified by using frequency domain parameter estimation methods. The results of the paper show that these well-known excitation-based system identification methods can be used to identify the characteristics of the mechanical driveline of a city bus. The estimated model can be adopted to model-based diagnostics or control of the driveline.

In **Publication II**, a novel closed-loop control based on swing angle estimation is proposed for reducing payload oscillation in a tower crane application as an alternative to input shaping. An advantage of the estimator-based swing angle feedback method is that it does not cause a significant delay to the operator commands like the input-shaping-based method would do. The proposed closed-loop method is equally easy to implement, and it requires the same information of the crane state as the input shaping with additional trolley movement information.

In **Publication III**, a novel method for generating a surface dynamometer card is proposed. The method allows to form a surface dynamometer card by using information of the pump geometry and inverter speed and torque estimates without additional sensors; only one limit switch is required to indicate one position of the pumping cycle. The traditional method is to attach position and force sensors to the rod of the pump.

In **Publication IV**, equations for analyzing the dynamics behavior, stability, and performance issues of a mechanical-level hardware-in-the-loop (MHIL) simulator are given. It is also shown that the dynamics of the application mechanics with the drive under test and that of the MHIL will inevitably differ from each other. In order to achieve similar dynamics for both cases at the control bandwidth, the performance and stability issues have to be analyzed case by case.

In **Publication V**, different control methods for the battery energy storage in an offshore supply vessel are proposed. The suggested control methods are based on isochronous control, which is typically employed for the power control of diesel gensets. This would enable easy retrofitting of a battery energy storage to an already isochronous control-based vessel.

1.3 Outline of the doctoral dissertation

Chapter 1 gives an introduction and describes the outline and scientific contribution of the doctoral dissertation.

Chapter 2 presents different types of inverter, electric motor, and load model. Different levels of complexity for the models are presented, and examples are given to demonstrate how these models are used by the author of this dissertation or how they are employed in the literature. Furthermore, the chapter discusses the effects of the model selection on the complexity of the other models in the system.

Chapter 3 provides summaries of the related publications and key findings of each publication.

2 Modeling and simulation of inverter-driven mechatronic systems

This chapter discusses different types of electric drive and load model as well as selection of a suitable simulation model type for an electric drive. In addition, the properties and limitations of different types of model are discussed. In this dissertation, the term ‘electric drive’ refers to a system of an inverter and an electrical motor. ‘Mechatronics’ refers to an electric drive connected with mechanics and the related sensors. In this dissertation, ‘load’ refers to the mechatronic system connected to the electric drive.

2.1 Electric drive modeling

Different levels of complexity for inverter and electric motor models are required for different simulations. In some cases, the effect of an electric drive model is only small for the overall system response, and therefore, a very simple gain model can be used, or the model can be left out. On the other hand, when the dynamics of the electric drive influences the behavior of the mechanics of the system, or when the electric drive itself is under investigation, a more complex simulation model is required. Moreover, there are other limitations, such as the nonlinearity of the inverter caused by the current or voltage limits of the inverter. If these limits are not considered, it must be ensured that the limits do not affect the simulation results. One method to simulate these limitations is to use bandwidth limitation and saturation of the output when using a simple model that normally does not take these into account, such as a gain model or a transfer function model. Hence, selecting a suitable simulation model requires knowledge from the user.

Different levels of complexity for an electric drive and load models (see Figure 2.1) are discussed separately in the following sections, and general guidelines are given as to when to use which model. It is worth noting that, in general, the modeling method of one component has an effect on how the other components can be modeled. Figure 2.1 depicts a typical position control model for mechatronics. Instead of being position controlled, the mechanics model could also be speed or torque controlled, depending on the application. An example of a position-controlled application could be a two-axis manipulator. A tower crane or a pump drive could represent a speed-controlled application, and a vehicle a torque-controlled application. In this figure, speed control and torque control are included in the inverter model as in Figure 2.3, but they could also be separate blocks after the position control.

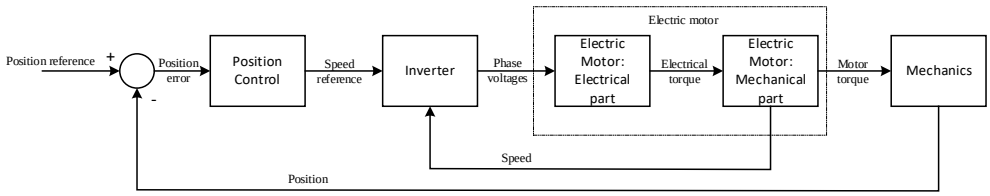

Figure 2.1 Functional block diagram of the position control of a mechatronic system. The electric motor model could be less complex and only be a transfer function, or the electric motor model could be included in the inverter model, and it would model the whole electric drive. Speed feedback is typically obtained from a sensor attached to the electric motor. Depending on the application, position feedback could come from the same sensor or from a dedicated position sensor attached to the mechanics.

2.2 **Inverter model**

In this section, different levels of inverter models are presented with some general guidelines on how to select a suitable model and what the requirements are for the simulation cycle time and for the motor model. Inverter models can be divided roughly into five categories based on their complexity as follows:

- Gain model;
- Transfer function model, possibly with saturation to model torque limits;
- Model with frequency converter control algorithms (no power electronics);
- Averaging model, power electronics modeled with ideal voltage or current sources;
- Switching model, which also includes power module switching phenomena.

The simplest form of an inverter model is a gain from the input to the output, see Figure 2.2 (a). This model can be used to describe, for example, a system of an accelerator pedal, an inverter, and an electric motor in a vehicular application when the focus is on the behavior of the vehicle with electric drives of different sizes. In that case, the input to this model is the torque reference from the accelerator pedal, the output is the torque to the vehicle model, and the whole electric drive is modeled by a gain. This gain can be a unity gain, or it can be used for converting the torque reference, for example, from per unit values to Nm. A saturation block, as in Figure 2.2 (b), can be added to limit the available torque and to model the nonlinearities caused by the inverter control, such as the current or voltage limit. Another way to do this is to limit the reference. This model has an infinite bandwidth, and if bandwidth limitation is required, then this model becomes a transfer function model, and thus, maybe using the transfer function model should be considered. Of course, for example in Simulink, a ramp function can be used for bandwidth limitation and to simulate the reference ramping of an inverter control. This type of model has no requirements for the execution cycle time. Hence, it should be selected based on the application.

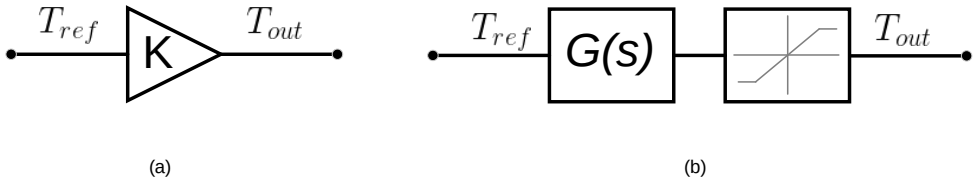

Figure 2.2 Gain (a) and transfer function model with output saturation (b).

A transfer function can be used to model the filtering effect caused by the control of the inverter and to limit the bandwidth of the electric drive model to correspond to the actual drive behavior but also to prevent high frequency oscillations when the model is connected to the mechanics model in the feedback control, see Figure 2.2 (b). Saturation can be added to simulate the limited torque caused by the limited voltage and current that are available. It is also worth noting that an anti-windup should be used in the case of Figure 2.2 (b). When the output is saturated and the transfer function model contains an integrator, the integrator can count to high values. When the input value decreases, the change is not visible in the output before the integrator counts below the saturation limit. A similar functionality is also implemented in real inverters.

The simulation cycle time should be short enough compared with the smallest time constant of the transfer function. As a rule of thumb, the cycle time should be smaller than 10–25% of the rise time of the transfer function (Åström & Wittenmark, 1995). A longer simulation cycle time causes distortion to the response of the (discrete) transfer function.

As an example of the use of the gain model, a position control model is employed for feeding the torque reference directly to the mechanics model, as in (Saarakkala et al., 2009) and (Jokinen et al., 2008). Therefore, the rest of the electric drive model after the position control is reduced to a simple gain model. The authors of these papers considered that the dynamics of the electric drive can be ignored in the dynamical model of the overall system. A position control was modeled because the aim of the paper was to show how to compensate the nonlinear friction and spring constant of the linear tooth belt drive using a feedforward control. In (Mohamed, 2006), a gain model is used for the electric drive and the load is modeled using an inertia and friction model.

A gain model for the electric drive with a torque limit is used in (Harnefors et al., 2013) to limit the maximum torque available from the drive. In this case, a simple gain model for the inverter is sufficient because the mechatronic system is slow compared with the inverter dynamics, and the inverter is not the component under investigation.

As an example of a transfer function drive model, in (Younkin, 1989), the performance of a servo drive for a machining tool is analyzed. The servo drive control, the current

regulator, and the machining tool are modeled using transfer functions. This paper also models the nonlinearities of the machining tool, such as stiction and backlash. In this case, the effect of the servo drive on the system dynamics could not be neglected, and an accurate model was required to be able to analyze the performance of such a system.

Figure 2.3 presents a block diagram of an inverter control containing speed control, torque and flux control, current limiting, current control, voltage limiting, and transformations between stator and rotor coordinates and three-phase into αβ stator coordinates, according to space current vector theory and the 2-axis modeling principles (Kovács, 1984). The model does not contain a model for the power electronics. The model outputs u_α and u_β voltage references. This type of a model can be used to simulate the effect of the inverter control on the overall system or the behavior of the inverter control in different situations. This type of model requires a shorter simulation cycle time than the transfer function model to be able to exploit the increased complexity of the model. The cycle time can be the same as the task cycle time of a real inverter. This type of inverter model also requires an accurate motor model, at least a 2-axis model (Leonhard, 2001).

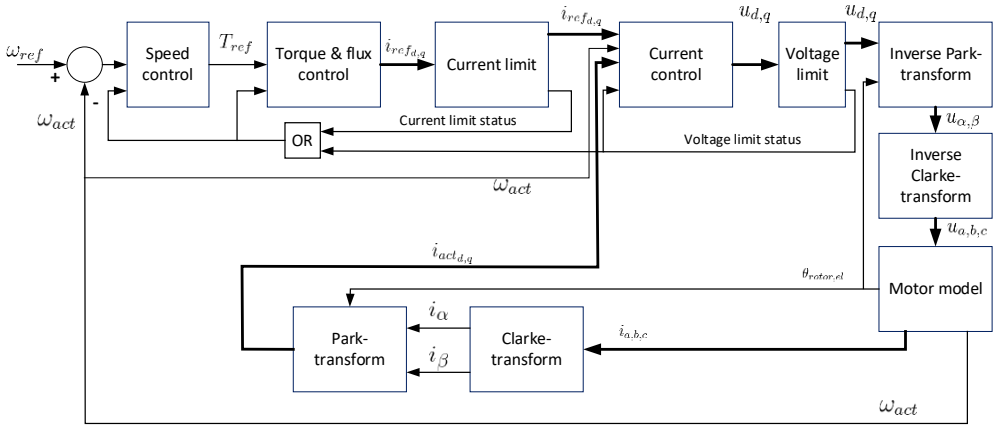

Figure 2.3 Model of an inverter control with speed control. The bolded lines contain several signals. The rotational speed feedback ω_{act} can also be calculated in the mechanics (or load) model.

As an example of a detailed inverter model, in (Luukko et al., 2009), the fault ride-through (FRT) capabilities of a wind turbine are investigated by using a Simulink-based simulation tool. In addition to FRT, in (Tiainen, 2010), a wind turbine electric power train model is used for the analysis of the applicability of time domain simulations in the technical and economic analysis of a wind energy conversion system. While the economic analysis part is not new, simulations had not been used before to obtain the required efficiency information. The simulation-based approach is expected to enable the analysis of the whole drivetrain (including the effect of control algorithms), which is very difficult by using analytical calculation. Therefore, a detailed model of the wind turbine electric

drivetrain is required to be able to perform the analysis. To this end, the inverter switching losses were analyzed separately and calculated parallel to the dynamic simulations to avoid the use of a switching power electronics model. This could be done because the author was not interested in the effects of switching, other than losses. The information produced by the simulation could then be used to evaluate the costs of a wind turbine drivetrain.

A detailed inverter model with control code is used in **Publication III** to be able to simulate plotting of surface dynamometer cards for a sucker rod pump by using inverter estimates. A surface dynamometer card is a plot of rod force as a function of rod displacement, and it is used for the evaluation of the pump performance and oil well conditions. For this purpose, a detailed inverter model and a mechanical model of the sucker rod pump is required because there is a risk of nonlinear behavior of an inverter, which could deteriorate the formation of the surface card in an actual device. In (Montonen et al., 2012), software-in-the-loop (SIL) simulation is used as a tool for dimensioning the hybrid power train of a working machine. An inverter control code with an electric motor model is used as part of the SIL to accurately model the behavior of an inverter-driven electric drivetrain of a working machine. In (Aarniovuori, 2010), the dependence of the inverter switching frequency on the inverter and induction motor losses is investigated by using simulations and actual measurements. A finite element method (FEM) model is used for the induction motor. To be able to simulate the inverter losses and to run the FEM motor model, a detailed inverter model is required. In (Lindh, 2013), various problems arising from nonlinearities and time-varying components of the inverter and mechanics model are discussed and ways to simulate such systems are addressed. Special interest is devoted to the SIL and HIL simulation.

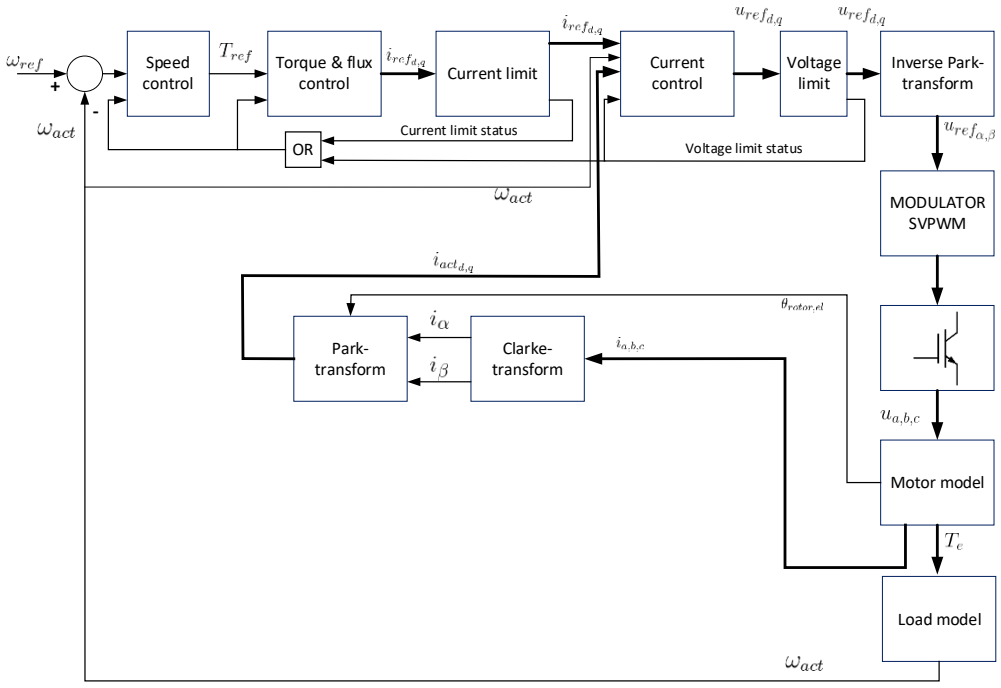

Figure 2.4 Electric drive model containing a power electronics model, a motor model, and a load model. The speed feedback can also be obtained from the motor model.

The power electronics model in Figure 2.4 can be an averaging or a switching type model. An averaging model is used when there is no need to analyze switching phenomena. The output of the averaging model is sinusoidal voltage waveforms. Unlike transistor and diode models, the averaging model contains controllable voltage sources. The use of an averaging model instead of a switching model reduces the computational load. This makes the averaging model a preferred selection for system-level simulation when a detailed inverter model is required.

The switching model contains transistor models, or a model of a transistor bridge, which are switched using gate signals from the modulator. Depending on the aim of the modeling and simulation, a switching model can also include the transient phenomena of switching and not only treat switches as conducting or nonconducting. The output of a switching model is the pulse-width-modulated phase voltage. The switching model requires a short simulation cycle time, which makes system-level simulations impractical. The switching inverter model also requires a motor model that is capable of reacting to the switching events.

An inverter model with a control and power electronics model is employed in (Bubert et al., 2014) to study the drivetrain efficiency and energy consumption by using a simulation

tool. A 2-axis model is used for an electric motor, but losses are modeled using a separate loss model.

A Simulink model of an inverter, similar to the one presented in Figure 2.3, without a motor model, was compiled and used to run a real permanent magnet synchronous motor. The output of the model was the u_α and u_β voltage references for the modulator. The modulator was then connected to an oversampling digital output card, which was used to give switch signals to an IGBT power module. This experimental setup was used for educational purposes when teaching motor control. This also proves the accuracy of this model; if it can be compiled and used as a controller for inverter power electronics, it also models an inverter accurately.

2.3 Electric motor model

Different types of electric motor model can be identified, and their complexity varies depending on the purpose of the simulation. Generally, for mechatronic system-level simulation, a simple gain or transfer function model suffices for the whole electric drive. When the simulation concentrates on some special case, such as losses or behavior in a certain situation, a more detailed model is required. The model types discussed here are:

- Gain model;
- Transfer function model;
- Two-axis model;
- Finite element method (FEM) models.

A gain model and a transfer function model, similar to the inverter model depicted in Figure 2.2, can be used for an electric motor. The gain model does not set any requirements for the simulation cycle time. A gain model is suitable when the dynamics of the motor has only a small effect on the system dynamics and/or the electric motor is not the main interest of the simulation. For a transfer function model, the same rules apply as in the case of an inverter model. Often, the response of an electric motor is fast compared with an inverter, and therefore, an electric motor model can be included in the inverter model, or both are modeled using the same transfer function. A separate transfer function model can be used, for example, to describe the mechanics of the electric motor.

Field weakening is a technique for increasing the rotational speed of the electric motor above its rated speed at the expense of torque. In field weakening, torque is reduced as the speed increases. This behavior could be modeled by adding a saturation block after a gain or transfer function model, and the saturation value should depend on the rotational speed (Leonhard, 2001).

Gain or transfer function models can be used for the inverter when these models are used for the electric motor. The inverter and electric motor models can be combined and represented by using one gain or transfer function model as it is done in (Jokinen et al., 2008) and (Saarakkala et al., 2009).

The d-q -axis model (or two-axis model) is a commonly used model of an electric motor. It presents the motor using two axes, the direct axis (d-axis) and the quadrature axis (q-axis). The d- and q- axes are fixed to the rotor flux and axes. Motor currents can be divided into components along the d-axis (i_d) and components along the q-axis (i_q). Motor torque can be calculated by using current components and known motor parameters, such as the motor inductances.

A mechanical model can then be used to calculate the mechanical rotational speed of the motor:

$$\frac{d\omega_\mathrm{m}}{dt} = \frac{1}{J}(T_\mathrm{e} - T_\mathrm{f} - B\omega_\mathrm{m} - T_\mathrm{L}) \tag{2.1}$$

where ω_m is the angular mechanical speed of the rotor, J is the rotational inertia of the rotating parts, T_e is the electromagnetic torque, T_f is the rotor shaft static friction torque, B is the combined static viscous friction coefficient of the rotor and the load, and T_L is the load torque.

Modern simulation tools (such as MATLAB/Simulink) have built-in blocks for electric motors that employ the two-axis model. Often, there is no need for the user to model the electric motor by using fundamental blocks. Of course, this does not eliminate the need to know the limitations and properties of each premade block.

A 2-axis model for an electric motor can be used when there is no need to investigate switching-time-level phenomena, but a more detailed model than a transfer function model is required. The 2-axis model contains an electric model of the motor for calculation of the fluxes and currents and the resulting electrical torque. Then, a mechanical model can be used to calculate the rotational speed of the motor. A 2-axis model of the motor can be used when, for example, a model of a motor inverter containing control algorithms is being tested. Suitable inverter models for running the 2-axis model from the inverter models presented in this work are the models with a control model with or without a power electronics model. The u_α and u_β voltages from the inverse Park transformation block can be fed to the d-q model as inputs.

For the investigation of different motor design properties, the finite element method (FEM) can be employed. The FEM is used to compute numerical approximations of complex partial differential equations, which often cannot be solved analytically. These approximations can then be solved by using numerical methods. The FEM is widely used when solving, for example, magnetic, thermal, or structural stress calculations. While simulating an electrical motor, the FEM can be used for solving magnetic equations, and

an electric circuit simulator can be used for solving electrical equations. Other simulators can be added, for example, for calculating losses. The inputs to the FEM model are phase voltages or currents. Electrical equations are then used for calculating the currents, which are then used for the calculation of magnetic fields. Torque is calculated, and based on the equation of motion, the rotor movement and the new position are calculated (Comsol, 2016).

To fully benefit from a FEM model, a switching model is required to feed the input voltages into the FEM model. An averaging model is not sufficient if the effect of switching is analyzed; on the other hand, this is not normally included in the analysis of mechatronic systems.

In (Bubert et al., 2014), different simulation tools are combined to establish a method for designing and analyzing electric drivetrains, which consist of an inverter, an electric motor, and a gearbox. The FEM is used to calculate the simulation model parameters for a frequency inverter model consisting of a control model, and a power electronics model driving a d-q frame model of an electric motor. Additional models are used for calculating the inverter and electric motor losses, and efficiency maps are formed based on the simulation data.

A FEM model of a frequency-converter-fed induction motor is used for the analysis of losses in (Aarniovuori, 2010). Direct torque control (DTC) and vector control algorithms are implemented into a simulation software to be able to run the FEM model. The dependence of the inverter, induction motor, and system losses on the switching frequency is investigated by using this setup.

As a summary of Sections 2.2 and 2.3, inverter model types, their typical use cases, and suitable electric motor model types is given below.

- Gain model
    - Usage
        - When the inverter dynamics has only a small effect on the dynamic behavior of the whole system. A mechanical system model connected to the inverter model is much slower than the inverter model, and the nonlinear behavior of the inverter does not affect the behavior.
        - The subject under investigation is the dynamic behavior of the mechanical system under, for example, speed or position control, not the inverter or the electric drive itself.
        - Saturation can be added to describe the limited control performance of the inverter.
    - Required motor model

        - The whole electric drive is modeled as a gain, in other words, the torque output follows the torque reference exactly;
        - or a mechanical model for the motor can be used, see (2.1).
- Transfer function model
    - Usage
        - When the dynamic response of the mechanical system is fast enough in order for the inverter model to have an effect on the overall system response, then a first or second order transfer function can be used to model the filtering done by the inverter control.
        - Saturation can be added to model the limited control effort of the inverter.
    - Required motor model
        - Gain model;
        - Transfer function model;
        - or none.
    - Usage in related publications
        - **Publication I**;
        - **Publication IV**.
- Model with control algorithms
    - Usage
        - Contains speed, torque, flux, and current controllers, and coordinate transformations.
        - Can be used to investigate inverter control with a suitable motor model.
    - Required motor model
        - 2-axis model.
- Averaging model
    - Usage
        - Contains speed, torque, flux, and current controllers and coordinate transformations. Power electronics replaced with current sources.
        - Suitable for investigating the behavior of the inverter control or motor/network.
        - Uses average values of current/voltage.
        - Not suitable for investigating switching phenomena.
    - Required motor model
        - 2-axis model.
    - Usage in related publications

        - **Publication III**;
        - **Publication V**, grid inverter.
- Switching model
    - Usage
        - The same as the averaging model, but the model also includes ideal power switch models.
        - Suitable for analyzing switching phenomena.
        - Requires the most computational power.
        - Not useful when simulating mechatronics.
    - Required motor model
        - FEM model;
        - 2-axis model typically not feasible.

2.4 Load model

In the scope of this work, the load model is typically the mechanics attached to an electric drive, such as the longitudinal dynamics of a vehicle (**Publication I**), the mechanics of a rod pump (**Publication III**), or the slew motion dynamics of a tower crane (**Publication II**). A simple mechanics model based on Newton's Second Law can often be used as a load if the mechanics is not under investigation.

The feedback signal back to the control is typically obtained from the load model. The feedback signal can be, for example, the speed, position, or angle of the controlled process. Typically, selecting the load model is easy. If the purpose of the simulation is to design a control for a certain system, then the system model is acting as the load for the inverter and electric motor models. Although the selection of the load model is straightforward in many cases, finding a suitable load model plays an important role in the control system design.

When considering real-world mechanical systems, nonlinearities play a role in the behavior of the system. Often, mechanical systems are also time varying as the mechanics wear out or environmental conditions affect them (e.g., temperature fluctuation, dirt). Mechanical clearances and friction are common nonlinearities in mechanical systems. For example, mechanical clearances between the gear teeth cause nonlinear behavior to the system. Friction is, by its nature, also nonlinear. For instance, the tire–road friction is high when the tire is not slipping. However, when the tire starts to slip, the kinetic friction is smaller than the static friction, and the tire accelerates rapidly if the torque is not reduced. In (Montonen & Lindh, 2014), a sensorless traction control system is tested using a small electric vehicle. A fuzzy controller is used to control the torque of the traction motor because of the nonlinear behavior of the tire–road friction.

A system model can be linearized (in a certain operating region) to get rid of the nonlinear parts. This makes it easier to analyze and design a control for the system. Figure 2.5 presents a typical case of linearization where $\cos(\theta) \approx 1$ and $\sin(\theta) \approx \theta$; these are valid for small values of θ. Therefore, in the figure, $L_y \approx L$ and $L_x \approx L\theta$ when the swing angle θ is small. At larger angles, other means are required.

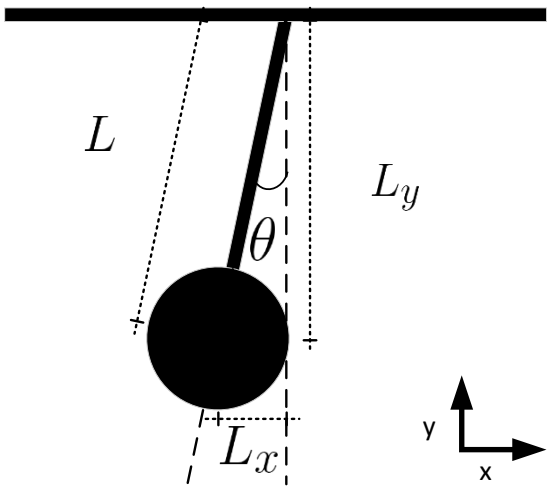

Figure 2.5 Example of linearization at small angles.

This kind of linearization is used in **Publication II** to linearize the applied crane load model, which is used to estimate the load swing angle. The control algorithms are also tested by using an experimental laboratory setup to verify their functionality on actual hardware.

It is worth mentioning that there is no universal technique for the analysis of nonlinear control systems. In linear control, the system can be analyzed in the time or frequency domain. For nonlinear control systems, none of these standard approaches can be used because a direct solution of nonlinear differential equations is generally impossible, and frequency domain transformations do not apply. While the analysis of nonlinear control systems is difficult, construction and simulation of a nonlinear simulation model are not any harder than in the case of a linear model. For example, in (Montonen & Lindh, 2014), the nonlinear friction of tire–road contact was modeled in Simulink, and fuzzy-logic-based traction control was hand tuned for the system.

For the analysis of nonlinear control systems, many methods have been proposed. One of these methods is the describing function method. The basic idea of the method is to approximate the nonlinear components in nonlinear control systems by linear "equivalents," and then use frequency domain techniques to analyze the resulting systems. Even though the describing function method is an approximation method, it allows to use

frequency domain methods, commonly used for linear systems, to nonlinear systems by forming a linear approximation of the nonlinear system. This method can be used for prediction of limit cycles in nonlinear systems, predicting subharmonics, jump phenomena, and the response of nonlinear systems to sinusoidal inputs (Slotine, 1991), (Mladenov, 2009). For example, in (Úředníček, 2018), describing functions are used to describe the hard nonlinear parts of a robot. Based on the description provided by the describing functions method for the nonlinear parts of the robot, a formalization of a limit cycle prediction process is performed.

If the system under investigation comprises an inverter and an electric motor model and the load is not of particular interest, then a commonly used model that is based on Newton's law of rotating bodies can be used as the load model for the system. The model comprises the inertia of the rotating parts and a friction part that depends on the rotational speed of the rotor. Additional load torque can be included. The load torque can be static or a function of time. The equation for the model is written as

$$T_\mathrm{e} = T_\mathrm{L} + J\frac{d\omega}{dt} + B\omega \tag{2.2}$$

where T_e is the electrical torque of the motor, T_L is the load torque, J is the rotational inertia of the rotating parts, ω is the rotational velocity of the rotor, and B is the friction coefficient. This type of model is used in (Harnefors et al., 2013) and (Lindh, 2013) to provide load for the inverter and electric motor models. The mechanical model can also have rotational speed as an input and loading torque as an output, as it was done in **Publication III** to balance the simulation.

The model presented here is stiff and does not contain any flexible parts. In a real-world case, there are flexible parts, such as axles and belts. The flexing of these parts must be taken into account in the modeling of the system when the simulation time step is short and an accurate model is required.

Figure 2.6 illustrates a flexible servo axis model. The model contains an electric motor connected to a gearbox with a stiff axle. The gearbox is then connected to a load by using a flexible axle. This type of load model can be used to model mechanics connected to an electric drive with a flexible connection; for example, a manipulator in which the belt is the flexible part, or a driveline of a vehicle in which the drive shaft is the flexible part.

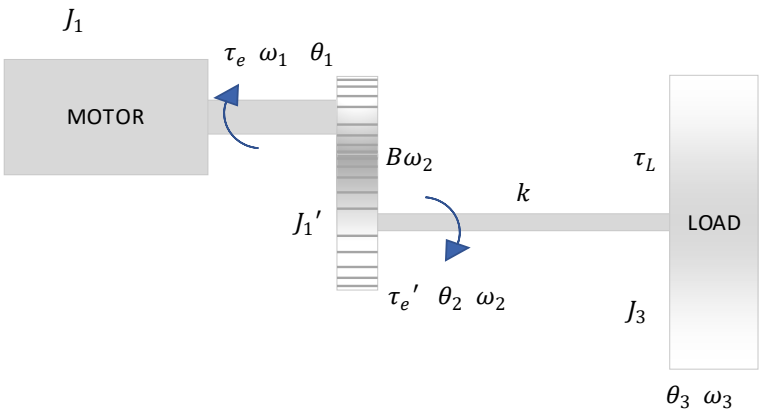

Figure 2.6: Servo axis model with a motor, a gearbox, a flexible axle, and a load inertia.

In Figure 2.6, ω is the rotational speed, θ is the rotation angle, J is the rotational inertia, r is the gear ratio of the gearbox, B is the friction coefficient of the gearbox (measured on the secondary side), k is the torsional spring coefficient of the flexible axle, and τ is the torque of each component. The subscripts 1, 2, and 3 indicate the sections of the model. The subscript 1 denotes the primary side of the gearbox, 2 indicates the secondary side of the gearbox, and 3 refers to the load side. The values of the primary side of the gearbox can be referred to the secondary side by using the gear ratio of the gearbox:

$$r = \frac{r_{\text{sec}}}{r_{\text{pri}}} = \frac{N_{\text{sec}}}{N_{\text{pri}}} = \frac{\omega_{\text{pri}}}{\omega_{\text{sec}}} \tag{2.3}$$

where r_{sec} and r_{pri} denote the radius of the secondary- and primary-side gear of the gearbox, and N and ω indicate the tooth count and the rotational speed, respectively. The electrical torque τ_{e} referred to the secondary side is then

$$\tau_{\text{e}}' = \tau_{\text{e}} r \tag{2.4}$$

and the inertia J_1 referred to the secondary side is

$$J_1' = J_1 r^2 \tag{2.5}$$

We split the model from the flexible axle and write equations of motion for the two bodies, one being the body consisting of a motor and a gearbox and the other being the load inertia.

$$\tau_e' = J_1' \frac{\mathrm{d}\omega_1'}{\mathrm{dt}} + B\omega_1' + k(\theta_2 - \theta_3)$$

$$k(\theta_2 - \theta_3) - \tau_\mathrm{L} = J_3 \frac{d\omega_3}{dt} \tag{2.6}$$

Further, by replacing $\omega_1{}'$ by ω_2 and solving $\frac{d\omega_2}{dt}$ and $\frac{d\omega_3}{dt}$, we get

$$\frac{d\omega_2}{dt} = \frac{1}{J_1{}'}\tau_e' - \frac{B}{J_1{}'}\omega_2 - \frac{k}{J_1{}'}(\theta_2 - \theta_3)$$

$$\frac{d\omega_3}{dt} = \frac{k}{J_3}(\theta_2 - \theta_3) - \frac{1}{J_3}\tau_\mathrm{L} \tag{2.7}$$

By selecting the states ω_2, ω_3 and $\theta_2 - \theta_3$ and the inputs $\tau_\mathrm{e}{}'$ and τ_L, we get the state–space model

$$\begin{bmatrix} \frac{d\omega_2}{dt} \\ \frac{d\omega_3}{dt} \\ \theta_2 - \theta_3 \end{bmatrix} = \begin{bmatrix} -\frac{B}{J_1'} & 0 & \frac{k}{J_1'} \\ 0 & 0 & \frac{k}{J_3} \\ 1 & -1 & 0 \end{bmatrix} \begin{bmatrix} \omega_2 \\ \omega_3 \\ \theta_2 - \theta_3 \end{bmatrix} + \begin{bmatrix} \frac{1}{J_1'} & 0 \\ 0 & -\frac{1}{J_3} \\ 0 & 0 \end{bmatrix} \begin{bmatrix} \tau_\mathrm{e}{}' \\ \tau_\mathrm{L} \end{bmatrix} \tag{2.8}$$

The program implementation of a state–space model allows to set conditions for signals in order to create bilinear behavior to the model. In (Caruntu et al., 2010), a driveline with backlash is divided into two modes: a contact mode and a noncontact mode. Both modes have their own equations for describing the dynamic behavior of the driveline.

The ratio between the load inertia and the rotor inertia of the motor is called inertia ratio. The inertia ratio is described by

$$r_\mathrm{J} = \frac{J_\mathrm{L}}{J_\mathrm{m}}, \tag{2.9}$$

where J_L is the inertia of the load reflected to the motor, and J_m is the inertia of the motor. The load inertia must be referred to the motor side if there is a gearbox between the load and the motor, and linear motion must be converted into rotational motion. The inertia ratio should be kept as low as possible when a high performance is required. The downside of too low an inertia ratio is the higher cost and energy consumption of the servo motor. On the other hand, too high an inertia ratio can cause a poor control performance as the motor is undersized with respect to the load. For example, an inertia ratio of 5:1 or less is recommended for high-performance servo drives (ABB, 2013).

The above-described type of resonating two-mass model is used widely to model different kinds of mechanical systems. In **Publication I**, it is used as a reference physical model for a driveline of a hybrid bus. In (Nevaranta et al., 2015), a similar two-mass model is used to model a linear tooth belt drive. In general, a two-mass model can be used to model a system containing a mass or an inertia attached to a prime mover using a flexible axle or a belt.

2.4.1 Multibody dynamics simulation

A multibody dynamics (MBD) simulator can be used as a load model, or it can be used to record work cycles, which can then be used to provide a real load to the simulation model. Multibody dynamics simulation is a numerical simulation method in which the simulated system is divided into bodies; rigid or flexible. Then, these bodies are connected with mechanical joints, forces such as springs, actuators, and frictional forces between bodies. A graphical 3D model of the system is used to visualize simulation. In the case of working machines, cranes, and the like, also the environment is modeled as it is an important part of the work cycle. It is also important that the simulated working environment matches the real working environment when, for example, dimensioning of the driveline components for a hybrid working machine is investigated (Montonen et al., 2012).

The MDB simulation allows to drive a working machine in a real environment, which makes it a useful tool for machine operator training and virtual prototyping of such working machines. Virtual prototyping allows quick changes to the machine and the environment, which makes it easy for the manufacturer to try, for example, different driveline configurations (Montonen et al., 2012). Figure 2.7 presents a commercial MBD simulator. The simulator features a virtual cabin with joysticks and pedals for a real feel and view as in the original machine.

Figure 2.7 Commercial MBD simulator with a tower crane model.

The MBD simulator can send and receive data via a TCP connection between the MBD solver program and an external program. This allows parts of the simulated system to be modeled elsewhere (e.g., in Simulink), and the models can be driven in real time against a real load. Alternatively, the control algorithms of components can be implemented to a separate program, and that program can be connected to the simulator, Figure 2.8. The MBD simulator sends drivers' references, for example, in the case of a tower crane: slew, trolley, and hoist motor speed requests, actual motor speeds, and other simulation-related data, such as hoist cable swing angles, the slew movement rotation angle, and the trolley position. The MBD simulator receives torque references for the slew, trolley, and hoist

motors. This then allows to, for example, control the movements of a tower crane using an external application as it is done in **Publication II**.

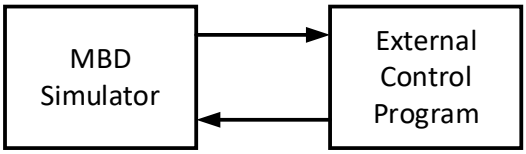

Figure 2.8 MBD simulation with external control.

This kind of distributed simulation is called co-simulation. An example of co-simulation is presented in (Montonen & Lindh, 2014), where a sensorless traction control application is developed using an MBD simulator, and further tested using an actual light electric vehicle.

One type of co-simulation is hardware-in-the-loop (HIL) simulation. In the HIL simulation, parts of the simulation models (software) are replaced by an actual hardware. In the case of Figure 2.8, the external control program can be replaced by a programmable logic controller (PLC), and it can then perform control tasks and run actual hardware via a fieldbus connection. Operator commands are read from the MBD simulator and relayed to the actual hardware. The MBD simulator also sends the commands via PLC for the load-emulating part of the HIL. When testing, it must be ensured that the load-emulating drive is capable of following the reference sent by the MBD simulator. Otherwise, the HIL simulation is no longer emulating the real case. The HIL simulation allows to test actual hardware against real loads in laboratory conditions, where, for example, instrumentation is easier than in real-world machines, which are moving in harsh conditions (Lindh et al., 2014).

2.5 System identification

Instead of modeling the system by using known physical and technical descriptions of the system, it can be identified. System identification is an experimental procedure in which an identification signal is fed to the system and the output from the system is observed. Then, a model for the system can be obtained. Identification is called “black box” identification if there is no prior knowledge available of the system.

Identification methods can be used to identify parameters of an existing system model, when, for example, commissioning a new machine or when system parameters change as a result of mechanical wear or a component change. In this case, for example, the physical model is known from the system, and identification can be used to find parameters for the model. This is called grey or white box identification.

The system identification is an iterative process that consists of experiments, choosing model sets, picking the best model, and validating the model. Often, several iterations are required. Figure 2.9 describes the flow of the process.

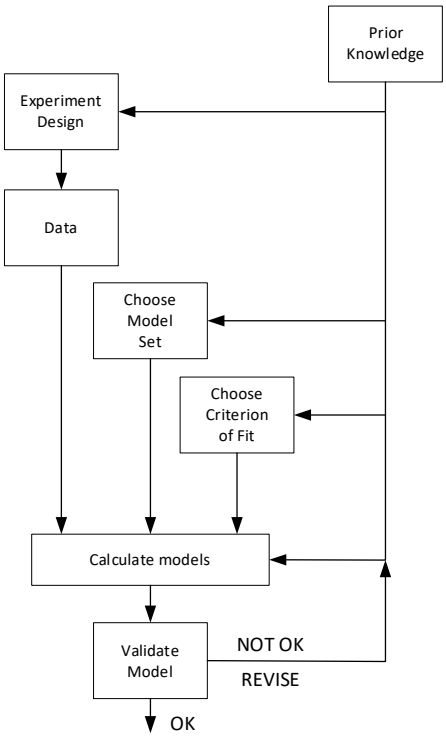

Figure 2.9 System identification process (Ljung, 1987).

System identification methods can be divided into two groups: parametric and nonparametric methods. Parametric methods identify a set of coefficients or parameters for the selected mathematical structure. Nonparametric methods form a system model based on its responses. Nonparametric methods can be further divided into time and frequency domain methods. Common time domain methods are impulse response and step response analysis. Frequency domain methods form a system model by making a relation between frequency responses of the output and input of the system (Ljung, 1987).

An excitation signal is used as an input to the system. Its purpose is to provide a known input to the system, from which the response can be measured to form the frequency response of the system. Common excitation signals are pseudo random binary sequence (PRBS) and sine signals, such as multisine and sine sweep. A PRBS signal consists of short pulses that seem to make a random sequence, but it is a repeating signal. A PRBS signal has a frequency content similar to white noise, and therefore, the power spectrum of the PRBS signal is spread over a wide frequency range. When applied, the PRBS excites the system in a wide frequency range at once, which can be gentler for the mechanics as the system will not start resonating at its resonant frequency. Multisine and sine sweep can be targeted to a specific frequency range, but these signals carry their power on a narrow frequency band at a time. Hitting the resonance frequency with a sine signal could cause mechanical stress for the system.

In **Publication I**, the authors use parametric and nonparametric methods to identify a mechanical model for a hybrid bus driveline. PRBS, sine sweep, and stepped sine are used as excitation signals. The identified driveline model can be adopted, for example, to control design when minimizing driveline resonances. In (Montonen & Lindh, 2014), identification of the vehicle mass is carried out by an event-seeking mass estimator. The mass estimator is part of a sensorless traction control system, which requires information on the current mass of the vehicle. The system is designed to work in a working machine, which tends to have a variable total mass as the load mass of the machine varies.

3 Summary of findings in different applications

This chapter summarizes the related publications and presents the key findings in each case study.

3.1 Experimental identification and parameter estimation of the mechanical driveline of a hybrid bus

In **Publication I**, the driveline of a hybrid city bus is identified by feeding in a test signal during a standstill and on-road experiments and measuring the frequency response. Stepped sine, sine sweep, and pseudo-random binary signals are used as test signals. The identification scheme is presented in Figure 3.1.

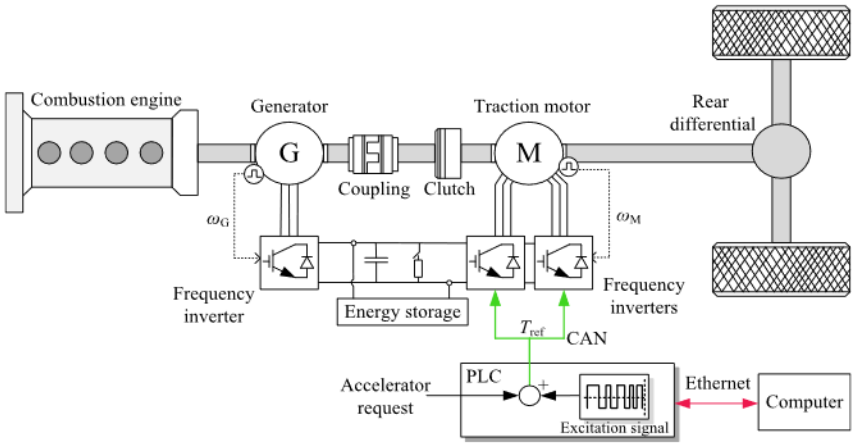

Figure 3.1 Hybrid driveline identification scheme (**Publication I**) © 2018 IEEE.

The identification signal is generated in the PLC and superposed to the torque signal going to the mobile inverters. A laptop PC is used for data capturing. The driveline is operated in the series hybrid mode, which means that the clutch between the traction motor and the generator is uncoupled. This corresponds to the fully electric operation mode. The PLC and CANopen run on a 10 ms cycle time, which means that the torque reference is updated at a 100 Hz frequency; also the rotational speed is read from the inverter at the same frequency. This means a 0 to 50 Hz frequency region for the identification. Rotational speed is measured using a resolver encoder attached to the electric motor.

Figure 3.2 illustrates a PLC function block for generating the PRBS signal. It consists of delays, AND operations, and XOR operations. The number of delays defines the length

of the PRBS. The function block depicted in the figure has ten delays, and thus, it is called PRBS10, and its repetition cycle length is $2^{10} - 1 = 1023$ values.

```
FUNCTION_BLOCK PRBS10_FB
VAR_INPUT
                  EN : BOOL;
                  OutputAmplitude : REAL;
                  OutputOffset : REAL;
                  OutputTemp : REAL;
END_VAR
VAR_OUTPUT
                  output: INT;
END_VAR
VAR
                  out0: BOOL := TRUE;
                  out1: BOOL := TRUE;
                  out2: BOOL := TRUE;
                  out3: BOOL := TRUE;
                  out4: BOOL := TRUE;
                  out5: BOOL := TRUE;
                  out6: BOOL := TRUE;
                  out7: BOOL := TRUE;
                  out8: BOOL := TRUE;
                  out9: BOOL := TRUE;
                  out10: BOOL := TRUE;


                  M10: BOOL;
                  M9: BOOL;
                  M8: BOOL;
                  M7: BOOL;
                  M6: BOOL;
                  M5: BOOL;
                  M4: BOOL;
                  M3: BOOL;
                  M2: BOOL;
                  M1: BOOL;
END_VAR
-------------------------------------------------------------------------------
IF EN=TRUE THEN (* If the block is enabled *)

                  (* Calculate the intermediate results *)
                  M10 := out0 AND TRUE;
                  M9 := (out1 AND FALSE) XOR M10;
                  M8 := (out2 AND FALSE) XOR M9;
                  M7 := (out3 AND TRUE) XOR M8;
                  M6 := (out4 AND FALSE) XOR M7;
                  M5 := (out5 AND FALSE) XOR M6;
                  M4 := (out6 AND FALSE) XOR M5;
                  M3 := (out7 AND FALSE) XOR M4;
                  M2 := (out8 AND FALSE) XOR M3;
                  M1 := (out9 AND FALSE) XOR M2;

                  (* Update the output, output is -1 or 1 *)
                  IF out0=TRUE THEN
                                    OutputTemp := 1*OutputAmplitude + OutputOffset;
                  ELSE
                                    OutputTemp := -1*OutputAmplitude + OutputOffset;
                  END_IF


                  (* Update old values for next execution *)
                  out0 := out1;
                  out1 := out2;
                  out2 := out3;
                  out3 := out4;
                  out4 := out5;
                  out5 := out6;
                  out6 := out7;
                  out7 := out8;
                  out8 := out9;
                  out9 := out10;
                  out10 := M1;

ELSE (* if the block is not enabled *)

                  OutputTemp := 0;

END_IF;

(* Block output must be INT *)
output := REAL_TO_INT(OutputTemp);
```

Figure 3.2 IEC61131-3 Function block implementation of the PRBS-generating code.

Sine chirp is a sine signal in which the frequency is swept over a range of values at a certain speed.

Figure 3.3 presents the IEC61131-3 function block used for creating a sine sweep between two frequencies using the given sweep speed.

```
FUNCTION_BLOCK SINGEN_FB
VAR_INPUT
                  EN : BOOL;
                  amplitude : REAL;
                  frequency :REAL;
                  endfrequency : REAL;
                  sweepspeed : REAL;
                  waveoffset : REAL;
                  samplingfreq : REAL;
END_VAR
VAR_OUTPUT
                  output : INT;
                  currentfreq : REAL;
END_VAR
VAR
                  n : REAL;
                  Ts : REAL;
                  k : REAL;
                  int_EN : BOOL;
END_VAR
```

```
Ts := 1/samplingfreq;

IF EN = TRUE AND int_EN = TRUE THEN

                  k := sweepspeed;

                  output := REAL_TO_INT(amplitude * SIN(6.283185*(frequency*n*Ts + (k/2)*(Ts*n)*(Ts*n)))
+ waveoffset);
                  n := n+1;

                  currentfreq := frequency + k*Ts*n;

                  IF currentfreq >= endfrequency AND k<>0 THEN
                                    k:= 0;
                                    int_EN := FALSE;
                  END_IF;

ELSIF EN = TRUE AND int_EN = FALSE THEN
                  output := 0;
                  n := 0;
                  currentfreq := 0;

ELSE
                  output := 0;
                  n := 0;
                  currentfreq := 0;
                  int_EN := TRUE;
END_IF;
```

Figure 3.3 IEC61131-3 Function block for generating a sine sweep.

A sine sweep has power at one frequency at a time, and thus, it can excite mechanical resonances quite violently in the driveline or in the vehicle body when the sweep frequency finds a resonance. This causes stress to the driveline and discomfort to the driver and passengers, if, for example, driveline identification is used for condition monitoring during normal operation.

The power spectrum of the PRBS is spread over the frequency bandwidth, causing less violent resonance and less stress to the mechanics compared with the sine sweep, and also

less discomfort to the driver and passengers if condition monitoring is performed during normal operation.

Although the identification is performed offline, at least parameter estimation could be performed online using a dedicated PLC or Industrial PC for the task, because the calculation related to the identification would cause unnecessary computational load to the controller (in this case a PLC), which is already controlling the functions of the hybrid bus.

The results show that well-known excitation-based system identification methods can be adopted to identify a resonating mechanical load of an actual hybrid bus.

Although a hybrid bus was used in this study, the proposed approaches can be used with other mobile technologies, such as working machines and electric vehicles. Adopting these methods can improve the accuracy of the driveline model, which can be used for condition monitoring, diagnostics, and control. These methods can also be employed with the identification run of different automotive applications.

3.2 Comparison of extra-insensitive input shaping and swing-angle-estimation-based slew control approaches for a tower crane

In **Publication II**, an input shaper and a swing-angle-feedback-based control for tower crane slew and trolley movements (see Figure 3.4) is compared. First, both methods were implemented to a separate control program running along (as illustrated in Figure 2.8) with the MBD simulator. Both control methods were tested using the MBD simulator depicted in Figure 2.7. Then, an experimental manipulator setup was used in a miniature scale to test the control algorithms. The input shaper, the swing angle feedback control, and the swing angle estimator were implemented using the IEC61131-3 ST language. The experimental setup was able to move on one axis only (trolley) because of the attached pulse encoder for angle measurement. The swing angle feedback control was tested using the measured and estimated swing angles.

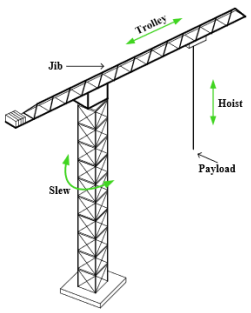

Figure 3.4 Tower crane has three axes of movement: slew, trolley, and hoist (**Publication II**).

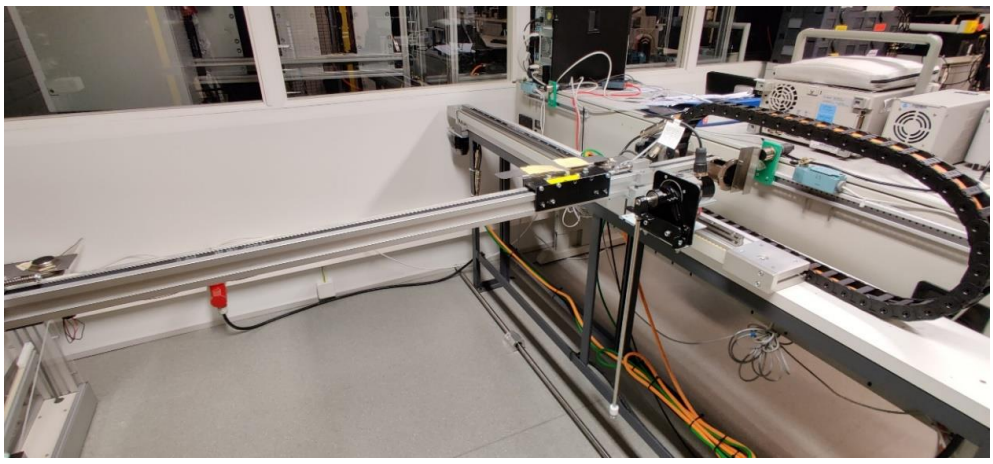

Figure 3.5 Experimental manipulator setup used for testing the swing control algorithms (**Publication II**).

The results show that although the input shaper suppresses load swing, it causes a long lag to the operator's commands. The lag is also dependent on the hoist cable length. This can be difficult to learn to compensate. As an alternative method, an approach based on swing angle feedback control is proposed. According to the results, the suggested method is as effective or better than the input shaper reducing the load swing, without causing a noticeable lag to the operator commands. Although the estimated angle differs from the measured angle, the swing angle feedback works well when using an estimated angle as long as the estimated angle has the same phase and roughly the same amplitude as the measured angle.

The length of the hoist cable naturally varies during lift operations; hence, the control algorithms must adapt to the changes. The hoist cable length can be estimated by using the hoist motor speed and information of the mechanics of the hoist system if the initial position is known. The initial position can be recorded by performing an identification run every time the system is powered on, for example. The robustness of the swing angle-based feedback control with the estimated swing angle for error in the hoist cable length is also presented. According to the results, varying the hoist cable length between 80% and 120% of the actual hoist cable length does not significantly affect the performance of the control.

Using an estimator reduces the need to install sensors to tower cranes; this is beneficial, as extra sensors can be undesired in harsh environmental conditions.

Although a tower crane is used as a case example, the approach can also be adopted to other crane types. For example, overhead cranes (also called bridge cranes) have a similar construction to the experimental setup and have only trolley and hoist movement.

3.3 Generating surface dynamometer card for a sucker rod pump by using frequency converter estimates and a process identification run

In Publication III, a novel method for generating surface dynamometer cards for a sucker rod is presented. The method involves using torque and rotational speed estimates of an induction motor drive and a pumping process identification run. A dynamometer card is a plot of rod force as a function of rod displacement. A surface dynamometer card is produced by the surface dynamometer, located on the top end of the well (on the surface of the ground). Figure 3.6 depicts a surface dynamometer card from an actual sucker rod pump.

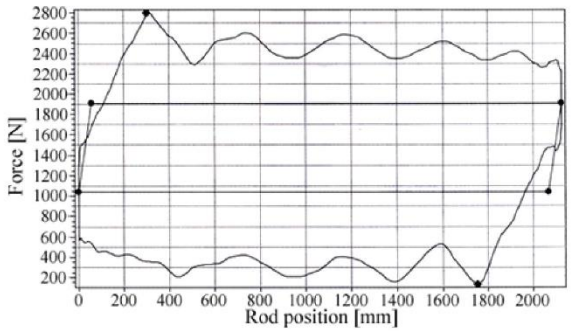

Figure 3.6 Surface dynamometer card of a sucker rod pump (**Publication III**) © 2015 IEEE.

The cards are the main tool for analyzing pumping performance, oil well conditions, and different abnormal operating conditions. A normal procedure to generate a surface dynamometer card is to install force and position sensors and a program that plots the force against rod position. Another way is to use the motor torque signal and calculate the rod force. The calculation requires knowledge of the kinematics of the pumping unit, which can be a drawback as it requires a detailed model of the geometry, and the geometry varies between pumps.

The authors propose a method for revealing the kinematic connections and forces affecting the pump with such an accuracy that the surface dynamometer card can be generated without geometry information only by using the estimates produced by the frequency converter and with one additional limit switch. Figure 3.7 presents a sucker rod pumping system.

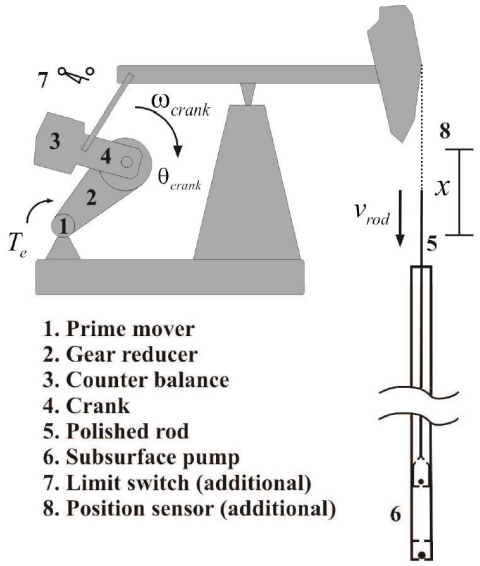

Figure 3.7 Sucker rod pumping system (**Publication III**) © 2015 IEEE.

A simulation model is constructed of the whole pumping system to be able to test the identification-based estimation of the surface dynamometer cards. The block diagram of the model is presented in Figure 3.8.

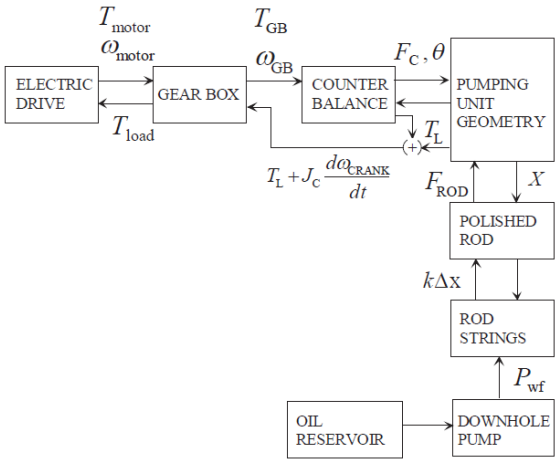

Figure 3.8 Block diagram of the pumping system model (**Publication III**) © 2015 IEEE.

The simulation model contains a detailed frequency converter model with an actual converter control code and a two-axis induction motor model, a pumping geometry with a gearbox, rod strings as a lumped flexible system, a downhole pump, and a simple oil well model as an RC circuit, where the capacitance reserves the inflowing oil that is flowing to the well through a resistance.

The identification procedure is used to establish a correspondence between the rod position and the motor rotor angle incremental during one rod cycle. A limit switch is used to get the rod position in one point of the cycle. The relation of the rod position and the rotor angle is recorded to a lookup table. Further, the "no-load" torque needs to be measured by detaching the polished rod from the string and running the pump.

After the identification run, the pump can be run using the frequency converter estimates for the rotor speed and torque. The rod position can be calculated by using an integral of the rotor speed and the lookup table formed using the identification run. The rod force can then be calculated as shown in Figure 3.9 .

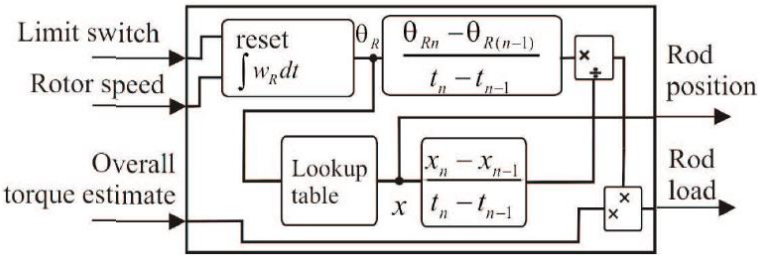

Figure 3.9 Scheme for the operational run of the sucker rod pump (**Publication III**) © 2015 IEEE.

The simulation results show that the surface dynamometer cards created after performing the identification run (and running the model: "operational run") and using the original parameters in the simulation model correspond with a good accuracy. The curve resulting from the identified system covers the area with a 99% accuracy, Figure 3.10.

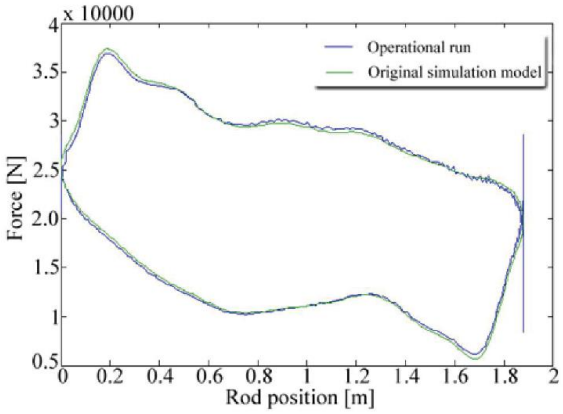

Figure 3.10 Dynamometer card comparison (**Publication III**) © 2015 IEEE.

Most other methods require quite complicated instrumentation and devices to record load values applied to the polished rod and to obtain the rod position. This novel method uses rotational speed and torque estimates from the frequency converter and the correspondence identified between the torque and the load for the calculation of the load that the polished rod undergoes. The only measurement device that has to be added to the pump is a limit switch. The polished rod force can be calculated in the frequency converter or in an automation device, such as a PLC.

3.4 Dynamic performance of mechanical-level hardware-in-the-loop simulation

In **Publication IV**, the dynamic behavior, stability, and performance issues of the mechanical-level hardware-in-the-loop (MHIL) simulation are discussed. A mechanical-level HIL is a type of HIL simulation in which the complete drive system is under test and a real-time simulator is emulating the load for the device under test. MHIL simulation can be used, for example, for testing electric drivetrains or their control.

Mechatronics systems driven by controlled electric drives can be analyzed without actual mechanics by virtual testing. This co-simulation can employ multibody dynamics simulation and mechanical-level hardware-in-the-loop simulation, Figure 3.11.

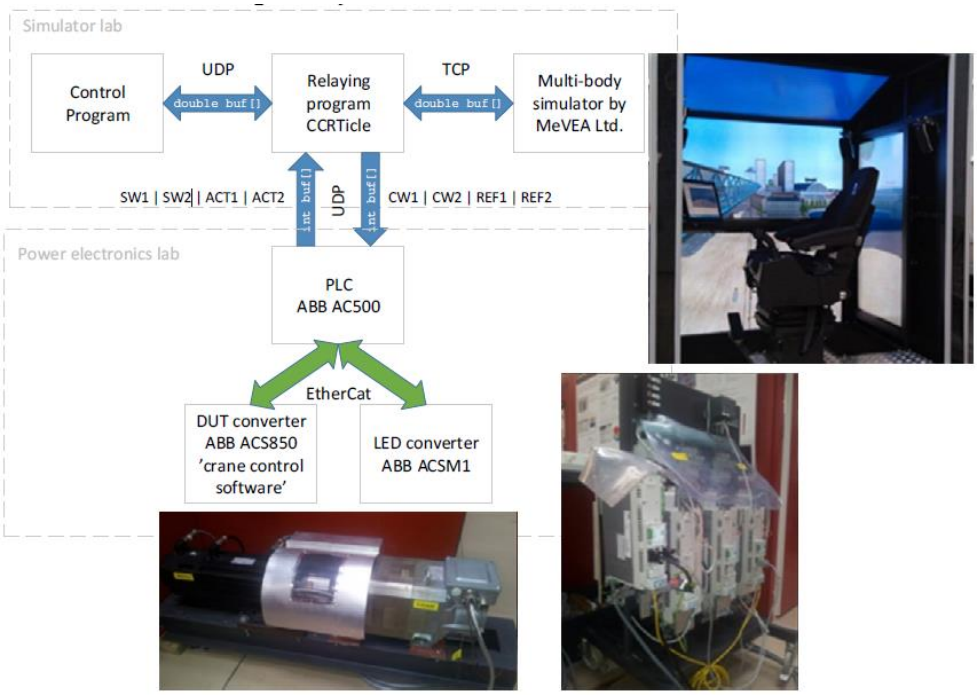

Figure 3.11 Laboratory HIL setup with an MBD model of a tower crane, the slew motor of the crane as an actual hardware with a loading motor (**Publication IV**) © 2014 IEEE.

A laboratory setup consisting of two electric drives, a load-emulating drive (LED) and a device under test (DUT), a PLC, and connection and control software, is used to

investigate the performance and stability of the MHIL. In Figure 3.12, the system is illustrated with a block diagram.

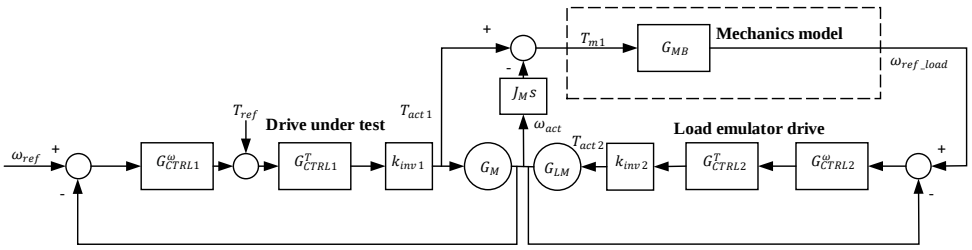

Figure 3.12 Block diagram of the MHIL system. Software components are enclosed in a dashed-line box.

The DUT drive is the part "taken out of the simulation loop," in this case, the slew motor of a tower crane. Often, a DUT is driven by a torque reference signal instead of a speed reference signal. The actual torque of the DUT drive is fed to the mechanics model, which, in this case, was a simple second order transfer function or a multibody dynamics simulator running a model of a tower crane. The mechanics model calculates the speed, in this case, the rotational speed of the slew motor, and feeds it as a speed reference signal to the LED drive, which is acting as the load for the DUT drive.

This type of setup can be used for testing actual components in virtual environments. Instead of applying the control algorithms to a frequency converter running a real tower crane, we can run the algorithms in a frequency converter running a virtual tower crane. This makes it safer, faster, and easier to develop algorithms than using actual hardware, such as a tower crane, as development and testing can be carried out in laboratory conditions. In addition, a real load cycle can be used as a human operator can drive the machine in real time.

In this study, it was found that the dynamics of the application mechanics with the DUT and the MHIL differ from each other, and the dynamics of the DUT and the LED affect the overall dynamics of the MHIL setup. Furthermore, different LED drive control parameters are needed for different DUT drive control parameters. In the laboratory tests, it was possible to achieve unstable behavior of the HIL setup even though the reference model of the DUT and mechanics were stable. The unstable behavior could also be predicted by means of frequency response analysis. It was also concluded that it is important that the LED follows the speed reference signal accurately; otherwise, the HIL setup does not emulate the real machine. Of course, transients can cause some difference between the speed reference and the actual speed of the LED, but the error should become zero in the steady state. This error signal can be used for monitoring the performance of the HIL.

3.5 Comparison of different power balance control methods for battery energy storage systems in hybrid marine vessels

In **Publication V**, different power balancing methods for hybrid marine vessels are analyzed. First, the power grid of the vessel is modeled using MATLAB and Simulink. Figure 3.13 depicts the top layer of the model. The simulation model includes models for the gensets, the battery energy storage system (BESS), the power grid (cables), the propulsion load, and the hotel load (the static load of the ship, other than propulsion). The power control block contains the power balancing algorithms currently under test.

The diesel genset (DG) model is divided into two parts: the diesel engine and the generator. The diesel engine is modeled using transfer functions for the fuel actuator dynamics, the fuel feed dynamics, and the turbo charger dynamics. The longest delay of the diesel engine model is the turbo charger delay. The generator model is a Simscape library block of a synchronous generator.

The propulsion load is a Simscape library rectifier model with a DC link model and a controlled current source model that can draw the propulsion power from the power grid. The power grid is modeled using Pi-section cables, and the hotel load is a static 3-phase load from the Simulink component library.

The BESS model consists of the battery model and the grid inverter model. The battery model is a Simscape library battery model. The grid inverter model is built from fundamental blocks. The grid inverter uses a phase-locked loop to keep track of the grid angle, and the model does not contain power switch models; it is an averaging model. It is controlled by the i_d current reference.

This model combines different levels of model complexity, and some subsystems of the model are built from fundamental blocks and some parts are ready-made library blocks. This shows the power of modern simulation tools, as relatively complex models can be built with ease. Often, the challenge comes from parametrizing the components, as detailed data sheets of components can be difficult to find. The authors decided to make the model of the power grid as detailed as possible. Hence, detailed models for the electrical components were used, such as the Simscape components for the generator, battery, transformers, cables, and propulsion load components. This enabled to study the simulated voltages, currents, and frequency of the power grid. Accurate modeling of the diesel engine would have been a massive task, and furthermore, there would have been the problem of finding parameters for the model. In this case, the transfer function model describes the dynamic response of the diesel engine, which is enough as the diesel engine itself is not under investigation. Then, the diesel engine could be tuned according to the manufacturer data to give a similar response.

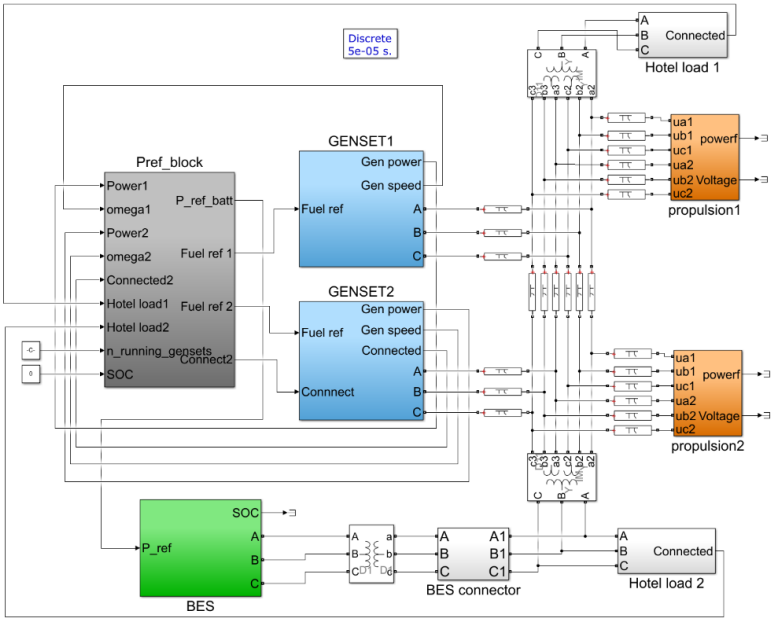

Figure 3.13 Simulink model of a ship power grid, containing models for gensets, battery energy storage, hotel load, and propulsion load (**Publication V**) © 2022 IEEE.

Different control methods were implemented and tested using dynamic positioning load data obtained from a real offshore supply vessel (OSV) as input data. Dynamic positioning (DP) is a mode in which the OSV uses thrusters to stay in position relative to the seabed or a moving object. In the DP mode, the propulsion power is low on average, but it is very dynamic. This causes challenges to conventional OSV power distribution systems without a BESS. In this paper, isochronous control is investigated as a control method for the BESS as it is used in conventional systems with diesel engines. This would enable easier retrofitting of the BESS to existing diesel-powered systems. Another control method for the BESS was a load-power-estimation-based method in which the difference between the nondelayed and delayed load power was used as the power reference to the BESS. This makes the BESS react to sudden changes in load power, but if the change remains, the power reference to the BESS decreases and the diesel gensets increase their power.

The simulation results show that the OSV could turn off one DG in the DP mode when it was using the BESS for power peak shaving. Without the BESS, the OSV needed two DGs to respond to the load changes caused by the thrusters. The tested power balancing methods were able to distribute power between the BESS and the DGs. The average load power estimation method is good for peak shaving as it reacts immediately to load power changes as the isochronous control reacts when there is a control error forming.

Isochronous control could be easier to implement on a retrofit vessel as it is already in use for DGs

4 Conclusions

This doctoral dissertation addressed modeling of mechanical systems driven by an electric drive, using case studies of different simulation, modeling, and control challenges and solutions. In the studied cases, first, a model of the system was built. Different methods were used to obtain the system model. The system model could be identified in one case. In one case, a multibody dynamics model was used to describe a mechanical system. In the other cases, the model was built by using existing knowledge of the system and combining fundamental and library blocks of the simulation software. Importantly, the model could describe the phenomena that were of significance when considering the research question of each case, without being overly complicated. Building of the models was based on analyzing the application and thereby identifying the modeling questions. Thus, a suitable model could be selected based on the requirements set by the research question. Different applications and different research questions obviously require the use of a different type of model.

After the system model was established, the system could be simulated, and control design could be started. Different simulation methods were used for testing and development of control algorithms. In **Publication II**, virtual simulation using a multibody dynamics simulator connected to a computer running a control program was used to test and compare the presented methods. This type of simulation is known as software-in-the-loop (SIL) simulation. In **Publication III** and **Publication V**, a commercial simulation software was used to run the simulation model, and the developed methodology and control algorithms were tested against the simulation model.

Experimental verification of the selected modeling methods indicated that the selection procedure was successful in all the presented cases. In the case of **Publication III**, the applied model represented the mechanics of the pumping system with such an accuracy that a methodology for generating surface dynamometer cards could be established. In addition, the use of a detailed electric drive model assisted in evaluating the effects of nonlinearities in the inverter control. In the case of **Publication II**, the use of a multibody dynamics model would not have been necessary; a pendulum-type model could have been built to describe the payload swing dynamics with a sufficient accuracy, as there is already an abundance of published research material available. However, the use of a virtual simulator assisted in the evaluation of the operator experience of the control, as the virtual crane could be driven in real time in a real environment to experience the behavior of the control and the crane. In the case of **Publication IV**, the transfer functions used described the MHIL system with a sufficient accuracy so that by applying them, it was possible to determine the point when the mechanical part becomes unstable. In the case of **Publication V**, a detailed enough vessel power distribution system model was built to be able study the network frequency and also voltages and currents. However, as the model was already computationally heavy, some simplifications were made, for example, the diesel engines were replaced by fuel and air dynamics modeled using transfer functions. Furthermore, propulsion drives were replaced by power sources sinking power from the

grid. This made the model computationally lighter and reduced the need for parametrization.

Parametrization of models is often challenging in the modeling. When a detailed model is required, it often contains numerous blocks, and they require numerous parameters. These parameters can be hard to find, or they can be confidential. Some parameters are not constant, and their values change during the simulation depending on the state of the simulated system. This further complicates the task of finding suitable values for the parameters. If the model contains numerous parameters with inaccurate values, the overall accuracy of the model will suffer. Thus, some other approach could be considered, with fewer uncertain parameters, which would, despite this, describe the studied phenomena.

4.1 Future research

Modeling, simulation, and control of mechatronic systems is a multidisciplinary science and requires a system engineering level of knowledge about mechanics, electric drives, control engineering, and automation. Although modern simulation and modeling tools, such as Simulink, contain numerous premade library blocks for describing different components, a common methodology would be required for modeling. For example, component manufacturers could provide components with standardized interfaces. Then, a company specialized in system integration could use the provided models to build a model of the whole system.

One interesting question is the use of artificial intelligence in modeling. Artificial intelligence could use the above-mentioned standardized interfaces to build complete models from submodels. The aspect of automated modeling or artificial intelligence in modeling and simulation itself is not a new idea (Xia, 1996) (Zeigler, 2009). However, it has not become a popular tool for generating simulation models. Nevertheless, it will be interesting to see how modeling systems will change when artificial intelligence is used more widely in different applications.

References

Aarniovuori, L. 2010. *Induction Motor Drive Energy Efficiency - Simulation and Analysis.* Doctoral dissertation. *Acta Universitatis Lappeenrantaensis 396.* Lappeenranta University of Technology. Lappeenranta, Finland.

ABB 2013. *ABB Motion.* [Online]. [Accessed 21 June 2021]. Available from: http://abbmotion.com/support/faq.asp?ItemID=135

Ahonen, T., Tamminen. J., Niinimäki. L., Mar. C. A. A., and Niemelä. M. 2013. ”Estimation accuracy of a vector-controlled frequency converter used in the determination of the pump system operating state.” In *2013 15th European Conference on Power Electronics and Applications (EPE)*. 2–6 June, Lille, France, pp. 1–10.

Aromaa, S., Leino. S.-P., and Viitaniemi. J. 2014. *Virtual protyping in human-machine interaction design*, [Online]. [Accessed 30 June 2022]. Available from: https://publications.vtt.fi/pdf/technology/2014/T185.pdf

Bubert, A., De Doncker, R. W., Kauffman, P. and Au, A. 2014. “Application-oriented design of mechatronic drive trains.” In *2014 IEEE International Conference on Mechatronics and Automation.* 3–6 June, Tianjin, China.

Capitol Technology University 2018. *The Evolution of Mechatronics Engineering | Capitol Technology University*. [Online]. [Accessed 18 May 2022]. Available from: https://www.captechu.edu/blog/evolution-of-mechatronics-engineering

Caruntu, C. -. F., Balau, A. -. E. and Lazar, C. 2010. “Cascade based control of a drivetrain with backlash.” In *2010 12th International Conference on Optimization of Electrical and Electronic Equipment.* 20–22 May, Brasov, Romania.

Comsol 2016. *The Finite Element Method (FEM).* [Online]. [Accessed 06 May 2021]. Available from: https://www.comsol.com/multiphysics/finite-element-method

Harnefors, L., Saarakkala, S. E. and Hinkkanen, M. 2013. ”Speed Control of Electrical Drives Using Classical Control Methods.” *IEEE Transactions on Industry Applications*, 49(2), pp. 889–898.

IGI Global 2022. *What Is Mechatronic System | IGI Global.* [Online]. [Accessed 12 May 2022]. Available from: https://www.igi-global.com/dictionary/digital-and-mechatronic-technologies-applied-to-the-survey-of-brownfields/48869

Jokinen, M., Saarakkala, S., Niemelä, M., Pöllänen, R., and Pyrhönen, J. 2008. ”Physical drawbacks of linear high-speed tooth belt drives.” In *International Symposium on Power Electronics, Electrical Drives, Automation and Motion.* 11–13 June, Ischia, Italy, pp. 872–877, doi: 10.1109/SPEEDHAM.2008.4581140.

Kotuszewski, P. Kukielka, K., Kluk, P., Ordys, A., Bieńkowski, K., Kościelny, J. M., Syfert, M., Wnuk, P., Możaryn, J., and Fajdek, B. 2021. “Cyber-Security Assessment of Industry 4.0 Enabled Mechatronic System.” *Complexity,* Issue Emerging Trends in Mechatronics, doi: 10.1155/2021/6670625.

Kovács, P. K. 1984. *Transient Phenomena in Eletrical Machines.* Budapest: Elsevier.

Leonhard, W. 2001. *Control of Electrical Drives.* 3rd Edition. Berlin: Springer.

Lindh, T. 2013. “Simulation, modeling, and virtual testing of electric-drive-powered mechatronic systems.” In *2013 International Conference-Workshop Compatibility And Power Electronics.* 5–7 June, Ljubljana, Slovenia, doi: 10.1109/CPE.2013.6601158.

Lindh, T., Montonen, J.-H., Grachev, M. and Niemelä, M. 2015. “Generating surface dynamometer cards for a sucker-rod pump by using frequency converter estimates and a process identification run.” In *2015 IEEE 5th International Conference on Power Engineering, Energy and Electrical Drives (POWERENG).* 11–13 May, Riga, Latvia, doi: 10.1109/PowerEng.2015.7266353.

Ljung, L. 1987. *System Identification: Theory for the user*. Englewood Cliffs (NJ): Prentice-Hall.

Luukko, J., Haverinen, V., Ruuskanen, V., Lindh, T., Pöllänen, R., Kärkkäinen, V., Tiainen, R., Paakkonen, M., and Pyrhönen, O. 2009. ”Simulation package for simulating wind power drives.” In *2009 13th European Conference on Power Electronics and Applications.*

Mladenov, V. 2009. “Prediction of Limit Cycles in nonlinear systems with ideal relay type nonlinearities by using Multiple-input Describing Functions.” In *13th WSEAS International Conference in SYSTEMS.* [Online]. [Accessed 30 June 2022]. Available from: https://www.researchgate.net/publication/228815548_Prediction_of_limit_cycles_in_nonlinear_system_with_ideal_relay_type_nonlinearities_by_using_multiple-input_describing_functions

Mohamed, Y. A. I. 2006. “Adaptive Self-Tuning Speed Control for Permanent-Magnet Synchronous Motor Drive With Dead Time.” *IEEE Transactions on Energy Conversion*, 21(4), pp. 855–862.

Montonen, J., Montonen, J.-H., Immonen, P., Murashko, K., Ponomarev, P., Lindh, T., Lindh, P., Laurila, L., and Pyrhönen, J. 2012. ”Electric drive dimensioning for a hybrid working machine by using virtual prototyping.” In *2012 XXth International Conference on Electrical Machines.* 2–5 September, Marseille, France, doi: 10.1109/ICElMach.2012.6349986.

Montonen, J.-H. and Lindh, T. 2014. “Analysis of sensorless traction control for electric vehicle.” In *2014 16th European Conference on Power Electronics and Applications*. 26–28 August, Lappeenranta, Finland, doi: 10.1109/EPE.2014.6911006.

NASA, 2009. *The Art and Science of Systems Engineering.* [Online]. [Accessed 18 May 2022]. Available from: https://www.nasa.gov/pdf/311199main_Art_and_Sci_of_SE_SHORT_1_20_09.pdf

Nevaranta, N., Parkkinen, J., Lindh, T., Niemelä, M., Pyrhönen, O., and Pyrhönen, J. 2015. ”Online Estimation of Linear Tooth Belt Drive System Parameters.” *IEEE Transactions on industrial electronics,* 62(11), pp. 7214–7223, doi: 10.1109/TIE.2015.2432103.

Saarakkala, S., Haapala, M., Jokinen, M., Niemelä, M., Pöllänen, R., Pyrhönen, J. 2009. ”Performance, limitations, and control of a high-speed tooth belt drive in a motion control application.” In *IEEE EUROCON 2009. 18–23 May, St. Petersburg, Russia*, doi: 10.1109/EURCON.2009.5167731.

Sierra-García, J. E., Santos. M. 2020. “Mechatronic Modelling of Industrial AGVs: A Complex System Architecture.” *Complexity,* Issue Emerging Trends in Mechatronics, doi: 10.1155/2020/6687816.

Slotine, J.-J. E., Li, W. 1991. *Applied nonlinear control.* Englewood Cliffs (NJ): Prentice-Hall.

Tiainen, R., 2010. *Utilization of a Time Domain Simulator in the Technical and Economic Analysis of a Wind Turbine Electric Drive Train.*Doctoral dissertation. Acta Universitatis Lappeenrantaensis 391. Lappeenranta University of Technology. Lappeenranta, Finland.

Úředníček, Z., 2018. Describing functions and prediction of limit cycles. *WSEAS Transactions on systems and control*, Volume 13, pp. 432–446.

Xia, S., and Smith. N. 1996. “Automated modelling: a discussion and review.” *The Knowledge Engineering Review*, 11(2), pp. 137–160, doi: 10.1017/S0269888900007803

Younkin, G. 1989. “Modeling machine tool feed servo drives using simulation techniques to predict performance.” In *Conference Record of the IEEE Industry Applications Society Annual Meeting.* 1–5 October, San Diego, CA, USA, doi: 10.1109/IAS.1989.96870.

Zeigler, B. P., Muzy. A., and Yilmaz. L. 2009. “Artificial Intelligence in Modeling and Simulation.” In R. A. Meyers, *Encyclopedia of Complexity and System Science.* New York: Springer. pp. 344–368.

Åström, K. J. and Wittenmark, B. 1995. *Adaptive control.* 2nd edition. Reading (MA): Addison-Wesley.

Publication I

Montonen, J.-H., Nevaranta, N., Lindh, T., Alho, J., Immonen, P., and Pyrhönen, O.
Experimental Identification and Parameter Estimation of the Mechanical Driveline of a Hybrid Bus

Reprinted with permission from
IEEE Transactions on Industrial Electronics
Vol. 65, pp. 5921–5930, 2018

Experimental Identification and Parameter Estimation of the Mechanical Driveline of a Hybrid Bus

Jan-Henri Montonen, Niko Nevaranta, *Member, IEEE*, Tuomo Lindh, Jani Alho, Paula Immonen and Olli Pyrhönen

***Abstract*—Driveline resonances are one of the major reasons for poor vehicle drivability, passenger discomfort, and premature wear of the mechanical parts of the driveline. Adequate models generated by system identification are essential, for instance, in order to analyze resonances, and especially, to design solutions to mitigate these adverse effects by means of control. In this paper, the resonating mechanical driveline of a hybrid city bus is identified by feeding different excitation signals such as pseudo-random binary signal, stepped sine, and chirp to the driveline and by measuring the frequency response at a standstill and during on-road experiments. The identification experiments are conducted by operating the bus in the series electric hybrid mode, that is, in an operating mode that corresponds to a full electric mode powered by energy storages. Resonating two-mass system models are parametrized based on the obtained frequency responses and used to validate the identification experiments.**

***Index Terms*—Driveline resonance, Hybrid bus, System Identification, Parameter Estimation**

I. Introduction

ELECTRICAL drives constitute an essential element of drivelines in modern mobile technologies such as hybrid and electric vehicles. In recent years, electrically powered vehicles have been a topic of intense discussion and research, in particular with respect to batteries [1], power electronics [2], and electric motors [3], resulting in well-established concepts for the manufacture of highly advanced electric powertrains. Well-designed integration of electrical drives into mobile applications has resulted in significant improvements in energy efficiency and better performance. Unfortunately, a typical problem encountered with electrically powered vehicles is related to driveline oscillations caused by flexibility associated with the couplings of the mechanical structure. Depending on the drive train design, the most crucial first eigenfrequencies, in particular, the dominant mechanical resonances, are typically in the range from 5 Hz to 50 Hz at low frequencies [4]. These adverse effects can cause vehicle drivability issues, which may pose challenges for the control design [5]. For these reasons, appropriate system identification techniques may provide viable solutions for commissioning of such drives. Moreover, as electrically powered mobile technologies are becoming more prevalent, the development of system-identification-based commissioning and maintenance tools is a task worth pursuing.

System identification of resonating mechanical loads in electric drives has been a topic of intense research over the past few decades; this has been explained by the ever-increasing need for model-based control in demanding industrial control applications. Owing to the widespread adoption of electrically powered vehicles and the integration of electrical drives with a high calculation capacity into mobile technology, provide an opportunity to implement various artificial excitation-based identification schemes as part of control electronics. Thus, these schemes offer a viable solution for commissioning of such drives. Further, from the viewpoint of preventive safety systems in automotive applications, these identification approaches make it possible to detect changes in the mechanical system as a proactive maintenance action before they lead to performance degradation or device failure.

Similar types of identification routines have been applied to the identification of vehicle driveline dynamics, but not to the same extent as for industrial applications discussed above. Therefore, only a few studies are available on the topic in the literature. In [4]–[7], nonparametric identification of nonlinear drivelines of electric vehicles is studied by exciting the mechanical system by pseudo-random binary sequence (PRBS) test signals. For the purposes of controller design, these identification problems have been treated as linear time invariant (LTI) ones in order to have a simple model of the drivetrain. In [8], a prediction-error-based parameter identification approach is adopted to estimate physical parameters such as spring and damping constants and inertia of a truck driveline. Another approach is introduced in [11], where an autoregressive moving average with an exogenous inputs (ARMAX) model is applied to identify a linear model for the driveline dynamics. The option for online estimation of the driveline dynamics is also addressed in [12] by considering an extended Kalman filter (EKF), which is a widely recognized approach for systems with nonlinear dynamics. A modal identification algorithm for a multi-inertia driveline system is proposed in [13]; the algorithm can be generalized to various types of multi-inertia systems or drivetrains.

In the controller design, an appropriate driveline model is essential for damping of driveline oscillations as has been

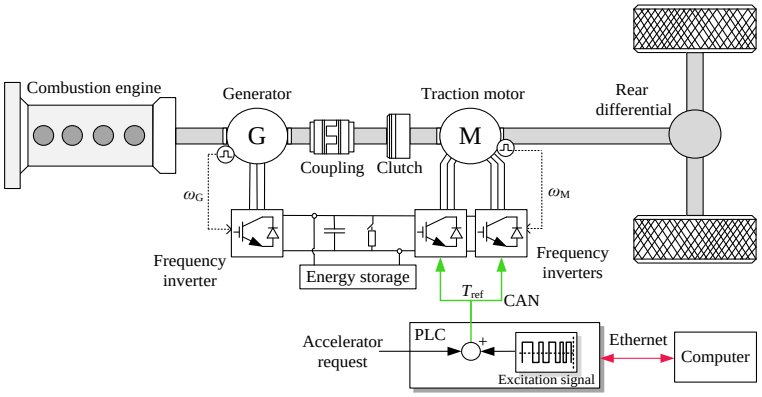

Fig. 1. Principle of the identification of a mechanical driveline in the series electric mode. The excitation signal is superposed to the torque reference of both the frequency inverters of the traction motor.

shown in simulation-based studies in [10]–[14]. In particular, the significance of an accurate model is demonstrated in [15], where the performance of the proposed active damping controller has been analyzed under system parameter changes. This paper focuses on issues in the system identification of a mechanical driveline of a hybrid bus, which is operated in the series electric mode. The identification is performed by injecting excitation signals to torque references of the traction motor control. By applying the estimated frequency responses, a parametric two-mass model is fitted from the frequency-domain observations to obtain a model for the dominant resonance frequency.

Motivated by the parameter estimation routines proposed in [16], [21] for the identification of resonating mechanical loads in electric drives, the objective of this paper is to study the parameter estimation of a mechanical driveline model of a hybrid bus. The identification problem of a resonating driveline of a mobile vehicle is addressed by using artificial excitation signals. The case differs from the typical industrial identification examples discussed in the literature [16], [21], [22], [24]. A similar type of parameter estimation routines based on an output-error (OE) model structure and a Least-Squares (LS) algorithm of Levenberg and Marquardt (LM) as proposed in [16] and [21] is considered; in this paper, however, the estimation is carried out in the frequency domain for both approaches, and an error function criterion is considered that improves the model fit in the low-frequency region. Moreover, in order to initialize the parameter estimation routines, supporting tests such as acceleration, deceleration, and standstill identification tests are discussed.

This paper is organized as follows. Section II describes the problem statement and introduces the driveline of the hybrid bus under study. In addition, identification of the mechanical driveline in the series electric mode is discussed. In Section III, the identification problem is considered, and approaches to identify the mechanical driveline are studied. In Section IV, experimental identification results are reported and analyzed, and Section V concludes the paper.

II. Problem Statement

Depending on the design of the mechanical driveline, mechanical components may produce very low-frequency oscillations due to the structure of the system. These torsional oscillations are typically generated by flexible structures, such as rotating masses coupled to the driving motor by shafts and gearboxes. The main driveline dynamics is obtained from the flexible driveshaft acting as the main source of resonance. In order to mitigate the effect of these oscillations, an adequate driveline model is a prerequisite to constructing observers or designing controllers. System identification approaches may offer a viable solution for commissioning of such a drive. In this paper, the problem of identification of a resonating mechanical driveline of a hybrid bus is addressed.

A. Mechanical Driveline

The components of the mechanical driveline are shown in Fig. 1. A 2.5L diesel engine (combustion engine) rotates a 55 kW outer-rotor permanent magnet (PM) generator. The generator and the traction motor can be coupled by an electrically operated clutch. A six-phase 150 kW PM traction motor is connected with a Cardan shaft running the differential and drive shafts. The driveline can be operated in three modes: diesel-only, parallel electric hybrid, and series electric hybrid. In the diesel-only mode, the clutch is coupled and the traction motor and the generator are rotating freely. In this operating mode, the diesel engine produces all the power required to move the bus. Correspondingly, in the parallel electric hybrid mode, the clutch is still coupled, but the diesel and the traction motor produce the driving power. Finally, in the series electric hybrid mode, the clutch is uncoupled and only the traction motor is connected to the driving wheels. In this mode, the diesel engine rotates the generator only when needed, that is, when the energy storage (battery pack) requires charging.

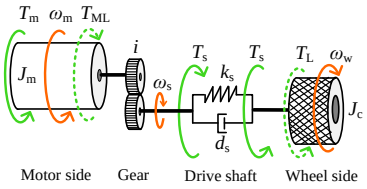

Fig. 2. Simplified two-mass driveline model.

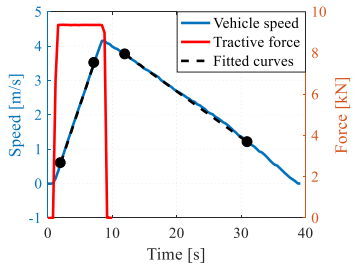

Fig. 3. Acceleration and deceleration test to identify the total inertia and friction forces. Fitted curves are used to determine the parameters.

B. Drive control system

The generator and the traction motor are controlled by frequency inverters connected to the energy storage system as depicted in Fig. 1. The six-phase traction motor is fed by two frequency inverters. In this paper, the overall control strategy of the hybrid bus is not discussed in detail, but only from the viewpoint of system identification experiments. The torque is controlled by the current controller of the inverter, which produces a minimum current rise time of approximately of 3 ms. Therefore, the bandwidth of the control limits the identification bandwidth to be approximately 100 Hz. Naturally, if the main purpose of the identification is to be able to reduce oscillations with a model-based control, it can only be done within the control bandwidth.

Finally, the identification of the mechanical driveline is studied in the series electric hybrid mode only, and thus, the coupling between the generator and the traction motor is open during the tests. Hence, the driveline dynamics is identified from the traction motor to the driving wheels. A programmable logic controller (PLC) is used for data acquisition and to implement the excitation signals, controllers, and references.

C. Driveline modeling

In many industrial applications, the mechanical loads of electric drives have been successfully approximated as resonating two- or three-mass systems in order to simplify the overall system modeling by taking only into account the dominant resonance frequencies [16], [21]. In this study, a resonating two-mass model is considered as a reference model for the driveline and the model structure to be estimated. As the drivability of a vehicle is mostly influenced by the low-frequency range [4], which is approximately 0–50 Hz, the possible higher resonance frequencies are not considered in this paper. It is also assumed that the main flexibility of the driveline is found on the drive shafts, represented by the spring and damping coefficients k_s and d_s. Based on these assumptions, the driveline modeling is simplified to a resonating two-mass system, as depicted in Fig. 2. Hence,

$$J_m\dot{\omega}_m = T_m - \frac{T_s}{i} - T_{ML} \tag{1}$$

$$J_c\dot{\omega}_w = T_s - T_L \tag{2}$$

$$T_s = k_s\cdot(\theta_s - \theta_w) + d_s\cdot(\omega_s - \omega_w) \tag{3}$$

where J_m is the total inertia of the motor-side driveline components, T_m is the motor torque, T_s is the torque on the driveshaft, and ω_m, ω_s, and ω_w denote the angular velocities of the motor, driveshaft, and wheels. The angular positions of the driveshaft and the wheels are θ_s and θ_w, respectively. The loading torques acting on the motor and the wheels are denoted by T_{ML} and T_L. The overall gear ratio i of the driveline components (i.e., differential) is used to transform the velocities $\omega_m = i\cdot\omega_s$ and the torques. J_c represents the total inertia of the wheels and the chassis as

$$J_c = J_{\Sigma w} + m_v r^2 \tag{4}$$

where $J_{\Sigma w}$ is the total inertia of the wheels, m_v is the mass of the vehicle, and r is the radius of the wheel. The parameters given in Table I are taken as reference system parameters for the mechanical driveline obtained from the geometrical and material properties and experimental tests.

Acceleration and deceleration tests were undertaken to produce the total inertia estimate and identify the friction forces affecting the vehicle. In these tests, the vehicle was accelerated applying a constant torque (and constant traction force), after which the vehicle was allowed to decelerate to a standstill by the effect of friction forces as depicted in Fig. 3. Thus, the friction force can be calculated from the deceleration part and then take that value to compensate for the friction forces of the acceleration test. The straight lines were fitted on the velocity curve slopes by the least-squares method. Multiple tests were done to ensure the validity of the estimates, and based on the slopes, a total mass estimate m_Σ = 12350 kg and a friction force estimate F_μ = 2420 N were obtained. The estimated friction

TABLE I
REFERENCE PARAMETERS OF THE DRIVELINE MODEL

Symbol	Parameter	Nominal value[1)]
J_w (kgm^2)	Wheel inertia	22.1**
k_s (kN/m)	Spring constant	1520
m_C (kg)	Vehicle mass	12350***
d_s (Ns/m)*	Damping constant	3600
f_{res} (Hz)	Resonance frequency	10
i	Gear ratio	8.79**
r (m)	Wheel radius	0.45**
J_m (kgm^2)	Motor side inertia [18]	4.5

* Damping has been approximated by following the guidelines given in [21].
** Values given by manufacturers, *** Also been determined by using truck scales during vehicle inspection.

force corresponds to the load-side torque term, the velocity-dependent friction part of T_L. In this paper, these estimates are applied to initialize the parameter estimation routines. The acceleration and deceleration tests with a constant torque reference can also determine whether a traction motor produces a cogging torque component that is enough to excite resonances at certain speeds. In this case, a velocity measurement did not reveal any such component, as expected, based on the skewed stator design of the traction motor [18].

Fig. 4. Hybridized city bus is as a test vehicle.

III. Identification of the Mechanical Driveline

Identification of resonating mechanical loads in electric drives is a widely studied research topic because of the broad range of applications [16], [20]–[26], in which accurate models are essential for the control design. These methods are also applicable to the identification of mechanical drivelines in modern mobile equipment.

A. Nonparametric identification

Depending on the information available on the system dynamics, it is often a good starting point to perform a nonparametric model identification such as a frequency response analysis. In general, the frequency response estimate can be expressed by the ratio of the auto-spectral density function $S_{uu}(j\omega)$ of the input signal $u(k)$ and the cross-spectral density function $S_{uy}(j\omega)$ of the input and output $y(k)$ as

$$\hat{G}(j\omega) = \frac{\hat{S}_{uy}(j\omega)}{\hat{S}_{uu}(j\omega)}. \quad (5)$$

The spectral analysis can be made in several ways, for example by the Welch method [16], the correlogram method [17], and the periodogram method to name but a few. In this paper, the Welch method is applied to estimate the spectral density functions with a chosen window size. Numerous identification experiments are conducted, and frequency responses are identified from them to ensure the validity of the results.

B. Excitation signals

Typically, the system identification of vehicle dynamics is based on input-output data gathered from on-road experiments, taking road excitations as an input and vehicle responses as an output to be used in the identification process [9], [19]. However, to get adequate results, the excitation should be rich enough in frequencies to excite all the modes in the system. For this reason, artificial test signals, such as a pseudo-random binary signal (PRBS) [21] or multi-sine [24], are commonly employed when the natural input to the system does not provide sufficient system excitation for identification. In this paper, the excitation signals applied during standstill and on-road experiments are PRBS, chirp, and stepped sine.

In general, in automotive applications, the differential gear backlash is a typical source of nonlinearity in the mechanical driveline. In order to prevent the presence of nonlinear backlash in the identification results, the PRBS should be superposed to an offset torque that is always at least as high as the amplitude of the PRBS. Note also that the pulses in the PRBS should not be designed to be too wide in order to prevent the backlash phenomenon. Thus, the excitation signal design for automotive applications with such a nonlinearity is always case specific and may require several experimental trial-and-error attempts.

C. Parameter estimation in the frequency domain

In this paper, the parameter estimation is based on frequency-domain observations; in other words, a two-mass model is fitted to the measured frequency responses. The parameter estimation can be made by using frequency-domain data and solving the identification problem

$$\hat{\theta} = \arg\min_{\theta} V(\theta) \quad (6)$$

with

$$V(\theta) = \sum_{i=1}^{N} \left| G_{\text{meas}}(e^{j\omega_i}) - G_{\text{model}}(e^{j\omega_i}, \theta) \right|^2 \quad (7)$$

where $G_{\text{meas}}(e^{j\omega_i})$ is the measured frequency response available in a particular frequency grid denoted by frequencies ω_i, $i = 1,\ldots, N$ and the model function $G_{\text{model}}(e^{j\omega_i}, \theta)$ to be fitted. By considering a discrete-time polynomial model with an OE model structure, the model function numerator is $B(e^{j\omega_i}, \theta)$ and the denominator $F(e^{j\omega_i}, \theta)$, respectively.

For comparison purposes, the Least-Squares algorithm of Levenberg and Marquardt (LM) is also applied to the parameter estimation. This method has been widely used in the literature [16], [20]–[22] for the identification of the resonating mechanical system of an electric drive in the commissioning phase. To put more emphasis on the reliable frequencies, the error function is weighted by the coherence γ, and to compensate for the scarcity of data in the low-frequency region, the error function is weighted by the inverse of the frequency f. Thus, (7) is converted into the following form in the case of the both parameter estimation routines

$$V(\theta) = \sum_{i=1}^{N} \frac{1}{f} \cdot \gamma(f)^2 \cdot \left| \ln\left(G_{\text{meas}}(e^{j\omega_i})\right) - \ln\left(G_{\text{model}}(e^{j\omega_i}, \theta)\right) \right|^2 \quad (8)$$

Because there are differences in the frequency response gains, the errors can be more equally distributed over the frequency range of interest by considering the logarithm of the model functions (8). It is emphasized that this modification affects only the gain and not the phase. Further, both the parameter estimation algorithms are initialized by an initial

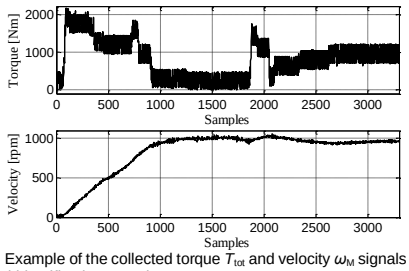

Fig. 5. Example of the collected torque T_{tot} and velocity ω_M signals in the on-road identification experiments.

model, with the parameters corresponding to the reference model given in Table I.

IV. Experimental Results

The experimental identification tests were run on a hybridized city bus test vehicle shown in Fig. 4 both at a standstill and during on-road operation. An AC500 programmable logic controller (PLC) manufactured by ABB was chosen to generate the excitation signals. Signal generators for the PRBS and sine signal (fixed frequency and chirp) were implemented in the PLC code as function blocks, and the output of these function blocks was superposed to the accelerator pedal reference signal coming from the driver (see Fig. 1). The traction motor was controlled by two Visedo PowerMASTER frequency inverters. The PLC uses CANopen to communicate with the frequency converters at a 10 ms cycle time (the bitrate was set to 250 kbits/s). The PLC sends the estimated torque from both converters and the measured rotational speed of the motor as an array of signed 16-bit integer values through an Ethernet UDP connection to a laptop computer. The angular velocity ω_m was measured by using the resolver of the traction motor. The laptop PC is used only for recording the data packets sent by the PLC. The sample time has been selected so that it covers frequencies slightly above the resonance frequency in order to see if there are any additional dynamics that should be taken into consideration.

A. On-road Identification Experiments

The identification experiments were conducted during the series electric mode operation by considering different on-road measurements at a moderate speed of 20 km/h. An example of on-road identification experiments is illustrated in Fig. 5. In order to ensure repeatability and get adequate results from the identification experiments, the on-road tests were accomplished using the same operating speed, but the other operating conditions such as road, weather, and route conditions varied in the tests. Before the identification process, data preprocessing must be done in order to find suitable segments that exclude bad data, and the signals are detrended prior to the estimation. In these tests, the mechanical system was excited by a ten-cell shift register operating on a 10 ms time level and a chirp signal.

Typical guidelines given for the PRBS clock frequency suggest that it should be chosen to be about 2.5 times the bandwidth covered by the signal. Moreover, the limit of the effective frequency band covered by the PRBS is around $f_{bw} = 1/(3{\cdot}\Delta T_{PRBS})$. As discussed above, the drivability is mostly influenced by the low-frequency characteristics [4], and thus, an adequate model that describes these dynamics is of importance. In this paper, the frequency band covered by the excitation signals has been chosen to be in the frequency region from 0 Hz to 50 Hz in order to obtain a good description of the low-frequency dynamics. Hence, the PRBS considered here has a constant spectral density content from the low frequencies to the high frequencies based on the same sample time used for data acquisition. It is emphasized that this selection does not have an effect on the quality of the identification [31] as the influence of this selection is compensated for by considering an appropriate parameter estimation routine with the proposed weights (8).

The second important factor related to the PRBS design is the sequence length, $N_p = 2^n - 1$, which depends on the number of cells n. In general, the sequence length N_p should be chosen to be sufficiently long so that the pseudo random characteristics of the signal are obtained. On the other hand, if the sequence length is too long, it will result in longer time periods without signal alternations. In this paper, one of the limiting factors for the signal selection is the duration of the on-road experiments, and thus, a trade-off of $n = 10$ is considered, which gives a reasonable period for the signal to carry out the experiments with a spectral content rich in frequencies.

The chirp excitation signal was chosen such that it excites frequencies around the dominant resonant frequency, and thus, it was swept from 0.1 Hz to 30 Hz during 295 s. The amplitudes of the excitation signals were set as follows: the amplitude of the PRBS was set to 76.7 Nm and with the chirp to 63.9 Nm, respectively. In this paper, the amplitudes of the signals have been selected based on experimental tests by iteration starting from low values from the rated drive torque, but the amplitudes are limited so that the mechanical stress is not too high.

Fig. 6 shows the frequency responses obtained from the on-road identification experiments. It is pointed out that more emphasis has been put on the PRBS-based tests because of the practical limitations of the chirp signal during on-road experiments. Thus, in Fig. 6, the average frequency responses from multiple PRBS-based experiments are indicated by the dashed black line, and the gray shaded area represents the average variation. Based on the results, the dominant resonance frequency of the mechanical driveline can be identified from these tests, and more importantly, the assumption of dynamics related to the resonating two-mass system is justified.

To further validate these observations, the average frequency responses from the PRBS-based experiments are compared with the chirp-based ones in Fig. 6. Moreover, the reference model, in other words, the initial assumption of the system dynamics with the parameters given in Table I is shown. Again, the resonance of the mechanical system can be clearly observed in the identified amplitude and phase responses. Furthermore, a good correspondence is reached between the frequency responses obtained from the PRBS- and chirp-based identification experiments, indicating that the on-road experiments yield adequate information of the dynamics. The initial assumption of the system dynamics is close to the identified frequency responses, but evidently, the parameter

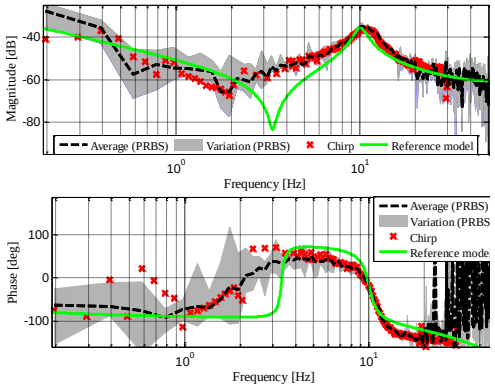

Fig 6. Identified frequency responses from the on-road identification experiments with the PRBS and chirp. The average of the PRBS-based identification results are indicated by the dashed black line, and the grey area represents the variation. The results are compared with the reference model (green), and the on-road identification experiments with the chirp excitation signal (red).

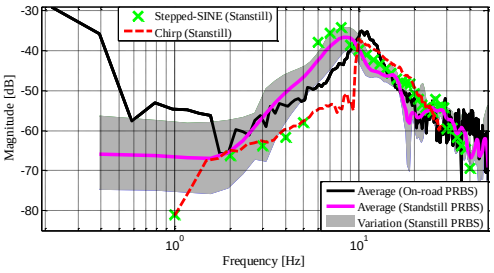

Fig. 7. Frequency response obtained from the different standstill identification experiments (PRBS, stepped sine and chirp) compared with the on-road experiment with the PRBS.

estimation step is required to have a better correspondence with the frequency-domain observations.

B. Standstill Identification experiments

Standstill identification experiments were conducted to validate the observations made on the results of the on-road identification experiments. In this paper, the term 'standstill identification experiments' refers to the operating mode in which the bus is held in place by the braking system and the mechanical system is excited by broadband excitation signals as described above. In these tests, the broadband excitation signals, viz. the PRBS and the chirp, were applied and compared with the stepped sine experiments. The amplitudes of the PRBS and chirp signals were as above and the amplitude of the stepped sine was set to 63.7 Nm. The stepped sine identification experiments consisted of a series of single sine measurements at desired frequencies with frequency ranges of 1–30 Hz with 1 Hz resolution, 30–40 Hz with 2 Hz resolution, and 40–45 Hz with 5 Hz resolution. Numerous periods of each sine were measured, and the tests were conducted so that transients did not cause erroneous results. The PRBS was kept the unchanged in the experiments, but the chirp signal was swept from 1 to 28 Hz in 295 s.

In Fig. 7, the results of the standstill identification experiments are shown and compared with the average frequency response obtained from the PRBS-based on-road experiments (see Fig. 6). It can be seen in Fig. 7 that even though the standstill tests were carried out differently from the on-road ones, similar system dynamics can be observed. Despite the fact that there are differences between the identified frequency responses, the dominant system dynamics, or more precisely, the resonance frequency region, is clearly observable in the standstill stepped sine and PRBS experiments. It is obvious that the standstill identification tests increase the error in the estimation, because the nonlinearities of the system, such as friction, have a greater effect on the frequency response estimate [23], and the total inertia cannot be estimated. In the absence of total inertia, the identified dynamics does not correspond to a two-mass system dynamics, and therefore, anti-resonance should also be nonexistent.

Fig. 7 also shows that the chirp does not yield a similar frequency response estimate close to the resonance frequency for instance in the range of 6–10 Hz. Thus, the signal excites the mechanics differently, even though the tests were similar in terms of torque offset and amplitude (stepped sine). Nevertheless, the standstill results are consistent with the on-road ones in the high-frequency region and especially in the region close to the resonance, which indicates that the estimated frequency responses from the on-road experiments can be assumed to be reasonable.

C. Parameter estimation

To further validate the on-road identification experiments, a two-mass system model was estimated from the frequency-domain data with a discrete-time OE model structure as well as with the LS-based frequency response fitting with a Levenberg and Marquardt (LM) algorithm (8). The OE model structure was taken as a benchmark approach based on its established position in the model estimation of resonating mechanical systems [21], [24], [25]. The main reason for considering the OE model is that it has been successfully applied in several identification studies that have focused on resonating systems. In these studies, the OE model has been chosen because of its advantages related to the model structure, which provides unbiased estimates under noisy conditions [21] and in open- [24] and closed-loop operation [27], [28]. On the other hand, the LM-based parameter estimation approach has been proposed for the commissioning of a resonating mechanical system in [16], [29], [30] because of its excellent numerical properties and convergence characteristics. Even though it has been shown in [21] that the LM method does not provide unbiased estimates in closed-loop conditions, the LM approach has been successfully applied as an identification tool for a control method [29], [30] as it yields good model fits in the frequency domain. Owing to their well-established features and

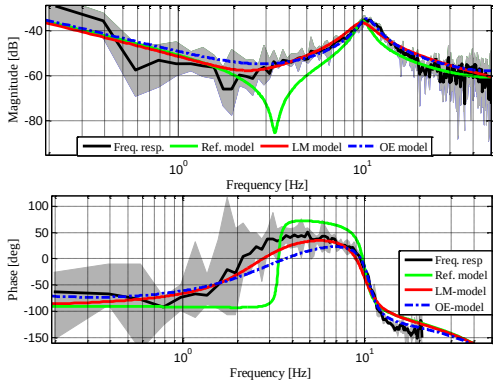

Fig. 8. Frequency responses obtained using the OE model structure in the estimation and the LM-based model fitting compared with the reference model and the experimental frequency response.

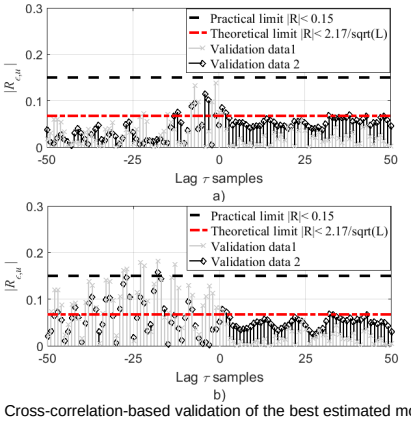

Fig. 9. Cross-correlation-based validation of the best estimated models against two independent validation data: a) output error model and b) LS model based on LM fit.

the application of LM and OE methods, these approaches are considered in this paper, but here the estimation is carried out for both methods in the frequency domain with a weighted error function (8). These changes deliver several advantages, such as an opportunity to focus the estimation on a selected set of frequencies, and furthermore, the proposed weights improve the model fit in the low-frequency region, which is the most critical region in an automotive application from the perspective of drivability.

A third-order model structure was chosen that corresponds to the two-mass system dynamics. In Fig. 8, the estimated parametric models with the OE and LM are shown with the average frequency response model obtained by the on-road identification experiments. The best fits were found iteratively by minimizing the error function (8), respectively. The reference model is also given in Fig. 8 to compare the estimation results with the initial assumption of the system dynamics.

Evidently, the estimated models show an acceptable agreement with the average frequency response estimate, and they capture the two-mass system dynamics. It is noteworthy that both of the estimated models yield almost similar fits, and they correspond to the frequency response estimate more accurately than the reference model.

D. Validation

To further analyze the results of the parameter estimation routines, physical parameters were also solved from the estimated models by using the approach [21] for the discrete OE model and [16] for the estimated LM model. Owing to the uncertainty related to the actual damping parameters, only the estimated motor inertia, vehicle mass, resonance, and spring constant were analyzed and are given in Table II. Further, the mean and standard deviations of the estimated physical parameters of the models obtained from six separate identification experiments are presented. As expected, the estimated parameters differ between the approaches, but on average, the values are reasonable.

In addition, the cross-validation routine studied for different resonating mechanical systems in [20], [21] was considered for model validation. The best model fit for both estimation approaches was searched iteratively, and then, a cross-correlation-based residual analysis was made (more details in [21]). The results are shown in Fig. 9. The validation is based on the calculation of the normalized cross-correlation $R_{\varepsilon,u}$ between the residual prediction error $\varepsilon = y(k)-\hat{y}(k)$ and the input signal $u(k)$. A confidence level of 97% expressed as $2.17/\sqrt{L}$ is shown by the red dashed line based on $L = 1023$ samples used in the estimation, and the practical confidence level of 0.15 is also indicated. An acceptable model should meet the condition $|R_{\varepsilon,u}| \le 2.17/\sqrt{L}$ or at least the practical level $|R_{\varepsilon,u}| \le 0.15$ proposed in [31]. Because the identification experiments have been carried out multiple times, some of the data sets are used as independent evaluation data in order to validate the estimated models. In Fig. 9, the models are validated against two independent validation data; data 1 are denoted by a grey line and a cross, and data 2 are indicated by a black line and a diamond.

According to the results in Fig. 9 a), the OE model provides a valid model against both validation data, thereby indicating satisfactory reliability of the identifications tests. This can be observed from the residuals that remain below the practical confidence limit in both validation data cases. On the other hand, the LS-based fit in Fig. 9 b) indicates that the frequency-domain-based LM algorithm does not yield a valid model in terms of cross-validation. A similar discrepancy between the LM- and OE-based parameter estimation approaches is reported in [21], where a simple experimental resonating mechanical system is used for validation. It is emphasized here that in mobile equipment the repeatability of identification experiments is not as straightforward as in typical industrial identification examples, and hence, a large number of tests at moderate speeds are needed to ensure valid models.

TABLE II
ESTIMATED PARAMETERS IN DIFFERENT ESTIMATION ROUTINES

Symbol	OE-models (mean ± std.)	LM-model (mean ± std.)
k_s (kN/m)	1479.9 ± 237.6	1280.8 ± 122.9
f_{res} (Hz)	12.02 ± 0.87	9.9 ± 0.21
f_{ares} (Hz)	3.45 ± 0.37	2.31 ± 0.21
J_m (kgm^2)	3.65 ± 0.11	4.29 ± 0.35
m (kg)	11600.9 ± 1827.8	13013.7 ± 141.9

Based on the results in Table II, it can be seen that the LM method gives more consistent physical parameter estimates between the experiments. This is an advantage of the LS-based fitting [16], [29] as the equation error minimum can be easily found as a constraint on the OE criterion, but the difference between the criteria results in different models. Further, the LM method can lead to biased estimates as reported in [21]; however, it is pointed out that it is often sufficient to find a model that accurately describes the system in a limited frequency band in order to obtain a low-order model for controller designs in which the LM method is typically applied [29]. Based on the results given in Table II, the approaches produce slightly different models, and the OE method yields unbiased estimates, as expected. However, it should be noted that the general evaluation of the goodness of the estimated parameters should be made on the intended application. Nevertheless, both approaches provide reasonable estimates of the driveline parameters, but the final evaluation of the estimated model should be made in an application-dependent manner, that is, by control or observer design.

Note also that the comparison of the estimated parameters with the reference parameters is quite difficult as the mechanical parameters of the driveline are only known with some degree of confidence. Similar issues have been reported in [16], [20], [21], where the experimental systems are laboratory examples of resonating mechanical systems, and thus, simpler in nature.

V. DISCUSSION

The main objective of this paper was to propose a similar identification (commissioning) routine for the identification of a resonating mechanical system in mobile road vehicles as is typically considered for mechanical systems used in the industry [16]. In general, the same approaches can be employed and valid models can be achieved, but a few remarks should be made. The operating conditions (weather and road conditions) have a significant influence on the identified dynamics. For instance, the identification results presented in this paper have been produced in different seasons; in winter and spring. Furthermore, the vehicle has been operated at a moderate speed on a nearly flat surface, but naturally, slopes would impact on the determination of the low-frequency dynamics. Thus, acceleration and deceleration tests should be conducted in advance in order to achieve fixed dynamics or suitable initial conditions for the chosen parameter estimation approach. A second remark should be made about the option to use a standstill identification test combined with an acceleration test to construct a simple two-mass system model based on total inertia, resonance frequency, and estimated motor inertia.

The third remark concerns the significance of the sufficient excitation signal. The PRBS is the most straightforward one, especially for on-road commissioning experiments as it can be designed and implemented relatively easily, and the flat amplitude spectrum offers desirable features for the identification of such a system to generate a reasonable estimate of the linear dynamics. Moreover, the nonlinear behavior, such as backlash, can be taken into account in the PRBS signal design.

An additional remark should be made about the suitable order for the model to be estimated in conjunction with the driveline dynamics. In this paper, the two-mass system model approximation is a justified choice of the model structure based on the initial inspection of the identified raw frequency responses and the statistical validation process. However, depending on the driveline configuration, the final model should be selected according to the prior knowledge, identified frequency responses, and parameter estimation supported by a statistical analysis. Thus, the two-mass model approximation considered here cannot be generalized to describe all drivelines in mobile equipment, because the system might include additional dynamics, such as resonances, as a result of different mechanical configurations or faults. Note, however, that the low-order model approximation, that is, the dominant dynamics, is usually sufficient for the controller design in automotive applications [7], [11].

A final remark should be made about the applicability of the identification routine to vehicles with different driveline configurations. In this paper, the identification tests were carried out exclusively in the series electric mode so that the traction motor produced the driving power. Naturally, the driveline of the hybrid bus can also be operated in other modes, and several driveline configurations have been reported in the literature [32], [32]. In general, the identification steps proposed in this paper can also be followed in the case of other configurations. The first step is the selection of a model structure to describe the dynamics by using parameters obtained from the geometrical and material properties and simple experimental tests. Naturally, the model complexity changes with the studied driveline configuration and mechanical properties, but still, a two-mass or three-mass-model should be the simplest option to describe the dynamics of a driveline. The second step is the selection of the proper characteristics for the excitation signal and design of the on-road identification tests. The final step is the parameter estimation routine with validation, but obviously, it may also be necessary to re-design the first two steps.

VI. CONCLUSION

Identification of resonating mechanical systems in electric drives using artificial excitation signals has been a topic of intense research over the last few decades. As electrically powered mobile road vehicles have become more and more widespread, a similar type of identification approaches could provide a viable solution for commissioning of such a drive.

The results of this paper show that, the well-known excitation-based system identification approaches can be adopted to identify the characteristics of the resonating mechanical load of an actual hybrid city bus.

Although the focus of this paper was on the identification of the mechanical driveline of a hybrid bus, the proposed approaches can be generalized to other mobile technologies, such as electric and hybrid vehicles and heavy working machines. Using the estimated parameter values build the mechanical system model provides more accuracy to the model-based diagnostics and control functions needed in various mobile technologies. The results are important considering the various needs of modern mobile equipment with advanced diagnostics, monitoring, or control options in which an adequate system model plays an essential role. The identification routines proposed in this paper could be adopted as an identification run in various automotive applications.

The discussion covered modeling of a resonating mechanical driveline in conjunction with parameter estimation built on frequency-domain observations. The estimated frequency responses obtained in the excitation-based on-road identification tests clearly indicate that the characteristics of a resonating system can be identified, and a reasonable two-mass system model approximation can be estimated based on these observations.

REFERENCES

[1] C. Wu, C. Zhu, J. Sun, and Y. Ge, "A synthesized diagnosis approach for lithium-ion battery in hybrid electric vehicle," *IEEE Trans. Veh. Technol*., vol. 66, DOI 10.1109/TVT.2016.2634125, no. 7, pp. 5595–5603, July 2017.

[2] M. Roche, W. Shabbir, and S. Evangelou, "Voltage Control for Enhanced Power Electronic Efficiency in Series Hybrid Electric Vehicles," *IEEE Trans. Veh. Technol*., vol. 66, DOI 10.1109/TVT.2016.2599153, no. 5, pp. 3645–3658, May 2017.

[3] J. Druant, H. Vandompel, F. De Belie, J. Melkebeek, and P. Sergeant, "Torque analysis on a double rotor electrical variable transmission with hybrid excitation," *IEEE Trans. Ind. Electron.*, vol. 64, DOI 10.1109/TIE.2016.2608768, no. 6, pp. 60–68, Jan 2017.

[4] N. Amann, J. Böcker, and F. Prenner, "Active damping of drive train oscillations for an electrically driven vehicle," *IEEE/ASME Trans. Mechatronics.*, vol. 9, DOI 10.1109/TMECH.2004.839036, no. 4, pp. 697–700, Dec. 2004.

[5] M. Berriri, P. Chevrel, and D. Lefebvre, "Vehicle driveability improvement by prediction and compensation of the shaft torque: a state-space approach," in *Proc. of* 2007 *European Contr. Conf. (ECC)*, Kos, Greece, 2007, pp. 78–84.

[6] A. Abass, S. Zhao, and A. T. Shenton, "Nonparametric driveline identification and control," in *Int. Conf. on Intell. Syst., Modell. and Sim*. (ISMS), Feb. 2010, pp. 238–243

[7] J. Böcker, N. Amann, and B. Schulz, "Active suppression of torsional oscillations," in *Proc. 3rd IFAC Symp. on Mechatronic Syst.,* Sydney, Australia, Sep. 2004, pp. 325–330

[8] P. Templin, "Simultaneous estimation of driveline dynamics and backlash size for control design," in *Proc. 17th Int. Conf. on Contr. Appl.*, San Antonio, Texas, USA, Sep. 2008, pp. 13–18

[9] F. Sun and Y. Cui, "Influence of parameter variations on system identification of full car model," in *Proc. of the Int. Multi-Conf. of Engineers and Comp. Scientists (IMECS)*, March 2011, pp. 839–843

[10] J. Fredriksson, H. Weiefors, and B. Egardt, "Powertrain control for active damping of driveline oscillations," *Veh. Syst. Dyn.*, vol. 37, no. 5, pp. 359–376, 2002

[11] P. Langthaler and L. del Re, "Identification of driveline parameters using an augmented nonlinear model," 16th *IFAC World Congress*, Prague, Czech Republic, vol. 38, no. 1, pp. 31–36, 2005

[12] M. Grotjahn, L. Quernheim, and S. Zemke, "Modelling and identification of car driveline dynamics for anti-jerk controller design," *IEEE Int. Conf. on Mechatronics*, July 2006, pp.131–136.

[13] M. Fleischer, "Reduced model identification for traction drive-trains," in *Proc. of 40th IAS Annual Meeting*, vol. 4, no. 2, pp. 2873–2879, Oct. 2005.

[14] P. Templin and B. Egardt, "An LQR torque compensator for driveline oscillation damping," *IEEE Int. Conf. on Contr. Appl*., Saint Petersburg, Russia, July 2009, pp. 352–356.

[15] F. U. Syed, M. L. Kuang, and H. Ying, "Active damping wheel-torque control system to reduce driveline oscillations in a power-split hybrid electric vehicle," *IEEE Trans. on Vehicular Technology*, vol. 58, no. 9, pp. 4769–4785, Nov. 2009.

[16] S. Villwock and M. Pacas, "Application of the Welch-Method for the identification of two- and three-mass-systems," *IEEE Trans. Ind. Electron.*, vol. 55, no. 1, pp. 457–466, Jan. 2008.

[17] I. Müller and P. Mutschler, "Two reliable methods for estimating the mechanical parameters of a rotating three-inertia-system," in *Proc. EPE-PEMC Conf.*, Dubrovnik, Croatia, 2002, pp. 1–5.

[18] P. Lindh, G. M Tehrani, T. Lindh, J-H Montonen, J. Pyrhönen, J. T. Sopanen, M. Niemelä, Y. Alexandrova, P. Immonen, L. Aarniovuori, and M. Polikarpova, "Multidisciplinary design of a permanent-magnet traction motor for a hybrid bus taking the load cycle into account," *IEEE Trans. Ind. Electron.*, vol. 63, no. 6, pp. 3397–3408, June 2016.

[19] A. J. Tuononen and A. Lajunen, "Modal analysis of different drivetrain configurations in electric vehicles," *J. Vib. Control.*, DOI 10.1177/1077546316635857, pp. 1–11, 2016.

[20] N. Nevaranta, S. Derammelaere, J. Parkkinen, B. Vervisch, T. Lindh, M. Niemelä, and O. Pyrhönen, "Online identification of a two-mass system in the frequency domain using a Kalman filter," *Model., Identif. and Contr.*, vol. 37, DOI 10.4173/mic.2016.2.5, no. 2, pp. 133–147, 2016.

[21] S. E. Saarakkala and M. Hinkkanen, "Identification of two-mass mechanical systems using torque excitation: Design and experimental evaluation", *IEEE Trans. Ind. Appl*., vol. 51, DOI 10.1109/TIA.2015.2416128, no. 5, pp. 4180–4189, March 2015.

[22] D. Luczak and K. Zawirski, "Parametric identification of multi-mass mechanical systems in electrical drives using nonlinear least squares method," in *Proc. of IECON* 2015, Yokohama, Japan, pp. 4046–4051, Nov. 2015.

[23] N. Nevaranta, S. Derammelaere, J. Parkkinen, B. Vervisch, T. Lindh, K. Stockman, M. Niemelä, O. Pyrhönen, and J. Pyrhönen, "Online identification of a mechanical system in frequency domain using Sliding DFT," *IEEE Trans. Ind. Electron.*, vol. 63, no. 9, pp. 5712–5723, 2016.

[24] M. Östring, S. Gunnarsson, and M. Norrlöf, "Closed-loop identification of an industrial robot containing flexibilities," *Control Eng. Pract*., vol. 1, no. 11, pp. 291–300, 2003.

[25] D. Luczak and K. Nowopolski, "Identification of multi-mass mechanical systems in electrical drives," in *Proc. of 16th Int. Conf. on Mechatronics*, Brno, Czech Republic, Dec. 2014, pp. 1–8.

[26] H. Zoubek and M. Pacas, "Encoderless identification of two-mass-systems utilizing an extended speed adaptive observer structure," *IEEE Trans. Ind. Electron.*, vol. 64, no. 1, pp. 595–604, Jan 2017.

[27] N. Nevaranta, J. Parkkinen, T. Lindh, M. Niemelä, O. Pyrhönen and J. Pyrhönen, "Online estimation of linear tooth-belt drive system parameters," *IEEE Trans. Ind. Electron*., vol. 62, no. 11, pp. 7214–7223, Nov. 2015

[28] I.D. Landau and A. Karimi, "An output error recursive algorithm for unbiased identification in closed loop", *Automatica*, vol. 33, no. 5, pp. 933–938, 1997

[29] M. Pacas, S. Villwock, P. Szczupak and H. Zoubek, "Methods for commissioning and identification in drives," *Int. Jour. for Comp.and Math. in Electr. and Electronic Eng.*, vol. 29, no. 1, pp. 53–71, Oct. 2010

[30] D. Łuczak, and K. Zawirski, "Parametric identification of multi-mass mechanical systems in electrical drives using nonlinear least squares method," in *Proc. of IECON*, Yokohama, Japan, Nov. 2015, pp. 4046–4051.

[31] I. D. Landau and G. Zito, Digital Control Systems: Design, Identification and Implementation, 1st ed. Berlin, Germany: Springer-Verlag, 2006.

[32] J. Liu and H. Peng, "Modeling and control of a power-split hybrid vehicle," *IEEE Trans. on Contr. Syst. Tech.*, vol. 16, no. 6, pp. 1242−1251, Nov. 2008.

[33] L. Li, X. Wang and J. Song, "Fuel consumption optimization for smart hybrid electric vehicle during a car-following process," *Mech. Syst. and Sign. Proc.*, vol. 87, no. 1, pp. 17-29, Oct. 2015.

Jan-Henri Montonen received the M.Sc. degree in electrical engineering from the Lappeenranta University of Technology (LUT), Lappeenranta, Finland in 2012.

His research interests include virtual simulation and intelligent control of electrically driven mechatronic systems. He is also engaged in teaching and research of control engineering and digital systems at LUT.

Niko Nevaranta (M'17) received the B.Sc., M.Sc. and D.Sc degrees in electrical engineering from the Lappeenranta University of Technology (LUT), Lappeenranta, Finland in 2010, 2011 and 2016, respectively, where he is currently working as a Post-Doctoral Researcher.

His research interest includes modeling and control of electrical drives, motion control, system identification, parameter estimation, system monitoring, and diagnostics. Currently he is also researching control approach for active magnetic bearings and rotor dynamics identification.

Tuomo Lindh was born in Lappeenranta, Finland, in 1964. He obtained B.Sc. degree from Mikkeli Institute of Technology in 1989. After couple of years work in industry he obtained his M.Sc. in Technology in 1997 and D.Sc. in Technology in 2003 from the Lappeenranta University of Technology (LUT). He currently works as an Associate Professor at LUT. His research interests include generator and motor drives and system engineering especially in the areas of distributed power generation, electric vehicles and in mechatronics.

Jani Alho was born in Lappeenranta, Finland, in 1978. He received the M.Sc. degree in electrical engineering from the Lappeenranta University of Technology (LUT), Lappeenranta, Finland, in 2016. He is currently working toward the Doctoral degree in electrical engineering at the School of Energy System, LUT. He also works as a Software Engineer with Danfoss Power Solutions, Lappeenranta. His current research interests include electrical safety and intelligent control of electrically drive marine vessels and land vehicles.

Paula Immonen was born in Imatra, Finland, in 1986. She received the M.Sc. and D.Sc. degrees in electrical engineering from Lappeenranta University of Technology (LUT), Lappeenranta, Finland, in 2008 and 2013, respectively. She is currently with the Department of Electrical Engineering, LUT. Her current research focuses on the diesel–electric hybrid drive system.

Olli Pyrhönen received the M.Sc. and D.Sc. degrees in electrical engineering from the Lappeenranta University of Technology (LUT), Lappeenranta, Finland, in 1990 and 1998, respectively. Since 2000, he has been a Professor in applied control engineering at LUT. In 2010, he received further teaching and research responsibility in the wind power technology at LUT. He has gained industrial experience as a R&D Engineer at ABB Helsinki in 1990-1993 and as a CTO of The Switch in 2007-2010. His current research areas include modeling and control of active magnetic bearings, bearing-less machines, renewable power electronics and electrical drive systems.

Publication II

Montonen, J.-H., Nevaranta, N., Niemelä, M., and Lindh, T.
Comparison of Extrainsensitive Input Shaping and Swing-Angle-Estimation-Based Slew Control Approaches for a Tower Crane

Reprinted with permission from
Applied Sciences
Vol. 12, 2022

applied sciences

MDPI

Article

Comparison of Extrainsensitive Input Shaping and Swing-Angle-Estimation-Based Slew Control Approaches for a Tower Crane

Jan-Henri Montonen *, Niko Nevaranta, Markku Niemelä and Tuomo Lindh

School of Energy Systems, Lappeenranta-Lahti University of Technology (LUT), Skinnarilankatu 34, 53850 Lappeenranta, Finland; niko.nevaranta@lut.fi (N.N.); markku.niemela@lut.fi (M.N.); tuomo.lindh@lut.fi (T.L.)

* Correspondence: henri.montonen@lut.fi

Abstract: Tower cranes are needed to move heavy objects safely around construction sites. In tower cranes, payload oscillations are a typical problem that can cause safety issues, especially if the crane is not operated by an experienced user. Depending on the system, there are different causes for oscillations, e.g., inertial forces from the crane movement or external forces, such as weather conditions. Hence, the selected control law for input tracking plays an important role to limit the oscillatory motion and to help the crane operator to prevent unwanted operations. In this paper, we study the slew control of a tower crane application from the viewpoint of reducing payload oscillations. Two different approaches are studied: open-loop control based on extrainsensitive input shaping and closed-loop swing angle control, based on the estimation of the hoist cable angle. The proposed control approaches are validated by running the developed control program against a multibody mechanics simulator containing a model of a Liebherr tower crane. The studied control laws are also evaluated using an experimental setup, which consists of a two-axis manipulator, inverters, and a programmable logic controller in which the studied control methods are implemented. The results from the multibody dynamics simulations and from the experimental setup are presented and evaluated from the viewpoint of crane operation.

Keywords: input shaping; payload oscillations; swing angle estimation; slew control; tower crane

Citation: Montonen, J.-H.; Nevaranta, N.; Niemelä, M.; Lind, T. Comparison of Extrainsensitive Input Shaping and Swing-Angle- Estimation-Based Slew Control Approaches for a Tower Crane. *Appl. Sci.* **2022**, *12*, 5945. https://doi.org/10.3390/app12125945

Academic Editor: José Sánchez Moreno

Received: 3 May 2022
Accepted: 8 June 2022
Published: 10 June 2022

1. Introduction

Tower cranes are widely used for lifting operations in different construction and industrial sites. During the operation of these cranes, the possible oscillatory behavior caused by the moving payload may have an adverse effect both on the accuracy of payload positioning and on safety. The control of these oscillations is a challenging task because of the nonlinear nature of the rotating system dynamics, and on the other hand, in most cases, there are not enough sensors to be used for compensation. This problem has been a topic of intense research in recent years and has resulted in several papers focusing on the modeling and control of various gantry and tower crane applications.

In the literature, various control approaches have been proposed to reduce the payload oscillations of different tower crane applications. The approaches can be roughly categorized into open- and closed-loop ones. The most straightforward methods are based on filtering of the natural frequencies from the trolley motion by using notch or low-pass filters [1]. The well-known input shaping can also be included in the same category as a method to modify the signal commands in order to minimize vibration [2]. Input shaping can be carried out in various ways, e.g., by creating multi-input-shaped commands [3], radial-motion-assisted shapers [4], or a zero-vibration shaper [5], to name but a few. The methods based on input shaping can be regarded as open-loop control methods, because the motion references are manipulated prior to being fed to controllers, and their main

advantage is that they do not require any measurement sensor for the payload angles. Different kinds of methods have also been proposed for input reference shaping, as in [6], where the authors use a model predictive controller to calculate optimal references for the inner loop PID control. The other category of approaches to reduce payload oscillations is closed-loop ones that are based on advanced control topologies, estimations, or additional feedback measurements. In [7], a neural-network-based control law is applied to a tower crane. Another approach is proposed in [8], where an elastic jib model for a large tower crane is derived and a state feedback law is proposed. In [9], a real-time optimal velocity control that is capable of limiting oscillations is presented. An inverse dynamics-based approach is introduced in [10] and compared with the traditional input shaper method. An observer-based nonlinear feedback controller for four-degree-of-freedom offshore ship-mounted tower cranes is proposed in [11]. A ship-mounted tower crane suffers from disturbances caused by sea waves or currents, which makes the controller design for such a system extra challenging. In [12], an adaptive sliding mode control is proposed for the antiswing control of a tower crane because of its robustness against system uncertainties and external disturbances. Further, in [13], an adaptive fuzzy control is proposed for the control of overhead cranes. The robustness of the method is tested with nonlinear disturbances. Due to the nature of disturbances (changing payloads, wind forces, collisions) in crane applications, it can be hard to measure the effect of disturbances on the crane system without extensive instrumentation. Adding extra instrumentation, on the other hand, is undesirable in the harsh environment in which the cranes operate. The control system must be designed robust enough to withstand these disturbances. Simulation of the effect of wind forces to a load carried by a mobile crane is presented in [14]. Although safety is not the primary aspect of this work, safety plays an important role in crane operations. Control system safety aspects of heavy industrial cranes are addressed and discussed in [15].

A crane should be able to transfer its payload quickly to the target position while suppressing the payload sway. The problem of load transfer is addressed in [16], where a control approach is proposed that is robust to variable rope length. Another approach, called saturating control, presented in [17], is used for suppressing the payload sway. In [18], a feedback control, based on inverse dynamics, is proposed to make the load follow a reference trajectory. Similar approach is often used in the control of industrial robot applications. In [19] an approach based on controlling the load position of an overhead crane instead of the trolley position, is presented for avoiding collisions of load with obstacles and to reduce load transfer time and residual vibration.

An antiswing control for crane application, based on swing angle feedback, is presented in [20]. Equations of motion for the load swing of a tower crane are presented in [21]. In this paper, the swing angle feedback control of [20] is combined with a swing angle estimator built from the equations presented in [21] to generate estimator-based swing angle feedback control. In this paper, we compare traditional input shaping and the estimator-based swing angle feedback control for reduction of payload oscillations of a tower crane. The comparison is conducted by using a virtual simulation tool and a small-scale experimental setup. Simulations are carried out using a multibody dynamics simulator environment with a model of a Liebherr 112EC-B8 tower crane. Both control approaches are also tested using a small-scale experimental laboratory setup, which has a belt-driven axis and a pendulum with angle measurement. This setup emulates one axis (trolley) of the tower crane movement. Although tower crane is used when comparing these methods, these methods can be adopted to other types of cranes, for example, gantry cranes and overhead cranes.

2. Slew Control Approaches

The tower crane has three degrees of freedom associated with the movement of the payload. The rotational motion of the movable jib is referred to as slew, the horizontal motion along with the jib as trolley, and the vertical movement of the payload as hoist as depicted in Figure 1a. The swing angle is the angle between the hoist cable and a

straight vertical line down from the trolley. The swing angle can be divided into radial and tangential components. Naturally, when the crane is operated, the movement of the payload may cause oscillatory behavior. Because this behavior is nonlinear in nature, the control of the unwanted oscillations is a difficult problem to solve. In most cases, there is not enough information, i.e., measurements from the system, in order to obtain a feedback-based control law. Thus, the derived control laws must be designed so that they reduce oscillations, e.g., by input reference shaping or by using estimator-based control strategies. In this paper, the slew motion of a tower crane application (see Figure 1a is analyzed from the viewpoint of reducing payload vibration by considering two different control approaches: (i) an open-loop robust extrainsensitive (EI) shaper and (ii) a slew-angle-estimation-based closed-loop method.

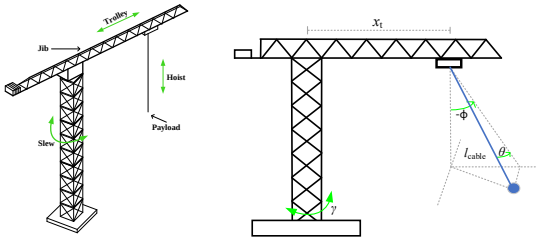

(**a**) (**b**)

Figure 1. (**a**) Tower crane with three degrees of freedom: rotational movement (slew), horizontal movement (trolley), and vertical movement (hoist). (**b**) Simplified free body diagram of the dynamics.

2.1. Extrainsensitive Input Shaper

Input shaping is an open-loop approach for the slew control, and it consists of convolving of the input signal with well-chosen impulses. The basic idea is to compensate the oscillatory motion by shifted pulses

$$F(s) = A_0 + \sum_{i=1}^{n} A_i e^{-sT_i}, \tag{1}$$

where $A_0 ... A_n$ and $T_1 ... T_n$ are the amplitudes and time delays of the pulses. The basic principle of the input shaping approach is depicted in Figure 2b, where the velocity inner loop control $C(s)$ is a PID-based control. A block diagram of an input shaper is presented in Figure 2a. The input shaper consists of gains and delays. Different shapers can be obtained by changing the number of impulses and their amplitudes and delays. It is worth remarking that this method causes a lag to the operator's commands and makes operating of the crane somewhat more difficult.

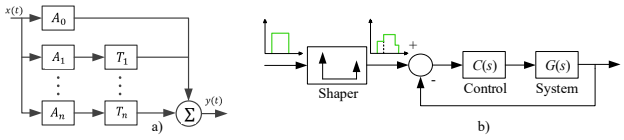

Figure 2. (**a**) Input shaper design using gains and delays and (**b**) input shaper used with the control.

In a tower crane system, the input shaping approach can reduce oscillations caused by inertial forces by modifying the reference signal. As real applications are often complicated to model accurately, the selected shaping approach should be designed so that it is robust to modeling errors and uncertainties. Different shaper designs have been presented in [22];

in the present paper, the extrainsensitive shaper (EI shaper) has been selected because of its insensitivity to modeling errors. Impulse amplitudes A and their delays t can be calculated as follows

$$EI = \begin{bmatrix} A_i \\ t_i \end{bmatrix} = \begin{bmatrix} \frac{1+V_{tol}}{4} & \frac{1-V_{tol}}{2} & \frac{1+V_{tol}}{4} \\ 0 & \frac{\tau}{2} & \tau \end{bmatrix}, \quad (2)$$

where V_{tol} is the maximum allowed residual vibration (e.g., 5% $\rightarrow$ V_{tol} = 0.05), and τ is the period of undamped vibration. Residual vibration is the ratio of the vibration amplitude with input shaping to that without input shaping [22]. The period of undamped vibration can be calculated using

$$\tau = 2\pi\sqrt{\frac{l_{cable}}{g}} \quad (3)$$

where l_{cable} is the length of the hoist cable, and g is the gravitational acceleration. It is worth noticing that when the length of the hoist cable changes, its oscillation period changes. Therefore, delays of the shaper impulses must be changed accordingly. Depending on the shape of the load, the effective length of the hoist cable varies, and thereby the estimated or measured hoist cable length may differ. Thus, the robustness is provided by the selected EI-based input shaper structure.

2.2. Swing-Angle-Estimation-Based Closed-Loop Control

A swing angle feedback control is also studied in this paper. The method is based on the estimation of the hoist cable swing angle that is fed back to modify the speed reference to the speed controller. The slew and the trolley axis have their own independent speed control loops with a swing angle estimator. The estimator uses the radial and tangential acceleration of the trolley to calculate the estimated swing angle. Equations for the tangential and radial swing angles are derived in [21], and they are linearized for small swing angles by replacing $\sin(\theta)$ with θ. The estimated radial swing angle $\hat{\phi}$ (caused by the trolley movement, see Figure 1b) can be calculated from

$$\hat{\phi} = \frac{a_t - g\phi}{l_{cable}}, \quad (4)$$

where a_t denotes acceleration of the trolley, g is the gravitational force constant, and l_{cable} is the length of the hoist cable. The estimated tangential swing angle $\hat{\theta}$ (caused by the slew motion, see Figure 1b) can be calculated from

$$\hat{\theta} = \frac{x_t\dot{\omega_b} - g\theta}{l_{cable}}, \quad (5)$$

where x_t denotes the trolley position (distance from the pivot point), $\dot{\omega_b}$ is the rotational acceleration of the boom, and θ is the tangential swing angle of the hoist cable. It should be noted from (5) that the position of the trolley is required for the estimation of the tangential swing angle. The closed-loop approach is depicted in Figure 3, where the estimated value is used as a feedback for the PID velocity control. The PID controller controls the velocity of the associated axis according to the reference. The controller itself is a standard parallel-form PID controller. In the studied approach, the closed-loop controllers for the slew and the trolley movement use the estimated values as feedbacks, and they are working independent from each other. The estimated value is scaled by a gain K to obtain a suitable control effort. The gain can be different for each axis (K_ϕ for the radial and K_θ for the tangential axis). A rough guide for selecting an initial value for the parameter K is that it should produce approx. 50% of the maximum speed reference of the speed control when the swing angle is at its expected maximum. For example, if the maximum expected swing angle is 5 degrees, and the speed reference to the motor is between $-1...1$, a good initial

value for the tuning parameter K would be 0.1 ($0.1 \times 5 = 0.5$). The control error for the trolley movement e_t can then be expressed as

$$e_t = \omega_{ref,t} - \omega_t - K_\Phi \cdot \hat{\phi}, \quad (6)$$

where $\omega_{ref,t}$ is the speed reference to the trolley motor, ω_t is the actual speed of the trolley motor, $\hat{\phi}$ is the estimated radial component of the swing angle, and K_ϕ is the tuning parameter on how much the swing angle affects the speed control error of the trolley motor. The equation is similar in the case of slew motion (tangential), but the variables are only replaced by the variables for slew motion.

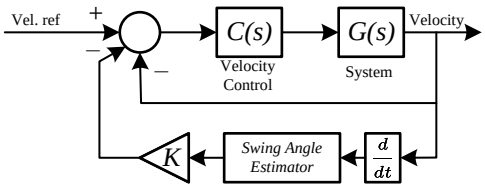

Figure 3. Proposed closed-loop method with a swing angle estimator. Acceleration of the trolley is the input to the estimator. It outputs the estimated angle, which is then multiplied by a tuning parameter K.

The hoist cable length is required for the estimation of the swing angles. However, it can be estimated by using information on the velocity of the hoist motor and mechanics of the hoist system. The initial position can be identified by performing an identification run at the system power-up, e.g., by raising or lowering the hook to its highest or lowest position and resetting the position to that.

3. Simulation Results

The tower crane control algorithms are simulated using a multibody dynamics simulator built by Mevea Ltd. (shown in Figure 4a. A Liebherr 112EC-B8 tower crane and a training area are modeled in the simulator, as the model and the simulator are also used for operator training (see Figure 4b). The multibody dynamics simulator communicates via an Ethernet connection with a relaying program. This relaying program connects to the Crane Control software, which is used for the implementation of the control algorithms and the user interface for changing control parameters. From the relaying program, it is possible to route signals to a programmable logic controller (PLC) and connect the actual hardware to the simulation loop. For example, one of the virtual motor drives of the crane can be substituted with a real one, i.e., modified to a hardware-in-loop (HIL) simulation [23]. However, the tests carried out in this paper are conducted without HIL simulation, and thus only the software components are used to model the crane. The simulation environment used in this study is presented in detail in [24].

The studied slew control approaches, namely the EI-shaper-based open-loop control and the swing-angle-estimator-based closed-loop control, are simulated and evaluated by considering similar operating conditions. The length of the cable is set to a constant value l_{cable} = 19.2 m to represent low-frequency oscillations, and the trolley position is kept constant. A barrel (mass 100 kg) is used as a load. The performance of the approaches is evaluated by means of residual vibrations at the end position of the motion profile.

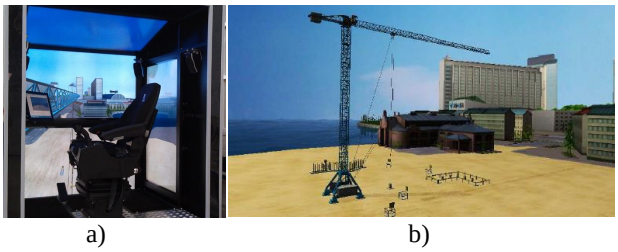

Figure 4. (**a**) Cabin of the multibody dynamics simulator and (**b**) model of a Liebherr 112EC-B8 tower crane.

3.1. Shaper-Based Control

In Figure 5, the results of the input shaper are shown when the delays and amplitudes of the three impulses of the shaper have been tuned using the selected cable length and a residual vibration tolerance value of 5%, V_{tol} = 0.05. Figure 5a illustrates the situation without the shaper when the crane operator rotates the boom at the maximum velocity for about 15 s. Obviously, the load oscillatory movement is observable as the load swings heavily during the movement, and after the motion profile, a residual oscillation with an amplitude of 3.7 degrees is seen. In contrast, in Figure 5b, the EI shaper is applied, which significantly reduces oscillations in the system, as can be seen in the reduced residual vibrations. With the input shaper, the residual vibration is reduced to approximately 11% of the residual vibration without shaping.

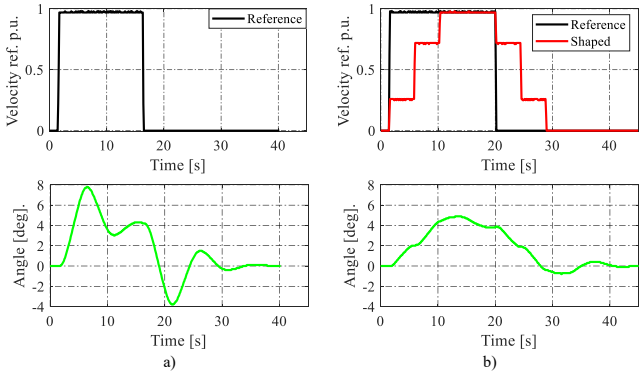

Figure 5. (**a**) Full slew movement without the input shaper and (**b**) results obtained with the EI input shaper method.

To further analyze the robustness properties of the EI-shaper-based approach, the actual cable length l_{cable} is varied and the shaper is designed using different design values l_{design}. The hoist cable length is considered the main source of uncertainty because its length varies greatly. Furthermore, the shape and size of the payload change the effective length of the hoist cable. In Figure 6, the results of four different tests are shown, where (a) the cable length is l_{cable} = 5 m and the shaper is designed using cable length value l_{design} = 10 m; (b) l_{cable} = 5 and l_{design} = 15 m; (c) l_{cable} = 15 and l_{design} = 10 m; and (d) l_{cable} = 15 m and l_{design} = 20 m. Based on the results with various operating and design conditions, the residual vibration is low compared with the design without the shaper in Figure 5a. Thus, it is shown that the EI shaper provides good robustness properties.

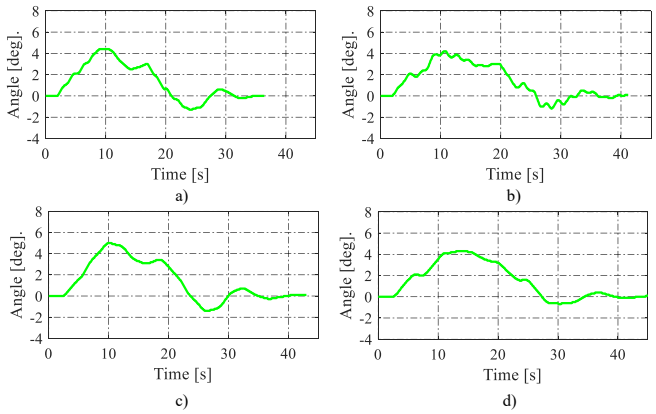

Figure 6. Analysis of the shaper design robustness against different actual cable lengths (l_{cable}): (**a**) l_{cable} = 5 m and l_{design} = 10 m; (**b**) l_{cable} = 5 m and l_{design} = 15 m; (**c**) l_{cable} = 15 m and l_{design} = 10 m; and (**d**) l_{cable} = 15 m and l_{design} = 20 m.

3.2. Swing-Angle-Estimation-Based Closed-Loop Control

The proposed closed-loop control based on the swing angle estimation is studied using the multibody dynamics simulator. In Figure 7, the results are shown (a) when the crane is operated only with the velocity control loop and (b) when the swing angle control is added to the system. A full-speed slew movement is used as a reference signal. The estimated swing angle is used as a feedback signal in the multibody dynamics simulator tests. The swing angle gain value (the tuning parameter K in Figure 3) is 5 for both the slew and the trolley movement ($K_\phi = K_\theta = 5$). The swing angle from measurement and estimation is in radians (degrees are used in figures), and the speed references to the slew and the trolley axis are in p.u. −1...1. The speed of the slew and the trolley motor is controlled by a PI controller. Swing angle estimation uses the actual hoist cable length.

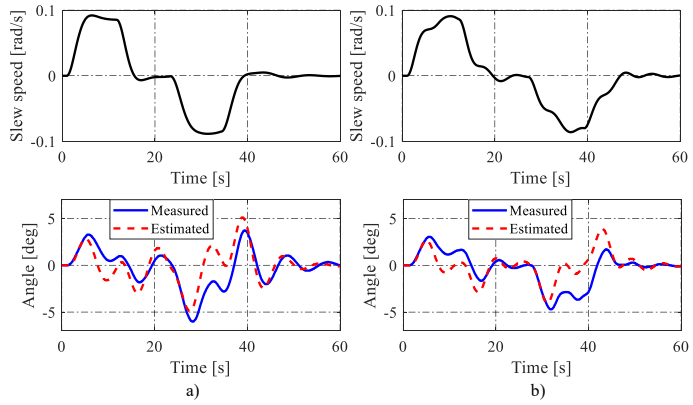

Figure 7. Comparison of control performance (**a**) without swing angle control and (**b**) with swing angle control.

According to Figure 7, the swing angle is overestimated compared with the measured swing angle. However, the control is capable of reducing the load swing without exact

swing angle information. The difference in amplitudes between the measured and the estimated swing angle can be compensated by using the swing angle gain value of the control. As long as the estimated swing angle has a correct sign during the acceleration and deceleration phases of the axis movement, the control is capable of reducing the load swing during these phases by slowing down or speeding up the axis and allowing the load to "catch up". In Figure 7a, the different signs of the measured and the estimated swing angles at time t = 10 s and at t = 32 s are explained by air friction. As the cable and the load are moving through the air, it causes a small angle to the hoist cable in the simulator. The estimator does not take this into account, and it assumes that the load is swinging forward (in the direction of motion) when the acceleration ends and a constant speed is reached. Despite this, the residual vibration at the end of the motion is significantly reduced when using the feedback control.

4. Experimental Results

A two-axis manipulator setup is used as an experimental setup for verification of the tower crane control algorithms. The experimental system is depicted in Figure 8. The manipulator setup consists of two belt-driven axes, two ABB ACSM1 frequency converters, and an ABB AC500 PLC connected to the frequency converters via an EtherCAT fieldbus. A stiff rod is acting as the load of the crane. The rod is connected to a rotary encoder for swing angle measurement. It is worth remarking that there is only one axis of the manipulator in the experimental evaluation, because the rotary encoder allows to measure axis movement only in one direction. Therefore, the manipulator setup used here only emulates the trolley movement of the tower crane.

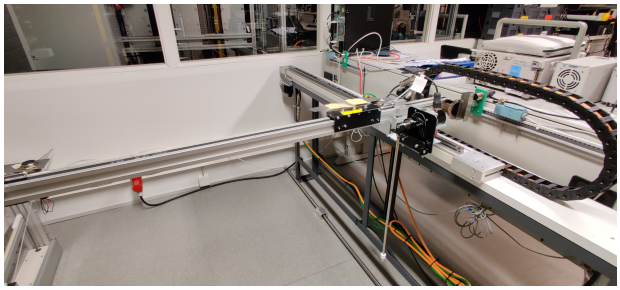

Figure 8. Experimental test setup emulating the trolley movement of the tower crane.

Both control methods are tested by implementing control algorithms to the PLC using the IEC61131-3 Structured Text language. A separate function generates a step up–step down speed reference to the axis in order to obtain comparable results. The function sets the speed reference to 10% of the nominal speed of the motor, which translates into approx. 0.79 m/s for 2 s and then zeros it. For data acquisition, the PLC sends reference values, actual values, and measured and estimated swing angles to a data logging computer. Figure 9 illustrates a test result when no control functions to suppress the oscillations are applied. Figure 9 also shows the estimated swing angle calculated using (4) by feeding the trolley movement to the equation.

As can be seen from Figure 9, the system oscillates heavily without supporting control functions. Next, an EI shaper is tuned to the system based on (2) and (3). With the maximum allowed residual vibration $V_{tol} = 0.05$ and by testing, we get an oscillation period $\tau = 1.56$ s for the pendulum. The vibration period is determined experimentally because the mass of the rod affects the center of gravity of the rod and weight system, and the equation for the vibration period of a mathematical pendulum as a function of pendulum length cannot be employed by using the total length of the rod and the load as the pendulum length. We

get impulse amplitudes A_i = [0.2625 0.475 0.2625] and delays T_i = [0 0.78 1.56] s for the EI shaper. The experimental test result using the EI shaper is presented in Figure 10.

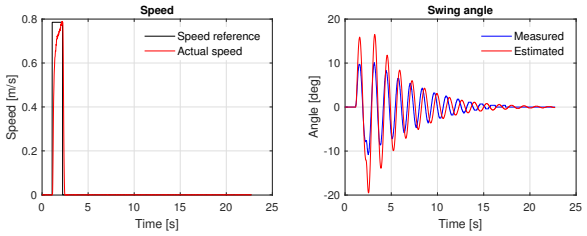

Figure 9. Speed reference and the actual speed (**left**) and the measured and estimated swing angles (**right**) when no control is applied.

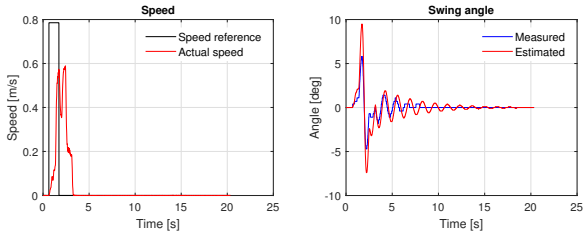

Figure 10. Speed reference and the actual speed and the measured and estimated swing angles when the EI shaper is applied.

As the results indicate, using a shaper to modify the input to the system significantly reduces load oscillations. The residual vibration (oscillation amplitude after the movement has ended) is approximately 10 degrees in the uncontrolled case, whereas the residual vibration is approximately 2 degrees when using an input shaper. The adverse effect of input shaping is visible in the shaped input signal as the trolley continues to move approximately 2 s after the reference signal has reached zero.

Next, the feedback-based control law is evaluated both by using direct measurement and estimation of the angle. Figure 11 presents a test result using the swing angle control law when the measured angle from the rotary encoder is used as a feedback. A swing angle gain value of 150 is used for the test, and it is kept the same in all tests. Using the feedback control reduces the delay in the operator commands compared with the input shaper. In this case, when using the actual measured angle from the sensor, the residual vibration is approximately the same as when using the input shaper shown in Figure 10. Next, the test result with the swing-angle-estimation-based feedback control is illustrated in Figure 12.

As can be noticed from the previous figures, the estimator overestimates the swing angle, which causes the system to react more strongly to the swing angle. This causes a slower movement and some correction action after the reference has reached zero but also small residual vibration. The value of the angle gain K_Φ was 150 during these tests; it is a tuning parameter that can be used to tune how much the control modifies the speed reference signal. It could even be a parameter that can be adjusted by the operator, as long as it has limits to prevent instability. The value of 150 used in the tests was selected experimentally.

As the load of the crane changes, the effective hoist cable length changes depending on the shape of the load. This causes an error between the actual and the assumed hoist cable length, which then affects the estimated swing angle. In Figure 13, robustness of the swing angle feedback control is tested by keeping the actual length of the rod and the load

system constant, but the l_{design} used in the estimator is varied. Results of the figure show that varying the hoist cable length (l_{cable}) between 80% and 120% of the actual length causes a residual vibration amplitude of 1 degree at worst.

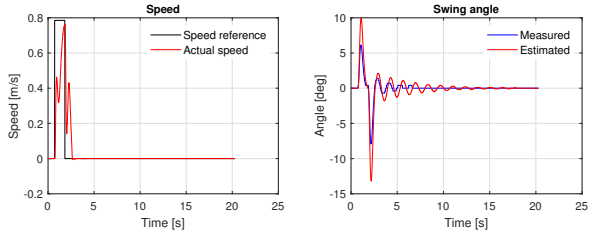

Figure 11. Speed reference and the actual speed and the measured and estimated swing angles when the swing angle feedback control using the measured angle is applied.

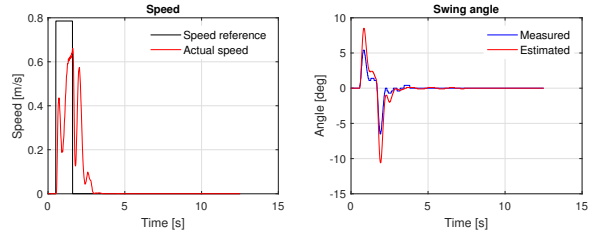

Figure 12. Speed reference and the actual speed and the measured and estimated swing angles when the swing angle feedback control using the estimated angle is applied.

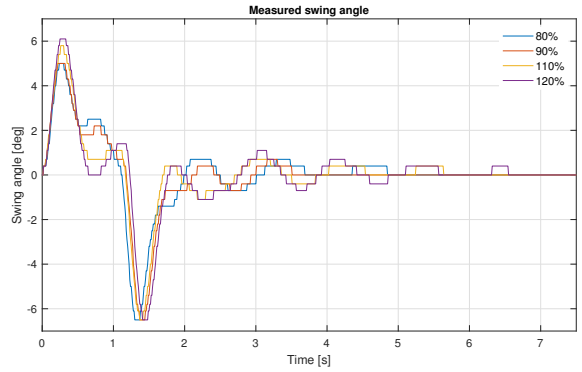

Figure 13. Measured swing angle when the hoist cable length is 80%, 90%, 110%, or 120% of the correct value.

5. Discussion

In this paper, we proposed methods for the swing angle control of a tower crane application with the main focus on reducing the payload oscillations. An extrainsensitive (EI) shaper and slew-angle-estimation-based closed-loop approaches were studied in a multibody simulator environment and by using an experimental small-scale setup.

The results indicate that although the input shaper suppresses load swing, it causes a long lag to the operator's commands. Moreover, the lag is also dependent on the hoist cable

length. From the crane operator's viewpoint, this can be difficult to learn to compensate. For instance, when the values l_{cable} = 19.2 m and V_{tol} = 0.05 are used for the EI shaper design, the amplitudes are $A_0 = 0.2625$, $A_1 = 0.4750$, and $A_2 = 0.2625$ with delays $\tau_1 = 4.4$ s and $\tau_1 = 8.8$ s, respectively. When the full movement is operated with the joystick, only 26.25% of the control action takes place in real time, and when the second impulse starts to take effect, the crane moves on about 75% of the operators command.

As an alternative method, a swing-angle-feedback-based control was proposed. The simulation results show that the suggested method is as effective or better than the input shaper for reducing the load swing, without causing a noticeable lag to the operator commands. Although the estimated angle differs from the measured one, the swing angle feedback works well when using the estimated information, as long as the estimated angle has the same phase and roughly the same amplitude as the measured angle.

The hoist cable length naturally varies during lift operations; hence, the control algorithms must adapt to the changes. If not measured, the cable length can be estimated using the hoist motor speed and information on the mechanics of the hoist system if the initial position is known. The initial position can be recorded by performing an identification run every time the system is powered on, for example. Robustness of the estimated swing-angle-based feedback control for error in the hoist cable length was also shown. According to the results, varying the hoist cable length between 80% and 120% of the actual hoist cable length does not significantly affect the performance of the control. In tower cranes, using estimators reduces the need for sensors, as the need of sensors can be undesirable in harsh environmental conditions. Both of the compared methods suffer from external disturbances, such as the force of wind, as they have no information on external forces. Cranes typically have a wind anemometer installed, but the size and shape of payloads vary greatly, which makes it unreliable to estimate the force of wind acting on the payload.

Although a tower crane was used as a case example, this routine can also be adopted to other types of crane. For example, an overhead crane (also called bridge crane) has a similar construction to the experimental setup and has only trolley and hoist movement. In the future, it would be interesting to study the effect of changing the tuning parameter K to an adaptive value as in [25]. This would, however, mean that the performance of the control should be monitored, in other words, the swing angle should be measured. This might pose a problem in a real crane but not in an experimental setup.

Author Contributions: Conseptualization, J.-H.M., N.N. and T.L.; Methodology, J.-H.M., T.L. and N.N.; Software, J.-H.M.; Investigation, J.-H.M.; Writing—original draft preparation, J.-H.M. and N.N., Writing—review and editing, J.-H.M.; Supervision, T.L. and M.N., Funding acquisition, T.L. and M.N., Project administration, T.L. and M.N. All authors have read and agreed to the published version of the manuscript.

Funding: This research received no external funding.

Institutional Review Board Statement: Not applicable.

Informed Consent Statement: Not applicable.

Data Availability Statement: Not applicable.

Conflicts of Interest: The authors declare no conflict of interest.

References

1. Smith, A.D. Comparison of Filtering Methods for Crane Vibration Reduction. *Tower Undergrad. Res. J.* **2009**, *1*, 1–7.
2. Vaughan, J.; Kim, D.; Singhose, W. Control of Tower Cranes with Double-Pendulum Payload Dynamics. *IEEE Trans. Cont. Syst. Technol.* **2010**, *18*, 1345–1358. [CrossRef]
3. Vaughan, J.; Singhose, W. Reducing Vibration and Providing Robustness with Multi-Input Shapers. In Proceedings of the American Control Conference, Saint Louis, Mo, USA, 10–12 June 2009; pp. 184–189. [CrossRef]
4. Blackburn, D.; Lawrence, J.; Danielson, J.; Singhose, W.; Kamoi, T.; Taura, A. Radial-Motion Assisted Command Shapers for Nonlinear Tower Crane Rotational Slewing. *Control Eng. Pract.* **2010**, *18*, 523–531. [CrossRef]

5. Lawrence, J.; Singhose, W. Command Shaping Slewing Motions for Tower Cranes. *J. Vib. Acoust.* **2010**, *131*, 1–11. [CrossRef]
6. Bariša, T.; Bartulović, M.; Žužić, G.; Ileš, Š.; Matuško, J.; Kolonić, F. Nonlinear predictive control of a tower crane using reference shaping approach. In Proceedings of the 2014 International Power Electronics and Motion Control Conference and Exposition, Antalya, Turkey, 21–24 September 2014; pp. 872–876. [CrossRef]
7. Duong, S.C.; Uezato, E.; Kinjo, H.; Yamamoto, T. A Hybrid Evolutionary Algorithm for Recurrent neural network Control of a Three-Dimensional Tower Crane. *Autom. Constr.* **2012**, *23*, 55–63. [CrossRef]
8. Rauscheru, F.; Sawodny, O. An Elastic Jib Model for the Slewing Control of Tower Cranes. *IFAC-PapersOnLine* **2017**, *50*, 9796–9801. [CrossRef]
9. Devesse, W.; Ramteen, M.; Feng, L.; Wikander, J. A real-time optimal control method for swing-free tower crane motions. In Proceedings of the IEEE International Conference on Automation Science and Engineering (CASE), Madison, WI, USA, 17–20 August 2013; pp. 336–341. [CrossRef]
10. El-Badawy, A.A.; Shehata, M.M.G. Anti-sway control of a tower crane using inverse dynamics. In Proceedings of the 2014 International Conference on Engineering and Technology (ICET), Cairo, Egypt, 19–20 April 2014; pp. 1–6. [CrossRef]
11. Qian, Y.; Fang, Y. Switching Logic-Based Nonlinear Feedback Control of Offshore Ship-Mounted Tower Cranes: A Disturbance Observer-Based Approach. *IEEE Trans. Autom. Sci. Eng.* **2019**, *16*, 1125–1136. [CrossRef]
12. Bai, W.W.; Ren, H.P. Horizontal positioning and anti-swinging control tower crane using adaptive sliding mode control. In Proceedings of the 2018 Chinese Control And Decision Conference (CCDC), Shenyang, China, 9–11 June 2018; pp. 4013–4018. [CrossRef]
13. Chang, C.Y. Adaptive Fuzzy Controller of the Overhead Cranes with Nonlinear Disturbance. *IEEE Trans. Ind. Inform.* **2007**, *3*, 164–172. [CrossRef]
14. Cekus, D.; Gnatowska, R.; Kwiatoń, P. Impact of Wind on the Movement of the Load Carried by Rotary Crane. *Appl. Sci.* **2019**, *9*, 3842. [CrossRef]
15. Slutej, A.; Kolonić, F.; Matuško, J.; Ileš, Š. Control of safety critical heavy industrial applications. In Proceedings of the 2014 16th International Power Electronics and Motion Control Conference and Exposition, Antalya, Turkey, 21–24 September 2014; pp. 958–962. [CrossRef]
16. Yoshida, K.; Matsumoto, I. Load transfer control for a crane with state constraints. In Proceedings of the 2009 American Control Conference, St. Louis, MO, USA, 10–12 June 2009; pp. 2551–2557. [CrossRef]
17. Teel, A. Using Saturation to Stabilize a Class of Single-Input Partially Linear Composite Systems. In Proceedings of the 2nd IFAC Symposium on Nonlinear Control Systems Design 1992, Bordeaux, France, 24–26 June 1992; pp. 379–384. [CrossRef]
18. Yanai, N.; Yamamoto, M.; Mohri, A. Feed-back control of crane based on inverse dynamics calculation. In Proceedings of the 2001 IEEE/RSJ International Conference on Intelligent Robots and Systems. Expanding the Societal Role of Robotics in the the Next Millennium (Cat. No. 01CH37180), Maui, HI, USA, 29 October - 03 November 2001 ; Volume 1, pp. 482–487. [CrossRef]
19. Terashima, K.; Kaneshige, A. Load-position control of overhead travelling crane in terms of fixed-pole approach for 3-D transfer path. In Proceedings of the 1999 European Control Conference (ECC), Karlsruhe, Germany, 31 August–3 September 1999; pp. 1070–1075. [CrossRef]
20. Halder, B. Anti-Swing Control of a Suspended Varying Load with a Robotic Crane. Master's Thesis, Russ College of Engineering and Technology of Ohio University, Athens, OH, USA, 2002.
21. Omar, H.M. Control of Gantry and Tower Cranes. Ph.D. Thesis, Virginia Polytechnic Institute and State University, Blacksburg, VA, USA, 2003.
22. Vaughan, J.; Yano, A.; Singhose, W. Comparison of robust input shapers. *J. Sound Vib.* **2008**, *315*, 797–815. [CrossRef]
23. Lindh, T.; Montonen, J.H.; Niemelä, M.; Nokka, J.; Laurila, L.; Pyrhönen, J. Dynamic performance of mechanical-level hardware-in-the-loop simulation. In Proceedings of the 2014 16th European Conference on Power Electronics and Applications, Lappeenranta, Finland, 26–28 August 2014; pp. 1–10. [CrossRef]
24. Baharudin, E.; Nokka, J.; Montonen, H.; Immonen, P.; Rouvinen, A.; Laurila, L.; Lindh, T.; Sopanen, J.; Pyrhönen, J. Simulation Environment for the Real-Time Dynamic Analysis of Hybrid Mobile Machines. In Proceedings of the 11th International Conference on Multibody Systems, Nonlinear Dynamics, and Control, Boston, MA, USA, 2–5 August 2015; Volume 6, pp. 1–11.
25. Soriano, L.A.; Rubio, J.d.J.; Orozco, E.; Cordova, D.A.; Ochoa, G.; Balcazar, R.; Cruz, D.R.; Meda-Campaña, J.A.; Zacarias, A.; Gutierrez, G.J. Optimization of Sliding Mode Control to Save Energy in a SCARA Robot. *Mathematics* **2021**, *9*, 3160. [CrossRef]

Publication III

Lindh, T., Montonen, J.-H., Grachev, M., and Niemelä, M.
Generating Surface Dynamometer Cards for a Sucker-Rod Pump by Using Frequency Converter Estimates and a Process Identification Run

Reprinted with permission from
Proceedings of 5th International Conference on Power Engineering, Energy and Electrical Drives (POWERENG)

Generating Surface Dynamometer Cards for a Sucker-Rod Pump by Using Frequency Converter Estimates and a Process Identification Run

Tuomo Lindh, Jan-Henri Montonen, Maxim Grachev, Markku Niemelä
School of Energy Systems
Lappeenranta University of Technology
Lappeenranta, Finland
tuomo.lindh@lut.fi

***Abstract*— This paper presents a novel method to generate surface dynamometer cards of a sucker rod pump by applying torque and rotational speed estimates of a variable speed induction motor drive and a pumping process identification run.**

Keywords—system identification; rod pump; estimate

I. INTRODUCTION

In pumping systems, sucker rod pumping is frequently used for artificial lifting of fluids, covering nearly two-thirds of the oil wells in operation around the world [1]. Nearly 70% of all the wells operate on sucker rod pumps [2, 3]. Fig. 1 illustrates a sucker rod pumping system.

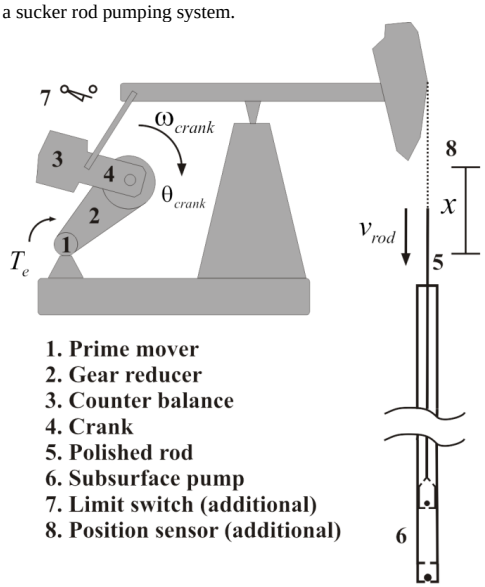

Fig. 1. Sucker rod pumping system.

A sucker rod pumping system consists of five basic parts: a prime mover, a gear reducer, a pumping unit, a sucker rod string, and a subsurface pump. In our case, the prime mover is a rotational-speed-controlled induction motor drive. The gear reducer increases the torque in order to adapt these values to the needs of the pumping system. The pumping unit transforms the rotating motion provided by the motor drive and the gear reducer into a reciprocating motion of the sucker rod string. The sucker rod string passes the reciprocating motion of the pumping unit to the downhole pump, mounted in the well. The subsurface pump sucks fluid (e.g. oil) from the well and brings it further to the surface.

The surface dynamometer card plots the force at the top of the rod string as a function of rod displacement. The cards are the main tool used to analyze the pumping performance, oil well conditions, and different abnormal operating conditions.

To generate a surface plot, the normal procedure is to install a dynamometer equipment comprising force and position sensors and a program that plots the force against the rod position. Another way to generate a plot is to use a motor torque signal and then calculate the polished rod force. The calculation can be carried out by using a kinematic analysis of a pumping unit as proposed by Liu et al. [4]. The proposed procedure has two main drawbacks: First, in order to calculate the kinematics, a very detailed model of the geometry is required, and second, the geometry varies between pumps and between different pump settings such as the rod stroke length or the gear ratio. We propose that an identification procedure can reveal the kinematic connection and forces affecting the pump with such an accuracy that the surface dynamometer card can be obtained without geometry information only by using the estimates produced by the frequency converter and with one additional limit switch. Thus, the system constitutes an intelligent drive.

The concept of an intelligent drive refers to a system where the drive adapts to the process, performs condition monitoring, or identifies the process that it is driving [5, 6, 7]. Sometimes, the term ‘intelligent drive’ refers to a system in which the motor parameters are automatically obtained during an identification run in a commissioning phase. In this paper, the

term ‘identification run’ is used for a system in which the required pumping process parameters are identified.

II. Test Setup

In order to be able to test the identification-based estimation of surface dynamometer cards, a simulation model of the whole rod pump system was established [8]. The block diagram of the rod pumping system model used is presented in Fig. 2.

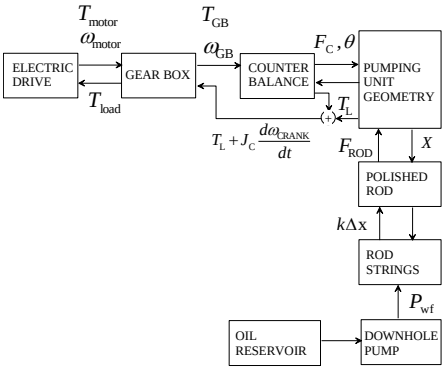

Fig. 2. Block diagram of the pumping system model.

The model consists of A) a detailed frequency converter model containing the actual converter control code and a two-axis induction motor model, B) a pumping geometry presented in [1, 4] comprising a gearbox, rod strings as a lumped flexible system, a downhole pump, and a simple well model as an RC circuit [8,9], where the capacitance reserves the inflowing oil that is flowing to the well through a resistance. The simulations in different operating conditions with different wells were executed. The results were compared with actual measurements in order to verify the simulation model. One of the results is plotted in Fig. 3 and Fig. 4.

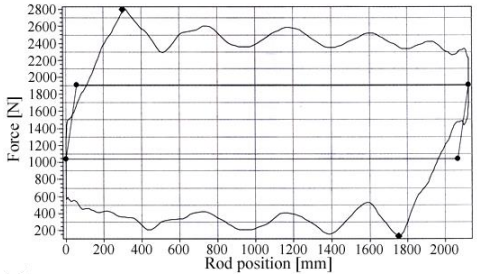

Fig. 3. Surface dynamometer card of an actual plant

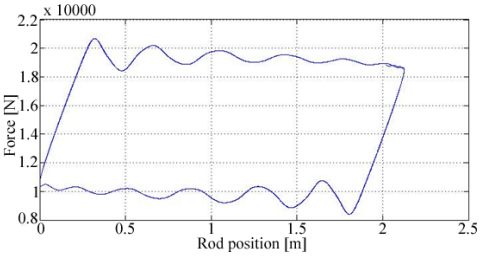

Fig. 4. Surface dynamometer card of a simulated plant.

III. Identification Procedure

The basic idea is to find a correspondence between the motor torque and the rod string force. The torque as a function of time or as a function of measured rod position does not directly correspond with the polished rod force as illustrated in Fig. 5 where motor torque is plotted as a function of the rod position. The main difference is due to a counterbalance torque. The counterbalance torque itself comprises two components; static moment and dynamic components caused by inertia. These two components can be isolated from each other in the identification because the latter is a function of rotational speed. The identification procedure does not and need not to ensure the source “no-load” torque components. Later on, these all are referred to as counterbalance torque because it is supposed to be the largest of all torque components that are not influenced by the polished rod force.

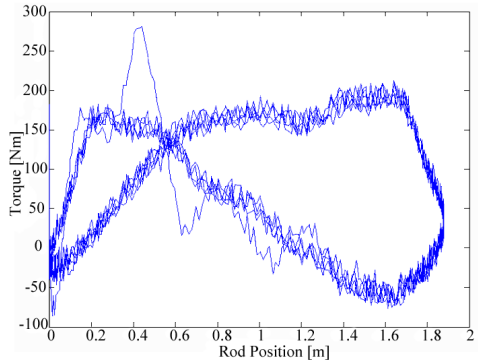

Fig. 5. Torque–position curve from the simulation model.

Neglecting the losses in the gearbox and the joints, it can be stated that the power produced must be equal to the power used in the rod and in counterbalance, which leads to equations

$$(T'_e + T_{CB}) \cdot \frac{\omega_{crank}}{v_{rod}} = P_{rod}$$
$$(T_e + T'_{CB}) \cdot \frac{\omega_{rotor}}{v_{rod}} = P_{rod} \quad (1)$$

where T'_e is the electrical torque estimate on the secondary side (crank side), T_{CB} is the counterbalance torque, T_e is the electrical torque estimate on the primary side (motor side), T'_{CB} is the counterbalance torque reduced to the primary side (motor side), ω_{crank} is the crank angular speed, v_{rod} is the rod speed, and ω_{rotor} is the rotor angular speed. It is necessary to know all the values from this equation to estimate the rod load. The electrical torque component can be estimated from the frequency converter, while the counterbalance torque component can be measured during the identification run of the pumping system with a zero rod load value. The rotational speed of the crank is not measured, and in addition, cannot be assessed by applying the gearbox ratio, because this value is not known in the case of an actual system, and the gearbox may have multiple values of ratio. The last value needed to determine the rod load is the rod speed, which can be calculated. The rod speed is a derivative of the rod position, and therefore, it is essential to have information about the rod position in order to obtain values of the rod speed.

Identification. The correspondence between the rod position and the motor angle incremental during one rod cycle can be achieved by an identification run. A limit switch is used to get information of one position during a cycle. The relation between the rotor angle and the polished measured or estimated rod position is recorded in a lookup table. This table will be used in the operational run of the system. In an actual application, the ID run procedure can be expressed by the following steps:

1) Obtaining the polished rod position signal during one operating cycle of the system, including the upstroke and downstroke of the rod.
2) Measuring the rotor speed (obtaining the rotor speed from the estimates of the frequency converter).
3) Integration of the rotor speed signal in order to obtain the rotor angle signal to establish a lookup table.
4) Application of a limit switch, which resets the estimates of the rotor incremental angle to zero every time when the polished rod reaches the limit switch.
5) The measured polished rod position is combined with the incremental values of the rotor angle position to establish a lookup table of values.
6) At the output of the identification run procedure, the set of angle position values is obtained and further applied to the operational run of the pumping system.
7) Measuring the "no-load" torque T'_{crank} ($\approx T'_{CB}$) by running the pump with a low velocity and with a normal operational velocity when the polished rod is dismantled from the supporting string.

One of the purposes of the identification run is to measure the ratio between the rod speed and the crank rotational speed, or simply between the rod position and the crank angle. When the ratio is known, the force applied to the rod can be estimated:

$$\hat{F}_{rod} = \frac{\omega_{rotor}}{\frac{\hat{x}_{rod}(t) - \hat{x}_{rod}(t-\tau)}{\tau}} (T_e - T'_{crank}) \quad (2)$$

The integration of the rotational speed estimate allows obtaining an estimate of the rotor angle. In addition, it can be mentioned that the rotor angle values are different from the crank angle values by the gearbox ratio. This yields

$$\begin{cases} \int_0^{t_1} w_{crank} dt = \theta_{crank}(t_1) \\ \int_0^{t_1} w_{rotor} dt = \theta_{rotor}(t_1) = \theta_{crank}(t_1) \cdot GR = \theta'_{crank} \end{cases}, \quad (3)$$

where θ_{crank} is the absolute angle of the crank from the limit switch and θ_{rotor} is the absolute angle of the rotor from the limit switch. Only the latter value is actually needed. $t = 0$ refers to the time of the limit switch triggering.

The rod position information in the identification run can be obtained in two ways: it can be provided by the measurement or it can be generated based on the known stroke length of the pumping system, limit switch information, and sinusoidal fitting. If sinusoidal fitting is used, no extra measurement hardware is needed in the identification phase, but the same limit switch used during an operational run triggers one phase in fitting. By applying the known angle value when a limit switch takes place in every round, it is possible to derive a formula for obtaining a sinusoidal signal of amplitude that equals the rod movement length A_{stroke}. The position of the rod can be calculated by

$$x = \frac{A_{stroke}}{2} \left(1 + \sin\left(\frac{\int w_r dt}{\theta_{2\pi}} \cdot 2\pi - \frac{\pi}{2} \right) \right), \quad (4)$$

where $\theta_{2\pi}$ is the integral of the rotational speed of the rotor of the motor during one cycle, or in other words, between two occurrences of the limit switch triggering. Of course, if the geometry does not guarantee a sinusoidal speed of the rod with a constant crank rotational velocity, a position measurement is needed during the identification run.

The block diagrams of the identification run and the operational run are presented in Fig. 6.

Operational run. The procedure of the operational run can be expressed as follows:

1) Measuring the rotor speed (obtaining the rotor speed estimate from the frequency converter) and application of a limit switch, which resets the values of the rotor angle to zero when the rod reaches the zero position.

2) Integration of the obtained rotor speed in order to get the rotor angle value at any moment.

3) Comparing the current value of the rotor angle with the corresponding value in the lookup table, which was produced during the ID run.

4) After the rotor angle and the corresponding position of the polished rod at a certain point in time are known, the rotational speed of the crank and the polished rod are calculated for instance by applying a direct Euler model of the derivative as presented in (2). This is done to avoid accumulation of errors resulting from using direct derivatives.

5) Establishing a ratio between the rotational speed of the crank and the rod velocity for further calculation of the load.

6) Obtaining overall torque estimates, including the "no-load" torque component from the ID run and an electrical torque component from the frequency converter estimates.

7) Multiplication of the ratio and the overall torque gives the load that the polished rod undergoes during operation.

8) Preparation of surface force plots by means of the estimated rod load and the obtained position values.

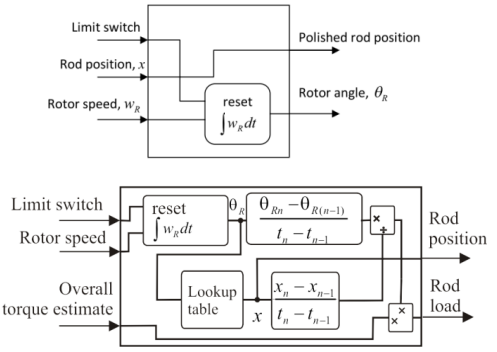

Fig. 6. Scheme of an identification run and an operational run.

IV. Test Results

The generation of the identification-run-based surface dynamometer cards was tested by executing identification runs and operational runs with a simulation model, and further, the estimated surface plots obtained by using (2) and (3) were compared with the force as a function plot directly produced by the simulation model. One of the results is illustrated in Fig. 7.

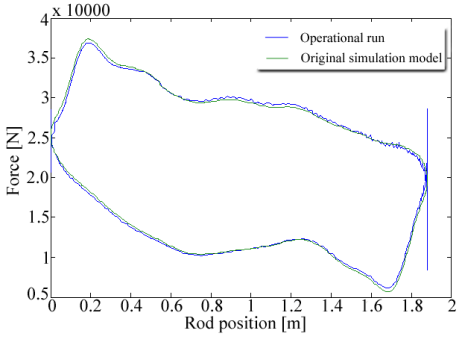

Fig. 7. Dynamometer card comparison

The curve resulting from the operational run fits the original one in terms of covered area (work) with an accuracy of 99% and a negligible error of less than 2% in force. However, these values were obtained assuming that the frequency converter estimates are accurate. The accuracy of the frequency converter estimates of induction-motor-driven systems was measured by Ahonen [10]. He concluded that the relative errors of the estimates are quite low for all the three investigated parameters: 0.2% for the rotational speed, 2.1% for the shaft torque, and 2.1% for the shaft power. This error directly increases the uncertainty of the surface plot. However, if the estimation errors are expected to be noncorrelating, the uncertainty is not increased by more than 3%. The gearbox and joint friction, on the other hand, are taken into account already in the identification run as a part of the "no-load" torque, and the error to the force estimate is only due to the variation in these friction forces.

V. Conclusions

There are a few possible options for plotting dynamometer cards; most of these methods employ quite complicated instrumentations and devices to record load values applied to a polished rod and to obtain the rod position signal. In this paper, a novel method for surface dynamometer card plotting was presented. The method applies torque and rotor rotational speed estimates obtained from the frequency converter and the correspondence identified between the torque and the load for the calculation of the load that the polished rod undergoes. The only measurement device that has to be added to the pump control is a limit switch. The polished rod force can be calculated in the frequency converter or in an automation device such as a high-performance PLC.

REFERENCES

[1] Tacaks, Gabor. 2003. Sucker-Rod Pumping Manual. s.l. : PennWell Books.

[2] Moore S. D. Well Servicing Expenditures, Activity Drop Substantially

[3] Marcelo Hirschfeldt, Paulino Martinez, Fernando Distel. "Artificial-lift systems overview and evolution in a mature basin: case study of golfo San Jorge", Society of Petroleum Engineers. 2007.

[4] Xinfu Liu, Yaoguang Qi, Chunhua Liu, Jianjun Wu . "An approach to the computation of motor loading for a pumping unit.", 2nd International Conference on Industrial Mechatronics and Automation. 2010.

[5] Schonfeld, R., Franke, M., Hasan, H.,Muller, F., "Intelligent drives in systems with decentralized intelligence.",Fifth European Conference on Power Electronics and Applications, Brighton,1993.

[6] Nevaranta N., Niemela M., Lindh T., Pyrhonen O., Pyrhonen J., "Position controller tuning of an intermittent web transport system using off-line identification", Power Electronics and Applications (EPE), 2013, Lille, France

[7] Montonen J-H., Lindh T., "Event-seeking Mass Estimator for Hybrid Working Machine", 13th International Symposium "Topical Problems in the Field of Electrical and Power Engineering". Pärnu, Estonia, 14-18 Jan. 2013

[8] Neklepaev, N., Rod pump control, 2012.. Master's thesis. Lappeenranta University of Technology.

[9] Bogdan M. Wilamowski, Fellow, IEEE, and Okyay Kaynak,"Oil Well Diagnosis by Sensing Terminal", IEEE Transactions on Industrial Electronics, Vol. 47, No. 5, October 2000.

[10] Ahonen, Tero, Tamminen,Jussi, Ahola, Jero, Niemelä, Markku. 2011. Accuracy study of frequency converter estimates used in the sensorless diagnostics of induction-motor-driven systems. LAPPEENRANTA UNIVERSITY OF TECHNOLOGY, Department of Electrical Engineering.

Publication IV

Lindh, T., and Montonen, J.-H., Niemelä, M., Nokka, J., Laurila, L., and Pyrhönen, J.
Dynamic performance of mechanical-level hardware-in-the-loop simulation

Reprinted with permission from
2014 16th European Conference on Power Electronics and Applications

Dynamic Performance of Mechanical-level Hardware-In-the-Loop Simulation

Tuomo Lindh, Jan-Henri Montonen, Markku Niemelä, Jarkko Nokka, Lasse Laurila, Juha Pyrhönen
LAPPEENRANTA UNIVERSITY OF TECHNOLOGY
Skinnarilankatu 34
Lappeenranta, Finland
Tel.: +358 / (0) – 400705961
E-Mail: Tuomo.Lindh@lut.fi
URL: http://www.lut.fi

Keywords

«Real time simulation», «Test bench», «Modelling», «Electrical drive», «Device simulation».

Abstract

This paper discusses dynamic behavior, stability and performance issues of the mechanical-level hardware-in-the-loop (MHIL) simulation. A special interest is in the cases where a real-time multi-body mechanics simulator is used to produce load dynamics to HIL hardware. The transfer functions describing the HIL system dynamics are created and presented. The analysis using transfer functions, the simulation results and test results using actual MHIL simulation are presented. The analysis shows that the performance and stability of the device under test cannot be concluded without case by case analysis of HIL-setup as a whole.

Introduction

Mechatronic systems driven by controlled electrical drives can be analyzed without actual mechanics by using a virtual testing. The virtual testing can use a multi-body dynamic modeling approach. The multi-body system is a structure constructed with flexible or rigid bodies that are connected by joints or force elements [1,2,3]. The joints can be modeled using combinations of different basic constraints that define the allowable movement between bodies connected to these. The force elements consist of springs, dampers, or more complicated actuators, in this case electric motors and other components such as gears and brakes. The multi-body simulator often interacts with a virtual landscape, and a human-machine interface (HMI) of an actual machinery. When considering modeling techniques of this kind, without going into details, one can come to a conclusion that such a model needs a specific tools and models of electric drives, independent of the multi-body system. This co-simulation sometimes utilize Software-In-the-Loop (SIL) [1, 4] or Hardware-In-the-Loop simulations (HIL) concept. In the SIL concept, a simulated mechanics is driven by simulated drive including the actual drive control software. In the HIL concept, an actual drive under test (DUT), or some components of it, are used as a part of simulation setup. The actual application motor drive can be tested on the simulation consisting of a real-time simulation of mechanics and of an electric motor drive that emulates this mechanics. The method is usually referred to as a Mechanical-level Hardware-In-the-Loop system [5, 6]. Other types of the HIL are a Signal-level simulation where the DUT is a controller connected with the real-time-simulator, and a Power-level HIL where electric power is exchanged between a System Under Test (SUT) and a controlled electric load.

HIL systems have been used for years for a rapid prototyping in different applications [7,8,9,10,11]. Most of the studies present their setups and demonstrate the performance by giving experimental results. The properties of the electric drives as a load emulator have been discussed in a few studies [6,13]. The dynamic performance of PHIL systems was analyzed e.g. by Lentijo [6] and of MHIL by Correa [13]. However, the MHIL as a dynamic system generally, or the combination of multi-body

mechanics simulator and MHIL as a dynamic system, have not been presented. Fig. 1 presents a laboratory HIL setup comprised of a multi-body crane simulator, a relaying program, a separate control program interface and a downscaled crane application motor drive and a load emulator drive. The LED drive is a standard AC frequency converter with an induction or a PM-servo motor.

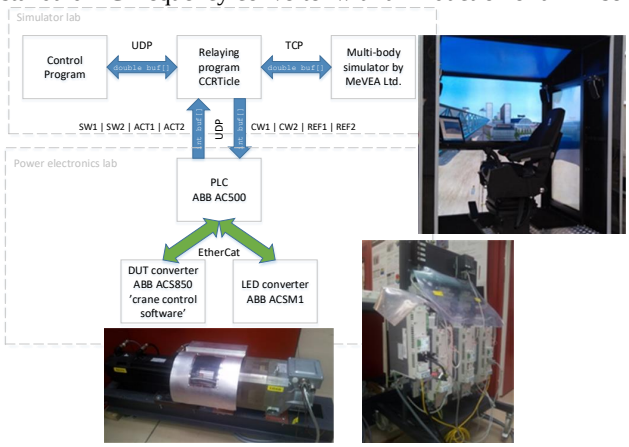

Fig. 1: A laboratory HIL setup comprised of multi-body crane simulator, relaying program, separate control program interface and a downscaled crane application motor drive and a load emulator drive.

Mechanical HIL as a dynamic system

In Fig. 2, a block diagram of the HIL setup is presented. The DUT drive in the left side can be controlled by a rotational speed or a torque reference. The controllers of rotational speed $G^{\omega}_{\mathrm{CTRL1}}$, torque G^{T}_{CTRL1}, and a torque amplification of an inverter reference to actual torque K_{inv1}, are presented in equations as one transfer function G_{C1}. The DUT motor G_{M} is connected to a LED motor G_{ML} forming a back-to-back configuration. LED motor is driven by an inverter, that takes its rotational speed reference from the output of the multi-body mechanics model G_{MB}. The model takes a torque estimate T_{act1} of DUT drive as an input if motor inertia J_{M} is neglected or included in G_{MB}. Otherwise, the input is a mechanical torque T_{m1} calculated by

$$T_{m1} = T_{act1} - J_M \frac{d\omega_{act}}{dt}. \tag{1}$$

The LED-drive, referenced by the subscript 2, has the same components as the DUT. The performance of the LED drive is measured by terms of ability to follow a rotational speed reference obtained from a multi-body mechanics simulator when different torque profiles are generated by the DUT. In case of the perfect control, the error between reference and measurement should be zero. The dynamics of the drives and delays in the system makes it impossible to obtain a perfect control. In practice, the error should be zero in steady state and attenuate quickly after transients.

As illustrated in Fig. 2, the both drives, DUT and LED, can use rotational speed reference because the reference of LED drive is constructed of the response of the multi-body mechanics simulator taking the actual torque of the DUT drive as an input. This is very useful feature, because the same setup can be used for testing the drives using either the rotational speed or torque references. However, the performance and stability conditions of the HIL are different in these two different modes as will be shown in the stability analysis.

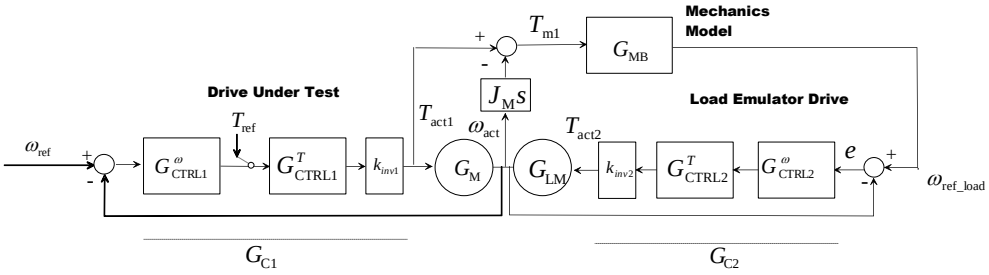

Fig. 2: A block diagram of HIL-system. Drive under test can take either a rotational speed or a torque references. G_{C1} is a DUT frequency converter G_M is a DUT motor. G_{C2} and G_{ML} are the controller and the motor of load emulator drive. G_{MB} is a real-time multi-body simulator.

The MHIL back-to-back setup mechanically consists of two motors fixed together, driven by torques produced by DUT and LED drives. Thus, the two mechanical models of motors G_M and G_{LM} of Fig.1 can be combined into one block with a model

$$G_M^{'} = \frac{\varpi}{T_{act1} + T_{act2}}(s) = \frac{1}{(J_M + J_{ML})s + B} \ , \tag{2}$$

where J_M and J_{ML} are inertias of motors of DUT and LED drive and B is a friction of back-to-back setup. Using this, the block diagram of Fig. 2 can be drawn in a new form as presented in Fig. 3. In the figure, the system is presented in a form where one can conclude the factors that affect stability and also the analytical calculation can be performed. One should be able to test the real DUT dynamics which is given by

$$\frac{\varpi_{act\_DUT}}{\varpi_{ref\_DUT}}(s) = \frac{G_{C1}G_{M,MB}}{1 + G_{C1}G_{M,MB}} \ , \tag{3}$$

where $G_{M,MB}$ is a combined dynamics of DUT motor and load mechanics. If a connection between motor and load is rigid and a motor inertia is low, compared to the load, motor often has no effect on dynamics of system and can be expected to have unity transfer function in analysis. The transfer function of the HIL system can be obtained from Figs. 2 or 3, and is given by

$$\frac{\varpi_{act}}{\varpi_{ref}}(s) = \frac{G_{C1}G_M^{'} + G_{C1}G_{C2}G_{MB}G_M^{'}}{1 + G_{C2}G_M^{'} + G_{C1}G_M^{'} + G_{C1}G_{C2}G_{MB}G_M^{'}} \ . \tag{4}$$

The dynamics of transfer functions of eqs. 3 and 4 should be ideally equal which is impossible. In the HIL-setup, the controllers and the motors of both DUT and LED as well as the multibody load model contribute the dynamics causing that the performance of actual application drive (eq. 3) and HIL are different. The stability conditions are also different so that, in order to be able to test stability of the DUT, the HIL should be designed case by case. Thus, the aim is to tune LED drive G_{C2} and G'_M so that dynamics of eqs. 3 and 4 are as similar as possible over whole control bandwidth of the DUT while G_{C1} and G_{MB} are determined by the DUT drive and mechanics (model). As illustrated in Fig. 3, the system forms a cascade where the LED drive converter model is in inner loop and in series with mechanics model G_{MB}. The gain of G_{C2} must be low enough to ensure the stability. In addition, the communication delay between drive setup and multi-body mechanics model, which is not analyzed in this paper, can cause instability.

The DUT drive is often driven by a torque reference instead of a rotational speed reference. In this case, one should be able to test the dynamics of the DUT which is given by

$$\frac{\varpi_{\text{act\_DUT}}}{T_{\text{ref\_DUT}}}(s) = G_{CTRL1}^{T} k_{inv1} G_{\text{M,MB}} \ . \tag{5}$$

In the HIL setup, the outer feedback loop of Fig. 2 is cut and the control G_{C1} contains only torque control G_{CTRL}^{T}. In this case, the transfer function of the HIL system is given by

$$\frac{\varpi_{\text{act}}}{T_{\text{ref}}}(s) = \frac{\left(G_{CTRL1}^{T} k_{inv1} G_{\text{MB}} G_{C2} + G_{CTRL1}^{T} k_{inv1}\right) G_{\text{M}}^{'}}{1 + G_{C2} G_{\text{M}}^{'}} = G_{CTRL1}^{T} k_{inv1} G_{\text{MB}} \frac{G_{C2} G_{\text{M}}^{'}}{1 + G_{C2} G_{\text{M}}^{'}} + G_{CTRL1}^{T} k_{inv1} \frac{G_{\text{M}}^{'}}{1 + G_{C2} G_{\text{M}}^{'}} \ . \tag{6}$$

The dynamics of eqs. 5 and 6 are quite similar if G_{C2} is large. Stability of the system again depends both on the DUT control G_{CTRL}^{T} and the LED control G_{C2} as well as on the HIL motor set G'_{M}. Large gain of G_{C2} that is required for keeping dynamics similar, can cause an unstable HIL system.

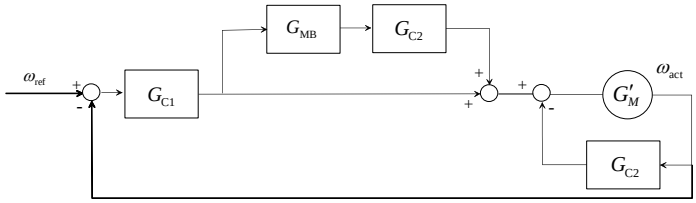

Fig. 3: A modified block diagram of HIL-system.

Performance of LED as a part of MHIL

The performance of LED is analyzed in two different cases. Firstly, if DUT changes acting torque, the rotational speed should not be affected directly but only through the load model G_{MB}. Secondly, if the load model output ω_{ref_load} changes, the rotational speed should follow independently of acting torque T_{act1}. A block diagram of Fig. 4 presents the setup of these tests. Sensitivity to DUT torque variations and ability to response to the rotational speed reference ω_{ref_load} can be measured by error term

$$e = \omega_{ref\_load} - \omega_{act} \ . \tag{7}$$

that should, remain zero all the time in order to achieve perfect control, or remain near zero at whole control bandwidth ω_c. The performance can be analyzed with a transfer function

$$\omega_{\text{act}}(s) = \frac{G_{C2} G'_{\text{M}}}{1 + G_{\text{C2}} G'_{\text{M}}} \omega_{\text{ref}}(s) + S_{\text{d}} T_{\text{d}}(s) \ , \tag{8}$$

where the DUT torque estimate T_{act1} is described by the disturbance term T_{d} and the sensitivity to the disturbance is approximately

$$S_{\text{d}} = \frac{\omega_{\text{act}}}{T_{\text{d}}} = \frac{G'_{\text{M}}}{1 + G_{\text{C2}} G'_{\text{M}}} \ . \tag{9}$$

If the DUT mechanical torque T_{m1} is used as disturbance term T_{d}, then G'_{M} should be replaced by G_{LM} in eq. 9. The disturbance model is presented in Fig. 4.

The disturbance can take any form. However, in practice, the torque rise time and the bandwidth of the torque signal are determined by the DUT drive. Therefore, it can be adequate to use ramps and sinusoidal test signals and possibly steps to test the performance. The sensitivity to disturbances can be tuned so that error peaks during disturbances remain low and a steady state error remains zero.

For example, if we expect that the torque control is perfect (has gain 1 at control bandwidth), the rotational speed controller is a PI-controller, and the friction term of the motor model is neglected, then, eq. 9 can be written in form

$$\frac{\omega_{\mathrm{act}}}{T_{\mathrm{d}}}(s)=\frac{1/Js}{1+\frac{K_{\mathrm{p}}k_{\mathrm{inv2}}(1+T_i s)}{T_i s}\frac{1}{Js}}=\frac{T_i s}{T_i Js^2+K_{\mathrm{p}}k_{\mathrm{inv2}}T_i s+K_{\mathrm{p}}k_{\mathrm{inv2}}} \quad . \tag{10}$$

It can be seen directly by setting s=0 that a steady state error to step disturbance is zero, if the system is stable. In addition, the steady state error to a ramp disturbance R is

$$e_{\mathrm{ss}}=\lim_{t\to\infty}e(t)=\lim_{s\to 0}sE(s)R(s)=$$
$$\lim_{s\to 0}\frac{T_i s^2}{T_i Js^2+K_{\mathrm{p}}k_{\mathrm{inv2}}T_i s+K_{\mathrm{p}}k_{\mathrm{inv2}}}\frac{A}{s^2}=\frac{T_i A}{K_{\mathrm{p}}k_{\mathrm{inv2}}} \quad , \tag{11}$$

where A is a rate of ramp of T_{d}. In order to achieve good performance, the integration time should be small, proportional gain and torque producing amplification k_{inv2} should be large and ramp rise time should be limited. The effect of disturbance torque ramp slope can be limited by dimensioning of the LED drives. If the LED drive k_{inv2} is doubled the effect of ramp A is halved.

The mechanics model including e.g. environment model cannot completely be given by a transfer function. Therefore, the output of multi-body mechanics simulator and, consequently, the changes in rotational speed reference of the LED, can only be tested by using the multi-body simulator without the MHIL setup and recording the results. The results can then be used to determine the required control bandwidth.

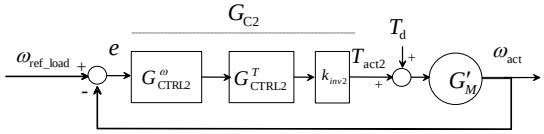

Fig. 4: A block diagram of the LED drive when the DUT torque is presented as disturbance.

Test setup

The performance of the HIL setup of Fig. 1 was tested by constituting a crane control application simulation. The crane control is interesting in a way that it is very poorly damped system. In addition, even if it can be modeled as a simple second order system, the flexible frames and hoisting wire introduce dynamics that is very difficult to model without a multi-body mechanics model approach. Physical test setup consists of back-to-back connected 4-kW (T_{N}=10.8 Nm, J=0.002 kgm^2) and 4-kW or 8-kW (T_{N}=31.1 Nm, J=0.017 kgm^2) induction servo machines with frequency converters. The crane model was created by multi-body mechanics simulator by Mevea corporation. The application control software runs alternatively as a SIL simulator or in actual hardware (ABB ACSM1 frequency converter and/or AC500 PLC). A crane driver controls movements of the simulator by assigning joystick and pedal commands. A slew movement rotational speed reference is fed to the application program which is executed in the crane application drive (ABB ACS850). That drive produces the torque T_{act1}. The torque estimate from drive is relayed back to simulator G_{MB} which then calculates the movements. The slew motor rotational speed from G_{MB} is relayed to the LED drive as rotational speed reference $\omega_{\mathrm{ref\_load}}$. If the error term of eq. 7 remains zero or exists only during large transient the simulation is valid and application drive (DUT) sees the load emulating drive as it was a real slew motion of crane. In order to be able to analyze and tune the HIL setup with a known mechanics model, the multibody simulator was replaced in the first phase by a discretized version of a reference plant model

$$G_{\mathrm{MB}}(s)=\frac{0.01}{s^2+0.06s+0.01}\ . \tag{12}$$

The hoist wire length changes the natural frequency of the system so that several plant models have to be analyzed.

Tests

The stability and performance of HIL setup was analyzed, simulated and tested. The tests were executed with setup of Fig. 1. Two mechanics models were used: the discretized version of the reference plant model of eq. 12, and finally, the multi-body crane model.

In the first phase, the dynamic properties of the HIL-setup and the DUT with the reference plant model were analyzed by comparing eqs. 3 and 4 and (eqs. 5 and 6 if the torque reference was used). If there exist different operational modes in mechanics model then the analysis should be made for all of these. The dynamics of the reference plant model driven by the DUT and the HIL should equal at control bandwidth and same stability conditions should exist. In the Fig. 5, the calculated bode plots and a step responses are given for the case where the plant model was controlled so that the overshoot was limited to 30 percent. The phase margin of reference DUT model is 18.5 degrees and of HIL setup 16.8 degrees. The gain margin of HIL-setup is 9.48 dB. Step responses of HIL-setup and DUT model are quite similar and one could think that the stability of DUT could be tested now by changing parameters of DUT drive only. This, however, is not possible. By increasing the proportional gain of DUT reference drive by factor four, the phase margin of reference DUT model decreases to 10 degrees. Phase margin of the HIL setup gets now the negative value -3.64 degrees, and HIL-setup goes unstable. This is illustrated in Fig. 6. Also, it is possible that with some other tuning parameters, the HIL setup can stabilize the unstable DUT drive. It can be concluded by analyzing the eqs. 3 and 4 and from the results of analysis, that the LED drive control parameters have to be tuned for different DUT control parameters. This is done by using transfer function equations or by simulating separately the DUT drive and HIL-setup. Also, using a software-in-loop simulation instead of HIL simulation is often a feasible solution, because there exist no such limitations as in the HIL.

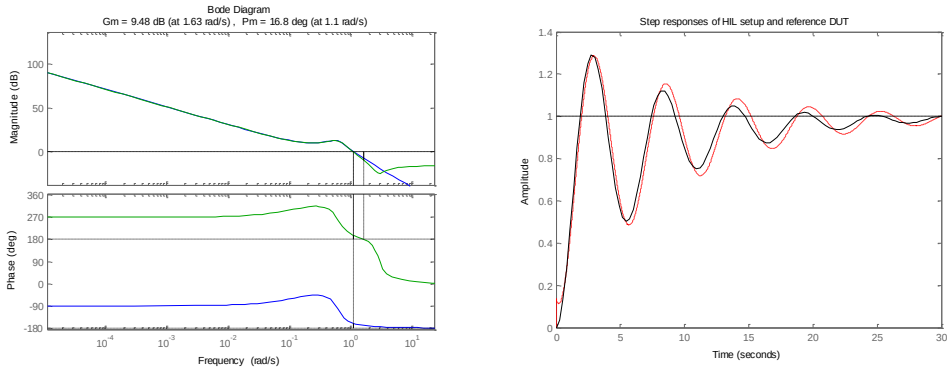

Fig. 5: Bode plots and step responses of reference DUT drive model and of HIL setup. The green line in bode plot refers to HIL setup. The step response of HIL setup is drawn with the solid line.

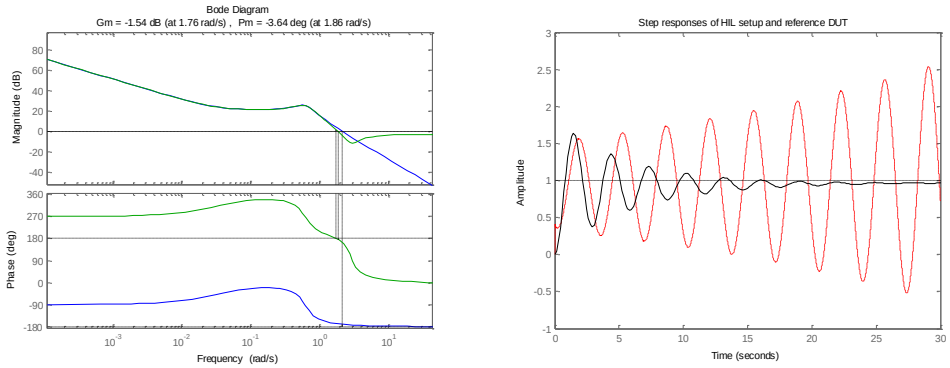

Fig. 6: Bode plots and step responses of the reference DUT drive model and of HIL setup. The green line in bode plot refers to HIL setup. The step response of HIL setup is drawn with the solid line.

In the second phase, the discretized version of the reference DUT plant model (eq. 12) was executed as a part of the actual HIL-setup. The rotational speed reference step was given to the DUT drive when same control parameters were used as the ones used in Figs. 5 and 6. The results recorded by ABB DriveStudio-program are presented in Fig. 7. The First step response is stable and the second is unstable, as expected. In the figures, it can be noticed that actual drives restrict torque, which cause that the responses do not have pure sinusoidal resonance.

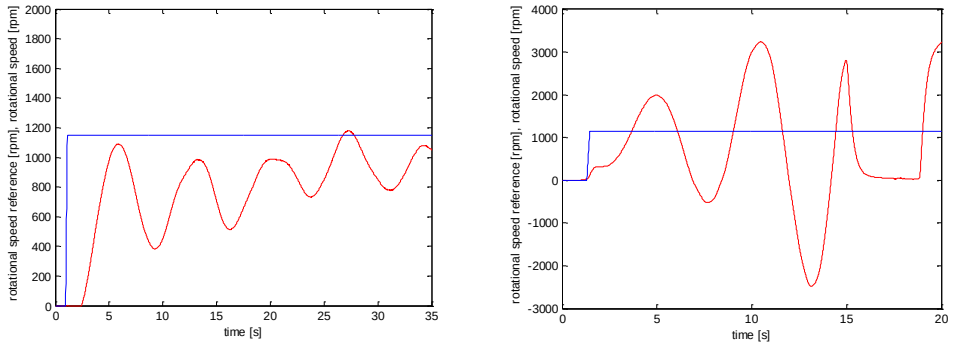

Fig. 7: Step responses of reference HIL setup with control parameters used in Figs.5 and 6.

In the next phase, the performance of LED-drive (eq.8) was tested. Firstly, the ability to follow the rotational speed reference was tested, and secondly, the LED rotational speed sensitivity to disturbance torque analyzed and tested.

A first part, the ability to follow the rotational speed reference was tested by applying the ramp and sinusoidal references to the LED drive while the DUT drive was loaded to the rated torque 10.8 Nm. In order to achieve good performance, a gain G_{C2} should be large, which requires large enough torque amplification k_{inv2}. In the present setup k_{inv2}/ k_{inv1} equals to 31.1 Nm/ 10.8 Nm. The gain and phase shift of eq. 8 can be directly obtained when sinusoidal references with different frequencies are fed to system. The multi-body mechanics model can change reference rotational speed in different ways. The rotational reference changes when the mechanics model responses to input. In addition, different ambient factors can cause the multi-body mechanics model to produce different changes. For example, in case of vehicle application, driving to uphill can cause a ramp shape reference reduction of the LED, when in the worst case, the DUT application is driving with full torque. In the crane application, the wind load can cause a ramp shape reference in gusty wind conditions. Both sinusoidal and ramp shape rotational speed references (ω_{ref_load}) were tested. In Fig. 8, it is illustrated how the LED drive controller follows the rotational speed reference.

In Fig.9, the sensitivity of LED rotational speed to disturbance torque produced by the DUT is illustrated. The sensitivity plot according eq. 9 is given in frequency domain with different LED drive controller gains. The plot shows that using the gains selected for stability and used to plot Fig. 5, the sensitivity is near to -40 dB. The result is verified by driving disturbance torque ramps from DUT drive when LED drive is rotating at rated rotational speed. When 0.1 seconds ramps from zero up to rated torque and back are driven, the rotational speed fluctuates approximately one percent as can be seen in the figure on the right.

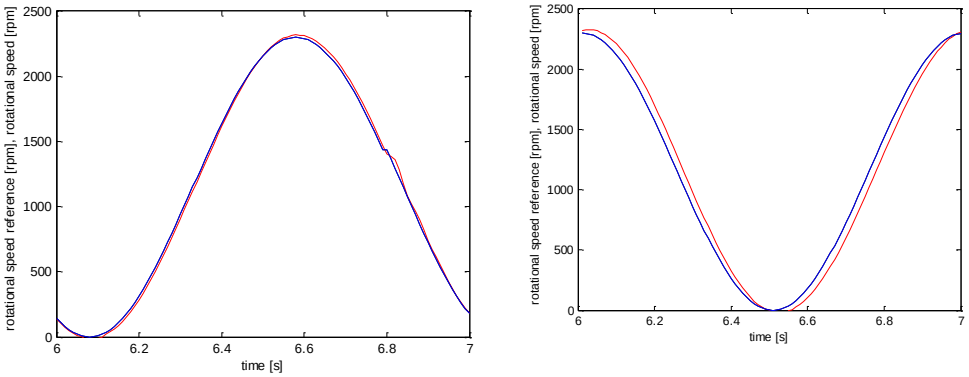

Fig. 8: Test for performance of LED-drive. The sinusoidal, one hertz, rotational speed reference between zero and rated rotational speed is presented with two different proportional gain. The first one results in very low rotational speed error. However, this controller gain results unstable HIL-setup with existing parameters. The rotational speed error of either figures at any time instant results mainly from phase shift.

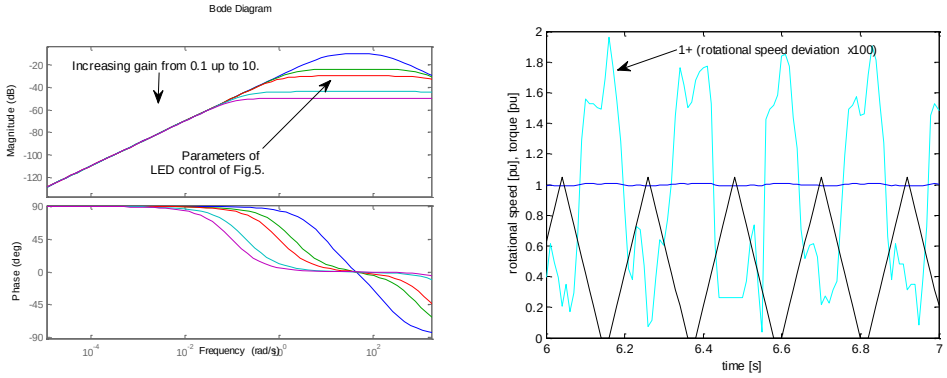

Fig. 9: Test for the LED rotational speed sensitivity to the DUT drive torque. The left figure illustrates the sensitivity according eq. 9 with various controller gains. The red curve is drawn with the controller values used in Fig. 5. Higher controller gain decreases the sensitivity. The right figure shows a result when a ramp disturbance torque (black curve) is given from DUT drive. Blue curve is a rotational speed (pu-value) and light blue illustrates the deviation.

In the Fig. 10, the actual crane multi-body model was connected as a part of MHIL. The system response to step shape rotational speed references of DUT drive are presented. The proportional gain and integration time of LED drive controller were the tunable variables. The left hand side figure shows a situation where proportional gain is 20 and integration time 3 seconds. The response from multi-body simulator is presented as reference to LED drive (as negative) and actual angular speed follows well the reference. The error magnified by ten cannot be attenuated totally during transient. However, the steady-state error remains zero. In the right side figure the integration time was reduced to 1 second. The error term remains lower at the beginning, but multi-mechanics model and back-to-back drive setup start to oscillate heavily.

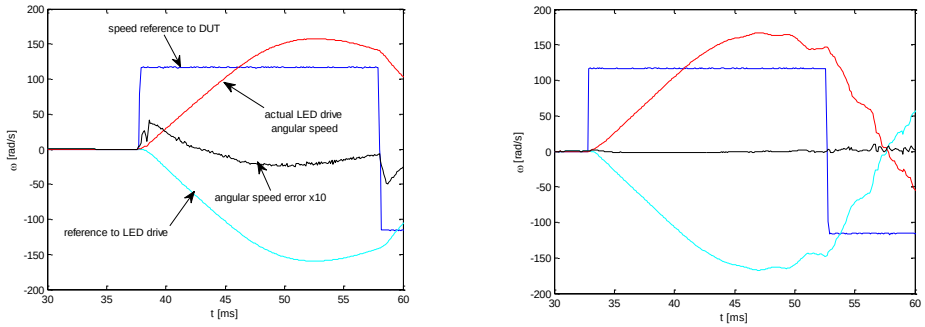

Fig. 10. Speed reference step tests using the crane multi-body crane model as a part of the MHIL setup. The figures show results with 2 different LED drive controller integration times. A tighter control of the figure in the right results heavy oscillations in speed.

Conclusion

The paper presented the equations that can be used to analyze dynamic behavior, stability and performance issues of mechanical-level hardware-in-the-loop simulation, especially when a multi-body mechanics simulator is a part of loop. It was shown that the dynamics of the application mechanics with drive under test (DUT) and of mechanical-level hardware-in-the-loop (MHIL) differ inevitably. The dynamics of HIL setup is affected both by the DUT drive and by the load emulating drive (LED). In order to achieve similar dynamics for both at control bandwidth, the performance and stability issues have to be analyzed case by case. Further, it is required that different LED drive controller tuning has to be used for different DUT controller parameters. A good tool for a supervision of the HIL setup performance during operation is the error term of the LED drive rotational speed controller input.

References

[1] Lindh, T. ”Simulation, modeling, and virtual testing of electric-drive-powered mechatronic systems”, 8th International Conference-Workshop on Compatibility and Power Electronics (CPE 2013). Ljubljana, Slovenia, June 2013.

[2] Shabana A., “Flexible Multibody Dynamics: Review of Past and Recent Developments,” in Multibody System Dynamics, Kluwer Academic Publishers, 1997, 189–222.

[3] Korkealaakso P., Mikkola A., Rantalainen T., and Rouvinen A., “Description of joint constraints in the floating frame of reference formulation,” In Proc. IMechE, Vol. 223 Part K: J. Multi-body Dynamics, 2009.

[4] Montonen, J., Montonen, J.-H., Immonen, P., Murashko, K., Ponomarev, P., Lindh, T., Lindh, P., Laurila, L., Pyrhönen, J., Tarkiainen A. (Visedo Ltd), and Rouvinen, A. (MeVea Ltd), ”Electric Drive Dimensioning for a Hybrid Working Machine by Using Virtual Prototyping”, in ICEM 2012.

[5] Boyscayrol A, “Different types of Hardware-in-the-Loop simulation for electric drives”, IEEE International Symposium on Industrial Electronics, 2008, pp. 2146-2151

[6] Lentijo S., D’Arco S., Monti A., “Comparing the Dynamic Performances of Power Hardware-in-the-Loop Interfaces”, IEEE Trans. Ind. Electron., Vol. 57, no. 4, pp.1195-1207, April 2010

[7] Youngsong L. and Woon-Sung L.,” Hardware-in-the-loop Simulation for Electro-mechanical Brake” SICE-ICASE International Joint Conference 2006, October 2006, Bexco, Busan, Korea

[8] Zhang Q., Reid J. F., Wu D., "Hardware-in-the-loop simulator of an off-road vehicle electrohydraulic steering system", Trans. on ASAE, September 2001, pp. 1323-1330

[9] W. Lhomme, R. Trigui, P. Delarue, A. Bouscayrol, B. Jeanneret, F. Badin, “Validation of clutch modeling for hybrid electric vehicle using Hardware-In-the-Loop simulation”, IEEE-VPPC’07, Arlington (USA), September 2007

[10] Jeeho L., Namju J., Hyeongcheol L., ”HIL Simulation Approach for Feasibility Study of a Tram with Onboard Hybrid Energy Storage System”, in Proc. ICCAS-SICE, 2009, pp. 5305-5312

[11] Hanselmann, H., “Hardware-in-the-Loop Simulation Testing and its Integration into a CACSD Toolset,” in Proceedings of the 1996 IEEE International Symposium on Computer-Aided Control System Design.

[12] Michael Angelo A. Pedrasa and Vincent Louie S. Delfin “Low Cost Mechanical Load Emulator”, University of the Philippines - Diliman, Quezon City Philippines

[13] Correa B.A., Zhang Y., Fang R., Dougal R. A.,” Driving a Synchronous Motor so That It Emulates a Twin-Shaft Gas Turbine Engine”, Power Electronics, Machines and Drives (PEMD 2012)

[14] Achour, T. ; Pietrzak-David, M., ” An experimental test bench for a distributed railway traction mechanical load emulator”, IECON 2012

[15] Bacic M., “On Hardware-in-the-loop simulation”, in Proc. 44th IEEE Conference on Decision and Control, and the European Control Conference, 2005, pp.3194-3198

Publication V

Montonen, J.-H., Lindh, T., Lana, A., Peltoniemi, P., Pinomaa, A., Tikkanen, K., and Pyrhönen, O.

Comparison of Different Power Balance Control Methods for Battery Energy Storage Systems on Hybrid Marine Vessels

Reprinted with permission from
IEEE Access
Vol. 10, pp. 58578–58588, 2022

IEEE Access
Multidisciplinary ⋮ Rapid Review ⋮ Open Access Journal

Digital Object Identifier 10.1109/ACCESS.2022.3179716

Comparison of Different Power Balance Control Methods for Battery Energy Storage Systems on Hybrid Marine Vessels

JAN-HENRI MONTONEN[1], TUOMO LINDH[1], ANDREY LANA[1], PASI PELTONIEMI[1], (Member, IEEE), ANTTI PINOMAA[1], KYÖSTI TIKKANEN[1], and OLLI PYRHÖNEN[1], (Member, IEEE)
[1]Lappeenranta–Lahti University of Technology LUT, Yliopistonkatu 34, 53850 Lappeenranta, Finland

Corresponding author: Jan-Henri Montonen (e-mail: henri.montonen@lut.fi).

This work was done as a part of the Integrated Energy Solutions to Smart and Green Shipping (INTENS) research supported by Business Finland.

ABSTRACT In this paper, different power balance control methods for hybrid marine vessels are analyzed. First, the power grid of a marine vessel is modeled using MATLAB and Simulink. Simulations are then performed using real power plant load data captured from an actual vessel. Isochronous control is used to control the power of the diesel gensets, and different control methods, such as isochronous control and average load power estimation, are used for the battery energy storage system. The system is simulated with different control parameters, and the effects of parameter changes are presented. It is shown that these presented control schemes can be adapted to manage the energy balance in a hybrid vessel, thereby enabling efficient use of the battery energy storage system. A diesel genset and battery energy storage system failure during a dynamic positioning operation is also simulated, and the effect of the failure on the frequency of the power grid of the vessel is presented.

INDEX TERMS AC grid, battery energy storage system, dynamic positioning, hybrid vessel, isochronous control, simulation, Simulink

I. INTRODUCTION

BATTERY energy storage systems (BESS) can be used in marine vessels to attain improved fuel economy and to achieve reduced emissions [1]. One application of a BESS is peak power shaving, in which power peaks are shaved by drawing power from the BESS, thus enabling steady load on the power plant diesel engines [2], [3]. Hence, for the performance in maritime operations, the rated power of the diesel engines can be smaller than in a similar vessel not equipped with a BESS. In this manner, hybridization can bring benefits in terms of the lower CAPEX and OPEX of a marine vessel [4]. In this work, an Offshore Supply Vessel (OSV) is used as a case vessel. OSVs are a vessel type used for supplying cargo and personnel to oil drilling or other offshore construction sites. In addition, OSVs can also be equipped to operate as anchor handling, sea exploration, or accommodation vessels. When on duty, OSVs can use their thrusters and main propulsion to stay in position relative to the sea bed or a moving object. This is called dynamic positioning (DP) [13]. The average power demand in the DP mode is small compared with the power demand in the cruise mode. However, load transients can be fast, especially in rough sea conditions. In many cases, the need to accommodate load transients is handled by running more gensets than what would be required by the average load power demand.

The BESS needs to be controlled in an appropriate way to achieve a high fuel efficiency of the gensets and to ensure a stable network frequency during load transients and a stable vessel operation during fault situations. Different methods for vessel power balance control for vessels with and without a BESS have been presented in the literature to mitigate the fluctuating load power demand caused by the propulsion. Model-based predictive control for battery power has been presented in [5], [6], and different types of energy storages have been suggested in the literature. For example, the use of flywheels, batteries, and ultracapacitors has been studied for the mitigation of power fluctuation in vessel power distribution systems in [7]–[10]. In [11] a

power management method based on filtering load power is presented as means for load sharing between power sources with different response times. In [10], fuzzy logic control was used to calculate a power reference for a hybrid energy storage consisting of a battery and an ultracapacitor. Thruster power was modulated to mitigate the load variations caused by other power consumers on the vessel in [12]. During dynamic positioning (DP), however, this approach causes small deviations to the commands given by the DP system, which may be undesirable in some cases. Additionally, thrusters can be driven in opposite directions to enable fast switching of thrust direction by reducing thrust from the opposite direction [14], [16]. Running thrusters in opposite directions, however, reduces the energy efficiency of the vessel. Thrusters can also be used to mitigate power fluctuations when there is a sudden drop of load power by increasing the thruster power [12]. Also, strategic loading of the energy storage to improve fuel efficiency has been studied in [15]. It was shown in [17] that by equipping an OSV with a BESS, transients can be taken from the BESS and the average power can be produced by running fewer gensets. These gensets then run on a higher load and use less fuel per produced kWh.

This study investigates isochronous-control-based power control methods for a BESS in hybrid vessels using a detailed simulation model. The model allows to investigate power, frequency, voltage, and current from the grid, instead of only power flow. Data recorded from an actual vessel is used as load power data. Three methods are proposed to run a BESS in a marine vessel already equipped with isochronous load sharing for the gensets. This enables the retrofitting of a BESS to a vessel already using isochronous control for the gensets and a constant-frequency AC grid for power distribution. To the best of the authors' knowledge, isochronous control has not been introduced as a control method enabling this advantageous usage of a BESS. It is interesting to compare the traditional isochronous control with the average power control in order to reveal the performance of both control laws in hybrid vessels.

II. CONTROL METHODS

Isochronous control is used to control the gensets and to enable load sharing in a powerplant. The study considers three control methods. In the first control scheme, the BESS is treated like a genset. The power reference for the BESS is formed using the isochronous control scheme described in Section II-A.

The second control method calculates an average load power estimate and uses the difference between the estimated and actual load power as the power reference for the BESS. This control scheme is presented in Section II-B. The third control scheme is start–stop, which is based on an isochronous control in which one diesel genset (DG) is running constantly and one is started and stopped based on the load power demand. This approach increases fuel efficiency as the DGs run on a higher load. The control scheme is presented in Section II-C.

TABLE 1. Example of the diesel genset power division for a four-genset isochronous system.

Genset number	p_i	b_i	$p_{\text{ref, i}}$
1	0.8	0	0.6
2	0.5	0.2	0.8
3	0.8	0	0.6
4	0.5	0	0.6

A. ISOCHRONOUS CONTROL

In the isochronous load sharing mode, each genset compares its produced power against the biased and weighted average produced power per genset as presented in (1). The effect of biasing and weighting is then removed from the power references of the gensets, (2). The biased average power $\overline{p}$ is calculated as

$$\overline{p} = \frac{1}{n}\sum_{i=1}^{n}\frac{p_i - b_i}{c_i} \tag{1}$$

where p_i is the produced power of the genset i, c_i is the load gain, b_i is the load bias, and n is the number of running gensets. With the load gain and the load bias, a genset can be "fooled" to produce more power as it believes that the other gensets are producing more power than it is. The load bias can be used to set a constant difference between the produced powers of the gensets. The load gain can be used to set a constant ratio between the produced powers of the gensets. The load gain and the load bias are useful when unbalanced load sharing is desired, e.g., to save fuel or to reduce the load on one genset. The power reference for the genset i is calculated as

$$p_{ref,i} = \overline{p}c_i + b_i \tag{2}$$

For clarification, an illustrative example of a four genset system is given in Table 1. For simplification, c_i is assumed to be equal to one. The actual genset power in per units is shown in the p_i column, and the load bias is shown in the b_i column. The nominal power of the genset corresponds to 1 p.u. The average power $\overline{p}$ is calculated using (1) and the values in the p_i and b_i columns. The average power of $\overline{p} = 0.6$ p.u. is attained.

The power reference for each genset is calculated using (2), and it is shown in the P_{ref} column. A load bias of 0.2 p.u. was set for DG2, which can be seen as a 0.2 p.u. higher power reference compared with the other gensets. The load gain c_i was set to 1 for simplification.

The engine power is controlled using a PID fuel rate controller. The controller error signal is a combination of power and speed errors

$$e = K_1(p_{\text{ref}} - p_{\text{act}}) + K_2(\omega_{\text{ref}} - \omega_{\text{act}}) \tag{3}$$

where K_1 and K_2 are the gains that are used to weight the power reference or the frequency reference. ω_{ref} is constant 1.0 p.u. [18].

Isochronous control is also used to control the power reference going to the BESS. The power reference is formed by:

$$p_{\text{ref,BESS}} = K_1(\overline{p}c_{\text{BESS}} + b_{\text{BESS}}) + K_2(K_p e(t) + K_i \int_0^t e(\tau)d\tau) \quad (4)$$

where $e(t) = \omega_{\text{ref}} - \omega_{\text{act}}$. Equation (4) does not take the State-of-Charge (SOC) of the BESS into account. In a real-world case, SOC control would be mandatory, because otherwise the control scheme would drain the battery. The SOC control could be implemented as it was done in the start–stop case in Section II-C by adding an additional P-type controller to $p_{\text{ref,BESS}}$. Then, (4) would be:

$$p_{\text{ref,BESS}} = K_1(\overline{p}c_{\text{BESS}} + b_{\text{BESS}}) + K_2(K_p e(t) + K_i \int_0^t e(\tau)d\tau) - K_{\text{p,SOC}}(SOC_{\text{ref}} - SOC_{\text{act}}) \quad (5)$$

where $K_{\text{p,SOC}}$ is the gain of the SOC controller, SOC_{ref} is the SOC reference value, and SOC_{act} is the actual value of the BESS SOC. The SOC controller is used to produce an offset to the $p_{\text{ref,BESS}}$, which causes the BESS to charge or discharge over time. The integral part is omitted from the controller, because the purpose of this SOC control is not to drive the SOC to its reference value. The purpose of the SOC controller is to prevent overcharging and overdischarging and to make sure that there is energy in the battery for the frequency control. A PI-type controller could also be used, but the integration time would have to be long in order to prevent power fluctuation of the DGs caused by the SOC control.

B. AVERAGE LOAD POWER ESTIMATION

The power reference for the BESS is calculated using the difference between the current load power and the average load power:

$$P_{\text{ref,batt}} = P_{\text{load}} - P_{\text{ave}} \quad (6)$$

where P_{load} is the actual consumed power, and P_{ave} is the calculated average power over the calculation period. P_{ave} is calculated by using a moving average filter of

$$p_{\text{ave}}(n) = \frac{1}{M}[p_{\text{load}}(n - M - 1) + ... + p_{\text{load}}(n)] \quad (7)$$

where M is the length of the moving average window. Average power can be calculated during operation, and M and the sample time should be selected so that enough averaging is obtained but the delay caused by the filter is not too long. The selection of the filter length requires adaptation, manual or automatic. A simple moving average can be replaced by a predictive estimator [5], [19].

C. START–STOP

The start–stop enables the shutdown of superfluous gensets when the load power demand is low enough and the reduced number of gensets are capable of producing the average load. Load transients can be handled by the BESS. In this mode, one genset runs constantly and one genset is started and stopped according to the load demand. All gensets are controlled using the isochronous control described in Section II-A. The control weight parameters K_1 and K_2 are changed based on the number of running gensets. During the simulation, one genset runs constantly. When only one genset is running, it is on the 100% frequency control. When the second genset is started, the first genset remains mainly in the frequency control mode, and the second one is mainly in the power control mode. The start and stop of the second genset are determined by the load power limits. If the load power is higher than the start limit, the genset is started. When the load power goes below the stop limit, the genset is stopped.

The power reference for the BESS is formed as a sum of two P-type controller outputs. The first is for the AC network frequency control and the second for the SOC control of the battery. The BESS power and SOC control is illustrated in Fig. 1. In this case, the BESS power control is a modified isochronous control with weights $K_1 = 0$ and $K_2 = 1$ with the SOC control by the added P-type controller parallel to the frequency control. The integral part was removed from the frequency controller, because the BESS is supposed to participate in peak load shaving only, i.e., it should not take part in the frequency control in the steady state.

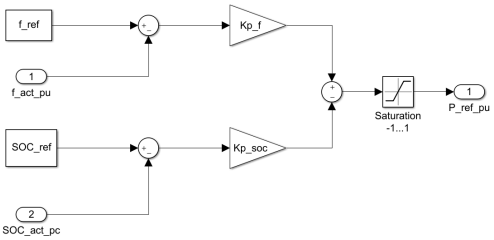

FIGURE 1. Power control scheme of a battery energy storage system (BESS) in the start–stop simulation

III. SIMULATION MODELS

MATLAB/Simulink is used for the simulation of the vessel power system and the proposed control. The simulation models are built from the main components such as the generator set, the BESS, the propulsion load, and the hotel load. These main components are described in the following subsections. The components are built from fundamental blocks and Simscape blocks. The simulation models are continuous time models, but a discrete solver with a 50 μs timestep is used for the Simscape models.

The vessel model is built based on Single Line Diagram (SLD) and component data of the actual vessel. A simplified

SLD of the case vessel is shown in Fig. 2, and the Simulink model is presented in Fig. 3.

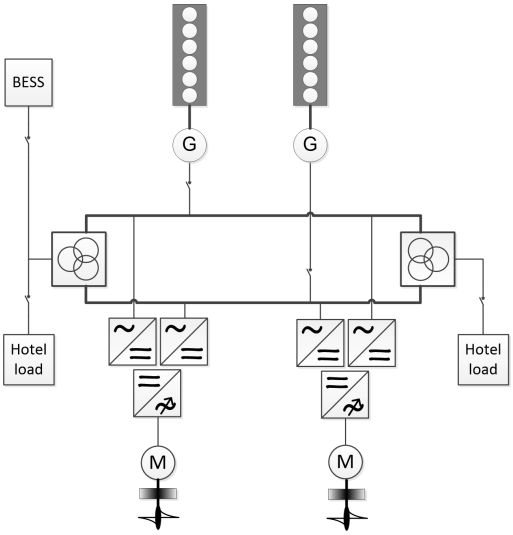

FIGURE 2. Offshore supply vessel (OSV) single line diagram (SLD) from which the Simulink model is built.

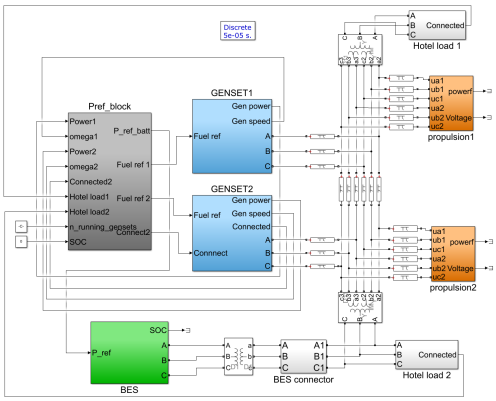

FIGURE 3. Top level of a hybrid OSV simulation model. The model contains diesel gensets (blue blocks), the BESS (green block), propulsion loads (orange blocks), the power control (grey block), and the hotel load (white blocks near the propulsion loads)

A. DIESEL GENSET

The diesel genset model is a transfer function model tuned to have a similar response to the real diesel genset in the vessel. A model presented in [3] could also be used, but it would require many engine-specific parameters, which can be hard to acquire. The diesel genset model is the model used previously in the simulations presented in [17]. The model consists of a diesel engine model and a generator model. Fig. 4 describes the top level of the diesel genset model. The generator model in Fig. 4 is a standard Simscape library synchronous motor block.

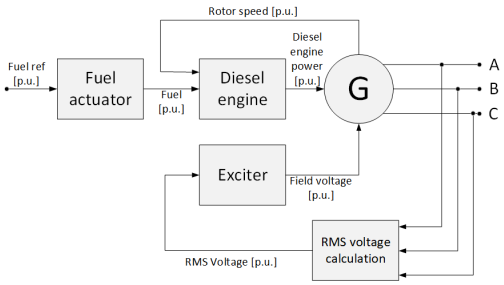

FIGURE 4. Diesel genset model consisting of a diesel engine model and a generator model.

The diesel engine model consists of the fuel actuator and the engine itself, as shown in Fig. 5. The input to this block (fuel reference) comes from an external power control block, which is simulation case-specific. The diesel engine model block outputs power and torque.

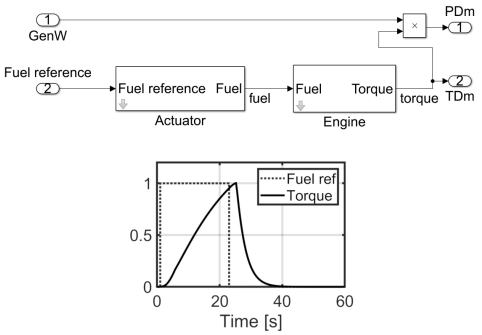

FIGURE 5. Diesel engine model block diagram and a step response of the Actuator–Engine system from the fuel reference to the torque of the diesel engine.

The actuator model in Fig. 5 is shown in detail in Fig. 6. The engine model is presented in Fig. 7. The produced torque of a diesel engine is a product of air and fuel. A three-second delay model for the increase of fuel injection is used. The turbo delay constitutes the longest delay in the system. The delay is modeled with a first-order transfer function in which the time constant can be tuned to produce the fastest possible gas circulation dynamics or the dynamics that follow the soot production restrictions given to the diesel by the manufacturer [20].

IEEE Access

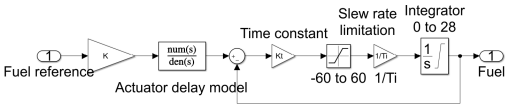

FIGURE 6. Actuator model of the diesel engine.

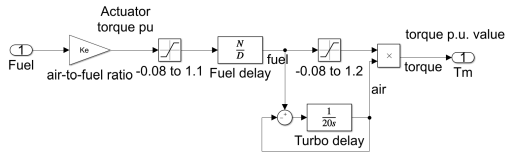

FIGURE 7. Contents of the engine model.

B. BATTERY ENERGY STORAGE SYSTEM

The top level of the battery energy storage system is presented in Fig. 8. The BESS model contains a battery model and a grid converter model. The battery model is a standard Simscape battery model, which can be parameterized to fit each simulation case.

The grid converter is controlled by a power reference signal coming from an external power reference block. The power reference is fed to the current controller of the grid converter as the i_d current reference. The grid converter keeps track of the grid angle by a phase-locked loop. The converter model is simplified to reduce the computational load and does not contain switches; they are replaced with voltage sources. This type of model is called an averaging model. The model is based on the model presented in [21] and [22] with the phase-locked loop presented in [23].

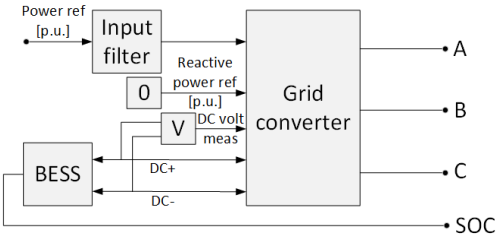

FIGURE 8. Top level of the BESS model. The model consists of a Simscape battery model and an averaging grid converter model.

C. PROPULSION LOAD

The propulsion load block models the whole propulsion load of the vessel, i.e., the main propulsion and the thruster loads. The model does not contain a model of an actual drive; rather, the propulsion drive is modeled by a controlled current source that sinks power from the DC link. The model consists of a power transformer model, two diode bridge models, a DC link model, and a current source model (see Fig. 9). The propulsion power data (from an actual vessel or artificially generated test data) can be loaded from a text file. The DC link model of Fig. 9 is presented in Fig. 10.

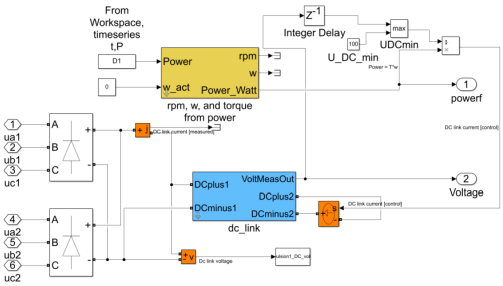

FIGURE 9. Top level of the propulsion model. The model consists of two diode bridge models, a DC link model, and a current source model.

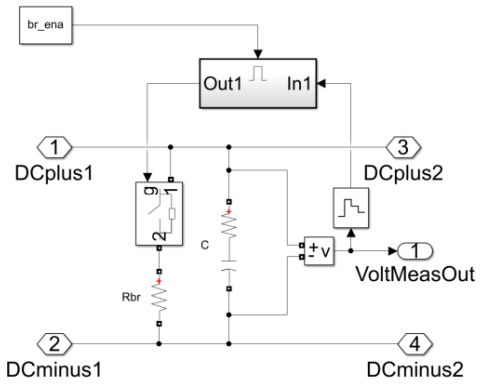

FIGURE 10. DC link model of a propulsion load model.

D. HOTEL LOAD

The hotel load comprises all loads other than the propulsion load. The hotel load consists mainly of lighting, pumps, fans, and other electrical systems on the vessel. The hotel load is modeled using a Three-Phase Parallel RLC Load model from the Simscape library, as illustrated in Fig. 11. The hotel load power remains static during the simulation. The total hotel load value used in the simulations is 400 kW. The three-phase Breaker and Hotel load connector blocks connect the load to the Power Distribution System (PDS) after 60 s from the simulation start. The delay is to prevent a load impact on the gensets while they are spooling up. The three-phase load and breaker models are connected with PI section cable models.

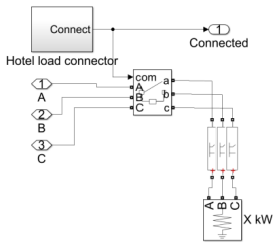

FIGURE 11. Hotel load model consisting of a three-phase breaker model and a three-phase parallel RLC load model.

IV. RESULTS

The simulation model was run using the load power data presented in Fig. 12. The load power consists of the static base load (hotel load) and the dynamic thruster and propulsion load. The data were obtained from an actual vessel, and they depict loading during the DP mode. These load power data are used in all the simulated cases, except for the start–stop case where higher power consumption is needed and artificial test data are used. The simulations tested various scenarios, such as:

- Loading in DP-mode
  - -- Traditional isochronous control without a BESS
  - -- Modified isochronous control with a BESS
    - ∗ BESS power reference from the isochronous control
    - ∗ BESS power reference from the average load power estimation
    - ∗ Start–stop with a BESS
- Robustness during malfunction
  - -- Genset failure
  - -- BESS failure

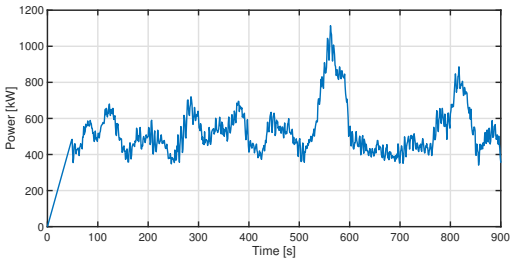

FIGURE 12. Load power used in the simulations.

The parameters of the different simulation model components are presented in Table 2. These parameters are kept constant during simulations. The table includes references to the figures and equations where the component is displayed.

TABLE 2. General model parameters that remain constant during simulations

Unit	Parameter	Value
BESS	Nominal power	3.1 MW
	Capacity	310 kWh
	Nominal DC voltage	1050 V
	C-rate	10
BESS isochronous control (Eq.4)	K_1	0.7
	K_2	0.3
	b_{BESS}	0
	c_{BESS}	1
	K_p	10
	K_i	0.01
BESS start–stop (Fig. 1)	$K_{\text{p,f}}$	10
	$K_{\text{p,soc}}$	0.01
Diesel genset: actuator (Fig. 6)	K	1.4286
	Actuator delay model	$\frac{1}{0.025s+1}$
	Gain K_t	8.33
	Integration time T_i	1
Diesel genset: engine (Fig. 7)	Gain K_e	1
	Fuel delay model	$\frac{1}{3s+1}$

TABLE 3. Simulation parameters of different isochronous cases without a BESS

Genset nbr	Parameter	Case 1	Case 2	Case 3	Case 4
1	K_1	0.3	0.3	0.3	0
	K_2	0.7	0.7	0.7	1
	c	1.0	1.5	1.0	1.0
	b	0	0	0.2	0
2	K_1	0.7	0.7	0.7	n/a
	K_2	0.3	0.3	0.3	n/a
	c	1.0	0.5	1.0	n/a
	b	0	0	0	n/a

A. ISOCHRONOUS CONTROL WITHOUT A BESS

The OSV model is simulated without a BESS in four different isochronous cases to test the effect of different load sharing parameters. Case 4 tests whether the vessel is able to run in the DP mode using only one genset because of the small load power. The studied cases are:

- Two gensets running, equal load sharing (Case 1)
- Two gensets running, load gain set (Case 2)
- Two gensets running, load bias set (Case 3)
- One genset running on speed reference (Case 4)

The parameters of these cases are presented in Table 3.

Fig. 13 and Fig. 14 present the network frequency and the genset power during the simulations. Fig. 13 shows that one genset alone is unable to keep the network frequency near the setpoint. Although one genset is able to produce sufficient power for the DP operation, the dynamic response of one genset is not fast enough and the network frequency never quite reaches the setpoint. Two gensets have sufficiently fast dynamics to be able to produce the required thruster power transients. Fig. 13 also shows that varying the isochronous control parameters (load gain and load bias) under load

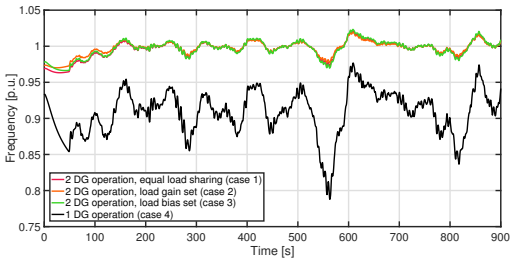

FIGURE 13. Generator speed (also AC-grid frequency) in different isochronous modes

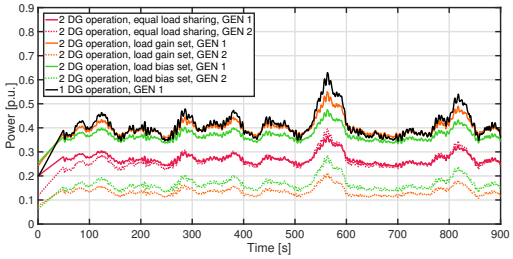

FIGURE 14. Generator power in different isochronous modes.

variations does not have a significant effect on the variation in frequency. Genset power while using different isochronous parameters is presented in Fig. 14. The figure shows how the different isochronous parameters change the load sharing between the gensets. Equal load sharing parameters result in equal load sharing among the gensets. Setting the load bias or the gain will result in one genset producing the set amount of more power than the other.

When using equal load sharing (Case 1), both gensets produce the same power ($c = 1$ and $b = 1$). In Case 2, $c = 1.5$ for DG1 and $c = 0.5$ for DG2. Consequently, DG1 will produce 1.5 times the average power, and DG2 will produce 0.5 times the average power. In Case 3, the load bias is set so that DG1 will constantly produce 20% over the average power. In Case 4, only one genset is running. In this case, it runs only on the frequency reference ($K_1 = 0$ and $K_2 = 1$).

The mean value and variance of the AC network frequency are presented in Table 6 for all the simulated cases. It can be seen from the table that the isochronous load sharing parameters (b, c) have a very small effect on the frequency of the AC network.

B. ISOCHRONOUS CONTROL WITH A BESS

The behavior of the BESS when included in the isochronous control is analyzed in the following simulation. A BESS model was added to the simulation model, and the system was simulated using the load power data in Fig. 12. In the simulation, only one genset is running and the BESS supports this genset. Average load power estimation and isochronous control are used to control the power of the BESS.

When using isochronous control, the BESS is treated like a genset. The genset runs primarily on frequency reference ($K_1 = 0.3$ and $K_2 = 0.7$), and the BESS runs primarily on power reference ($K_1 = 0.7$ and $K_2 = 0.3$). Both have equal load sharing parameters (c = 1 and b = 0). The power reference for the BESS is formed by (4).

When using the power reference for the BESS from the average load power estimation, the power reference is formed as described in Section II-B as the difference between current power consumption and filtered power consumption. The length of the averaging filter used is 120 s.

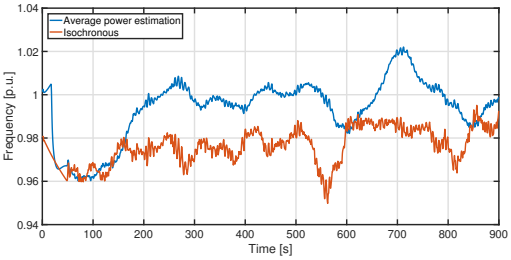

FIGURE 15. Frequency of the AC grid in one diesel genset operation with the BESS.

From Fig. 15, it can be seen that running the BESS with a power reference from the average load power estimator gave closer to the 1 p.u. frequency during the simulation than the alternative method where the BESS is treated like a genset. Table 6 shows that the mean frequency value difference is 1.7%. The difference in variance is small between the two methods. According to Table 6, the isochronous control results in a smaller variance in the AC frequency than the average load power estimation. However, if we neglect the droop at the beginning of the simulation, the average load power estimation results in a smaller variance.

The sudden load increase at t=550 s causes a smaller drop in the AC frequency when using the average load power estimation than with the isochronous control. When using the average load power estimation, the BESS power reference increases immediately when the load power increases, but when using the isochronous control for the BESS, the frequency must first drop so that a frequency error to which the controller can react will form.

Fig. 16 presents the genset and BESS power during the simulated DP operation. When running the BESS with the average load power estimation, the BESS operates in the peak-shaving mode, whereas the genset produces the base load. The average BESS power is close to zero, and thus, the BESS is charged and discharged during the operation and the SOC does not drift. The power reference sent to the BESS from the average load power estimation is not shown in the

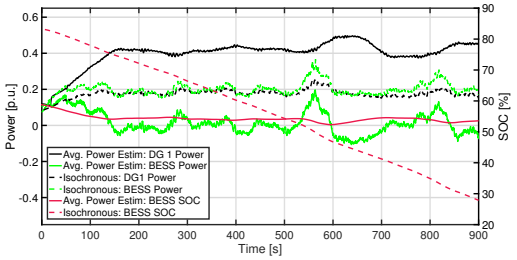

FIGURE 16. Diesel genset and BESS power while in the DP mode and running only one genset.

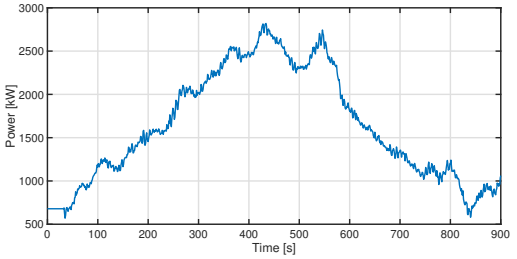

FIGURE 17. Artificial load signal used in the start–stop simulations.

TABLE 4. Genset parameters of the start–stop simulation.

Genset nbr	Parameter	1 DG Operation	2 DG operation
1	K_1	0	0.3
	K_2	1	0.7
	c	1	1
	b	0	0
2	K_1	n/a	0.7
	K_2	n/a	0.3
	c	n/a	1
	b	n/a	0
	start limit	n/a	2000 kW
	stop limit	n/a	1500 kW

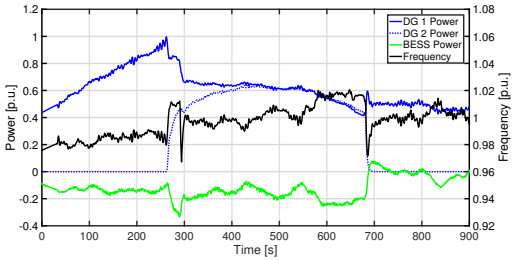

FIGURE 18. AC network frequency, genset power, and BESS power during the start–stop simulation.

figure, because it would be below the actual power curve of the BESS.

When running the DG and the BESS on isochronous load sharing, both produce the same power and the BESS is discharged during the operation. A BESS charge controller was not used in this simulation, but the controller described in Fig. 1 could be used to modify the power reference as the SOC drops. Alternatively, when the lower limit of the BESS SOC is reached, charging of the battery is started and another genset must possibly be started.

C. START–STOP

The load power signal is artificial in this simulated case. An artificial load signal was used to achieve high enough power consumption to justify the starting of another genset. The load signal is created by adding a triangular wave to the DP load signal described in Fig. 12. The triangular wave has a peak-to-peak amplitude of 2000 kW, an offset of 1000 kW, and a ramp of 5kW/s.

In the simulation, genset 1 (DG1) is running constantly and genset 2 (DG2) is started and stopped according to the load power demand. The start and stop limits are given in Table 4. When running on one genset, DG1, it is on the 100% frequency control ($K_1 = 0$, $K_2 = 1$). When DG2 is started, DG1 changes to 70% frequency control and 30% power control ($K_1 = 0.3$ and $K_2 = 0.7$). DG2 runs mainly in the power control mode ($K_1 = 0.7$), but it also participates in the frequency control by 30% ($K_2 = 0.3$). The genset parameters used in the simulation are given in Table 4.

Fig. 18 presents the AC network frequency, genset powers, and the BESS power during the start–stop simulation. The start and stop of genset 2 are visible in the network frequency. However, the change in frequency is less than 5%, and the frequency stays between 95% and 105% of the nominal frequency that the ship's PDS should be able to tolerate [24]. The frequency drops could be mitigated by ramping the power from one genset to another before shutting off the genset. In an actual vessel, these smooth start–stop functions would have to be in the power management system (PMS). Building the complete PMS into this simulation was beyond the scope of this paper.

D. FAULT CASES

Stability of an islanded grid is often studied by dropping generators off the grid or by introducing load spikes to the grid [26]. Malfunction of the BESS inverter and a genset fault during DP operation were simulated to study the stability of the grid. The DP load power data given in Fig. 12 were used in both fault case simulations.

First, a BESS failure was simulated. In the simulation, the OSV is in the DP mode and running one genset and the BESS. The genset is 100% in the frequency control mode. The power reference for the BESS is formed using two P-controllers: one for the frequency and one for the SOC of the battery, as shown in Fig. 1. A BESS failure occurs at

TABLE 5. Genset parameters before and after the BESS failure

Unit	Parameter	Before fault	After fault
DG1	K_1	0	0.3
	K_2	1	0.7
DG2	K_1	n/a	0.7
	K_2	n/a	0.3

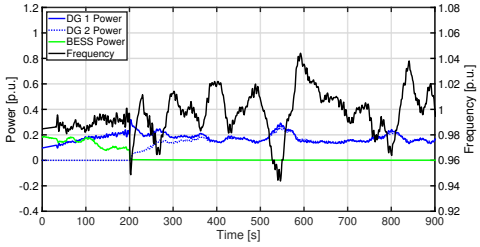

FIGURE 19. Genset and BESS power and AC network frequency during the BESS fault simulation. The fault occurs at t = 200 s.

$t = 200s$. The BESS is disconnected from the PDS and Genset 2 is started. During the fault, isochronous control parameters change as shown in Table 5.

The AC network frequency, genset powers, and the BESS power in the BESS malfunction simulation are presented in Fig. 19. The figure shows that the AC network frequency fluctuates less when the BESS is in operation. The BESS and Genset 1 share the load, but as the SOC of the BESS decreases slowly, the power reference for the BESS falls slowly. The fault occurs at $t = 200s$, Genset 2 starts to produce power immediately. In this simulation, it was assumed that Genset 2 is already running synchronized to the grid with a zero power reference in order to be able to start producing power quickly, if required, for example in critical DP operations. Gensets 1 and 2 go to isochronous load sharing according to Table 5. When a BESS fault occurs, the dynamic response of the one running genset is insufficient to respond to the load power changes caused by the DP operation, and therefore, a second genset must be started, even though the rated power of one genset should be sufficient to produce the power required for the DP operation. The AC frequency drops to around 0.95 p.u. when the BESS fault occurs. Despite the fault, the load power remains as the DP operation load power depicted in Fig. 12. Load shedding could be done in a fault situation on an actual vessel to reduce the load on the remaining gensets and the risk of a blackout [25].

The second fault case simulates a genset fault during DP operation. The OSV is performing the DP operation using DG1 and the BESS. At $t = 200s$, DG1 develops a fault and shuts down. DG2 starts immediately and continues operation in the 100% frequency control mode ($K_1 = 0$ and $K_2 = 1$). The BESS provides the required power during

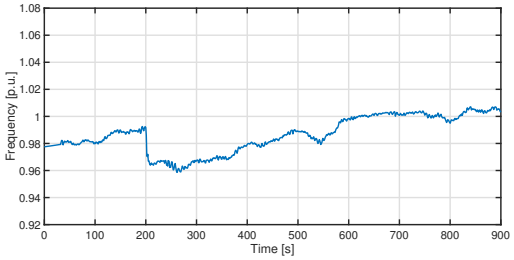

FIGURE 20. AC network frequency during genset failure simulation. The fault occurs at t = 200 s.

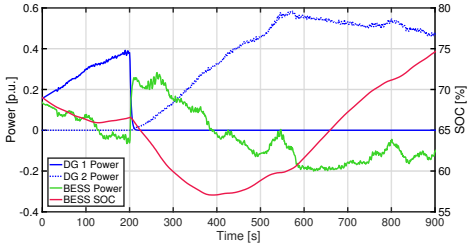

FIGURE 21. Genset and BESS power and BESS SOC during the genset failure simulation. The fault occurs at t = 200 s.

TABLE 6. Mean and variance of the AC network frequency in different simulations

Figure	Case	Mean	Variance
13	Isoch. w/o BESS case 1	0.9962	1.3971e-4
13	Isoch. w/o BESS case 2	0.9975	0.9557e-4
13	Isoch. w/o BESS case 3	0.9968	1.3607e-4
13	Isoch. w/o BESS case 4	0.9083	9,6966e-4
15	With BESS avg. pwr. estim.	0.9936	1.9714e-4
15	With BESS isochronous	0.9763	0.6692e-4
18	Start-stop	0.9970	1.2608e-4

the genset switch. This simulation, too, assumes that DG2 is already synchronized to the network and running on a zero power reference in order to start producing power quickly, if required.

The AC network frequency during the malfunction simulation is presented in Fig. 20 and the genset and BESS power in Fig. 21. Figs. 20 and 21 show that the genset fault causes a less than 0.03 p.u. drop in the frequency, mainly because the BESS can start feeding power to the network very quickly while the DG2 is ramping up. When the DG2 power rises high enough, the BESS starts charging, because its SOC setpoint is 80%. The BESS is able to participate in the PDS frequency control while charging by changing its charging power.

V. CONCLUSIONS

The power system control performance of an offshore supply vessel (OSV) was investigated using model-based simulation and real dynamic positioning (DP) load power data from an actual vessel. The effect of a battery energy storage system (BESS) on the dynamic performance was also analyzed.

Isochronous control was used for the gensets. Isochronous control and average load power estimation were investigated as methods for the power sharing control of a BESS. The parameter sensitivity of the isochronous control with and without a BESS was studied using average load power estimation and isochronous control to form a power reference for the BESS.

Simulation results obtained without a BESS showed that although one genset is enough to produce the power required for the DP operation, the dynamic response of the genset is not fast enough to respond to load changes. Consequently, the vessel has to run two gensets, each on a smaller load to be able to keep its position.

A BESS was added to the vessel to change the dynamic response of the vessel power output. If the vessel is already equipped with the isochronous genset control, the BESS can be controlled using either the average load power estimation or the isochronous control. In the simulations, the average load power estimation produced a slightly higher variance in the AC network frequency than when using isochronous control. However, under the average load power estimation control, the BESS was able to compensate load fluctuations with smaller AC frequency changes than when operating under the isochronous control.

Two fault cases were also studied. A BESS fault while the vessel is in DP operation was first simulated. As a response to the malfunction, the vessel had to start another genset and modify the isochronous control parameters to move into two-genset isochronous control with equal load sharing. The second fault case was a genset fault during DP operation. As a result of the malfunction, the vessel had to rely on battery power for the short period of time required to start and ramp up the second genset. In this case, it was assumed that the spare genset was already running on a zero power reference and synchronized to the network.

In the BESS fault simulation, the AC frequency dropped to 95% of the nominal frequency for a short period of time. It should, however, be noted that no load shedding was implemented in the simulation, which would be possible on an actual vessel to prevent a blackout. After the BESS malfunction, the second genset was started and the DP operation continued. The change in the system dynamics could be observed from the AC frequency as it fluctuated more without the BESS.

In the genset fault simulation, the fault caused a less than 0.03 p.u. drop in the AC frequency. The system was powered by the BESS while the second genset ramped up. The AC frequency remained within 0.95 p.u. to 1.05 p.u. In this simulation either, load shedding was not implemented.

Based on the results of this study, it can be concluded that all the investigated methods can be used for the BESS power control. The average power estimation method is good for peak shaving, because it reacts immediately to any change in the total load power. Isochronous control might be the easiest method to implement on a vessel already using isochronous control for gensets. While using isochronous control for the BESS, the State-of-Charge (SOC) of the battery must be managed by the power management system (PMS) by modifying the power reference for the BESS. Even when charging, the BESS can take part in the frequency control by changing its charging power. The start–stop method is a modification of isochronous control for the BESS. The start–stop method is able to start and stop gensets according to the load power and modify the isochronous control parameters according to the current configuration. The start–stop method is using the BESS to compensate load fluctuations in the power distribution system (PDS), and it is able to modify the BESS power reference to charge the battery when needed.

REFERENCES

[1] O, Mo, G. Guidi, "Design of Minimum Fuel Consumption Energy Management Strategy for Hybrid Marine Vessels with Multiple Diesel Engine Generators and Energy Storage", in ITEC, 2018.
[2] V. Shagar, S. G. Jayasinghe, H. Enshaei, "Effect of Load Changes on Hybrid Shipboard Power Systems and Energy Storage as a Potential Solution: A Review", Inventions, vol. 2, no. 3, 2017, doi. 10.3390/inventions2030021.
[3] T. I. Bø, A. R. Dahl, T. A. Johansen, E. Mathiesen, M. R. Miyazaki, E. Pedersen, R. Skjetne, A. J. Sørensen, L. Thorat, K. K. Yum, "Marine Vessel and Power Plant System Simulator", IEEE Access, vol. 3, pp. 2065-2079, doi. 10.1109/ACCESS.2015.2496122, 2015.
[4] A. Lana, A. Pinomaa, P. Peltoniemi, J. Lahtinen, T. Lindh, J.-H. Montonen, K. Tikkanen, "Methodology of Power Distribution System Design for Hybrid Short Sea Shipping", IEEE TIE, vol. 66, no. 12, pp. 9591-9600, Dec, 2019, doi. 10.1109/TIE.2019.2892665.
[5] T. I. Bø, T. A. Johansen, "Battery Power Smoothing Control in a Marine Electric Power Plant Using Nonlinear Model Predictive Control", IEEE TCST, vol. 25, no. 4, pp. 1449-1456, Jul, 2017, doi. 10.1109/TCST.2016.2601301.
[6] L. C. Raveendran, R. G. Devika, "Power fluctuation reduction scheme in marine power plants", in WiSPNET, Mar, 2017, pp. 2037-2040, doi. 10.1109/WiSPNET.2017.8300119.
[7] J. Hou, J. Sun, H. F. Hoffman, "Mitigating Power Fluctuations in Electric Ship Propulsion With Hybrid Energy Storage System: Design and Analysis", IEEE JOE, vol. 43, no. 1, pp. 93-107, 2018, doi. 10.1109/JOE.2017.2674878.
[8] J. Hou, J. Sun, H. F. Hoffman, "Battery/flywheel Hybrid Energy Storage to mitigate load fluctuations in electric ship propulsion systems", in ACC, 2017, pp. 1296-1301, doi. 10.23919/ACC.2017.7963131.
[9] Z. Jingnan, Z. Ying, "Control Strategy of Hybrid Energy Storage System in Ship Electric Propulsion", in ICMA, 2018.
[10] Yi Guo, M. M. S. Khan, M. O. Faruque, K. Sun, "Fuzzy logic based energy storage supervision and control strategy for mvdc power system of all electric ship", in PESGM, 2016.
[11] K. Kwon, D. Park and M. K. Zadeh, "Load Frequency-Based Power Management for Shipboard DC Hybrid Power Systems," 2020 IEEE 29th International Symposium on Industrial Electronics (ISIE), 2020, pp. 142-147, doi: 10.1109/ISIE45063.2020.9152418.
[12] A. Veksler, T. A. Johansen, R. Skjetne, E. Mathiesen, "Thrust Allocation With Dynamic Power Consumption Modulation for Diesel-Electric Ships", IEEE TCST, vol. 24, no. 2, pp. 578-593, 2016.
[13] International Maritime Organization, "Guidelines for Vessels with Dynamic Positioning Systems", Jun, 1994.
[14] T. A. Johansen, T. I. Bö, E. Mathiesen, A. Veksler, A. J. Sörensen, "Dynamic Positioning System as Dynamic Energy Storage on Diesel-

Electric Ships", IEEE TPWRS, vol. 29, no. 6, pp. 3086-3091, Nov, 2014, doi. 10.1109/TPWRS.2014.2317704.
[15] M. R. Miyazaki, A. J. Sørensen, N. Lefebvre, K. K. Yum and E. Pedersen, "Hybrid Modeling of Strategic Loading of a Marine Hybrid Power Plant With Experimental Validation," in IEEE Access, vol. 4, pp. 8793-8804, 2016, doi: 10.1109/ACCESS.2016.2629000.
[16] X. Shi, Y. Wei, J. Ning, M. Fu, D. Zhao, "Optimizing adaptive thrust allocation based on group biasing method for ship dynamic positioning", in ICAL, Aug, 2011, pp. 394-398, doi. 10.1109/ICAL.2011.6024750.
[17] A. Lana, K. Tikkanen, T. Lindh, J. Partanen, "Control of directly connected energy storage in diesel electric vessel drives", in EPE/PEMC, 2012.
[18] Woodward, Governing Fundamentals and Power Management.
[19] M. Järvisalo, "Keskitehoestimaattorin lisääminen diesel-sähkoiseen hybridijärjestelmään", M.Sc. Thesis, LES, LUT, Lappeenranta, 2014.
[20] Wärtsilä Finland Oy, "Wärtsilä 34DF Product Guide". Available: www.wartsila.com/docs/default-source/product-files/engines/df-engine/product-guide-o-e-w34df.pdf
[21] R. Pöllänen, "Converter-flux-based current control of voltage source PWM rectifiers - analysis and implementation", Ph. D. Thesis, Lappeenranta University of Technology (LUT), Lappeenranta, 2003.
[22] J. Ollila, "The space vector control of the PWM-rectifier using U/F references", in EPE, Trondheim, Norway, Sep, 1997.
[23] P. Peltoniemi, "Phase voltage control and filtering in a converter-fed single-phase customer-end system of the LVDC distribution network", Ph. D. Thesis, Lappeenranta University of Technology (LUT), Lappeenranta, 2010.
[24] DNV GL, "Rules for classification, Part 3: Surface ships, Chapter 3: Electrical installations", Dec, 2015, [ONLINE] Available: https://rules.dnvgl.com/docs/pdf/DNVGL/RU-NAVAL/2015-12/DNVGL-RU-NAVAL-Pt3Ch3.pdf.
[25] T. I. Bø, T. A. Johansen, "Scenario-based fault-tolerant model predictive control for diesel-electric marine power plant", in MTS/IEEE OCEANS, Bergen, Norway, 2013.
[26] K. Kanimozhi and M. V. Kirthiga, "Stability analysis of islanded micro-grids," 2016 IEEE International Conference on Power Electronics, Drives and Energy Systems (PEDES), 2016, pp. 1-6, doi: 10.1109/PEDES.2016.7914420.

JAN-HENRI MONTONEN received the M.Sc.degree in electrical engineering from the Lappeenranta University of Technology (LUT), Lappeenranta, Finland, in 2012. He is engaged in teaching and research of control engineering, automation and digital systems with LUT. His research interests include virtual simulation and intelligent control of electrically driven mechatronic systems.

TUOMO LINDH received the B.Sc. degree in mechatronics from the Mikkeli Institute of Technology, Mikkeli, Finland, in 1989, and the M.Sc. and D.Sc. degrees in technology from the Lappeenranta University of Technology, Lappeenranta, Finland, in 1997 and 2003, respectively. Since 1997, he has been with the Lappeenranta University of Technology, where he is currently an Associate Professor. His research interests include generator and motor drives and system engineering, particularly in the areas of distributed power generation, electric vehicles, and mechatronics.

ANDREY LANA received the M.S.E.E. degree from ETU (LETI), St. Petersburg, Russian Federation, in 2000 and received the M.Sc. and the D.Sc. degree in E.E. from Lappeenranta University of Technology (LUT), Lappeenranta, Finland in 2008 and 2014. Since 2014, he has worked as full researcher at Lappeenranta University of Technology. His current research interests include power system modelling and simulation, optimization of a hybrid propulsion power systems, microgrid protection and control.

PASI PELTONIEMI (M'09) received his M.Sc and D.Sc degrees in electrical engineering from Lappeenranta University of Technology (LUT), Finland in 2005 and 2010, respectively. From 2010 to 2014 he was a post-doctoral researcher and associate professor from 2015 to 2019 at LUT, Laboratory of Control Engineering and Digital Systems. He became in associate professor in power electronics in 2019 at LUT Laboratory of Electrical Drives. His areas of interests include modelling and control of power electronic applications such as dc microgrids, renewable generation, power-to-gas, grid-connected converters and electric drives.

ANTTI PINOMAA received the M.Sc. and D.Sc. degrees in electrical engineering from the Lappeenranta University of Technology (LUT), Lappeenranta, Finland, in 2009 and 2013, respectively. His main areas of interests include Information and communication technologies (ICT) in energy systems, smart grids, microgrid technologies, off-grid systems, and application of 4G LTE wireless IoT systems integrated with renewable energy sources, and those applications and system platforms covering fields from smart villages to smart cities.

KYÖSTI TIKKANEN received the M.Sc. degree in electrical engineering from the Lappeenranta University of Technology (LUT), Lappeenranta, Finland, in 2012. Since 2012, he has been working as Project Engineer with the laboratory of Department of Electrical Engineering at LUT. His responsibilities include designing and testing of emulation and measurement setups. His interests include control and system engineering, and energy efficiency measurements.

OLLI PYRHÖNEN (M'14) received the M.Sc. and D.Sc. degrees in Electrical Engineering in 1990 and 1998 from Lappeenranta University of Technology (LUT), Finland. He has been Professor in Applied Control Engineering since 2000 at LUT. In 2010 he received further teaching and research responsibility in the wind power technology at LUT. He has gained industrial experience as a R&D Engineer at ABB Helsinki in 1990-1993 and as a CTO of The Switch in 2007-2010. His main research fields are modelling and control of electrical drives and other energy conversion systems.

ACTA UNIVERSITATIS LAPPEENRANTAENSIS

1018. MÄNDMAA, SIRLI. Financial literacy in perspective – evidence from Estonian and Finnish students. 2022. Diss.

1019. QORRI, ARDIAN. Measuring and managing sustainable development in supply chains. 2022. Diss.

1020. MARTIKAINEN, SUVI-JONNA. Meaningful work and eudaimonia: contributing to social sustainability in the workplace. 2022. Diss.

1021. MANNINEN, KAISA. Conducting sustainability target-driven business. 2022. Diss.

1022. LI, CHANGYAN. Design, development, and multi-objective optimization of robotic systems in a fusion reactor. 2022. Diss.

1023. CHOUDHURY, TUHIN. Simulation-based methods for fault estimation and parameter identification of rotating machines. 2022. Diss.

1024. DUKEOV, IGOR. On antecedents of organizational innovation: How the organizational learning, age and size of a firm impact its organizational innovation. 2022. Diss.

1025. BREIER, MATTHIAS. Business model innovation as crisis response strategy. 2022. Diss.

1026. FADEEV, EGOR. Magnetotransport properties of nanocomposites close to the percolation threshold. 2022. Diss.

1027. KEPSU, DARIA. Technology analysis of magnetically supported rotors applied to a centrifugal compressor of a high-temperature heat pump. 2022. Diss.

1028. CHAUHAN, VARDAAN. Optimizing design and process parameters for recycled thermoplastic natural fiber composites in automotive applications. 2022. Diss.

1029. RAM, MANISH. Socioeconomic impacts of cost optimised and climate compliant energy transitions across the world. 2022. Diss.

1030. AMADI, MIRACLE. Hybrid modelling methods for epidemiological studies. 2022. Diss.

1031. RAMÍREZ ANGEL, YENDERY. Water-energy nexus for waste minimisation in the mining industry. 2022. Diss.

1032. ZOLOTAREV, FEDOR. Computer vision for virtual sawing and timber tracing. 2022. Diss.

1033. NEPOVINNYKH, EKATERINA. Automatic image-based re-identification of ringed seals. 2022. Diss.

1034. ARAYA GÓMEZ, Natalia Andrea. Sustainable management of water and tailings in the mining industry. 2022. Diss.

1035. YAHYA, MANAL. Augmented reality based on human needs. 2022. Diss.

1036. KARUPPANNAN GOPALRAJ, SANKAR. Impacts of recycling carbon fibre and glass fibre as sustainable raw materials for thermosetting composites. 2022. Diss.

1037. UDOKWU, CHIBUZOR JOSEPH. A modelling approach for building blockchain applications that enables trustable inter-organizational collaborations. 2022. Diss.

1038. INGMAN, JONNY. Evaluation of failure mechanisms in electronics using X-ray imaging. 2022. Diss.

1039. LIPIÄINEN, SATU. The role of the forest industry in mitigating global change: towards energy efficient and low-carbon operation. 2022. Diss.

1040. AFKHAMI, SHAHRIAR. Laser powder-bed fusion of steels: case studies on microstructures, mechanical properties, and notch-load interactions. 2022. Diss.

1041. SHEVELEVA, NADEZHDA. NMR studies of functionalized peptide dendrimers. 2022. Diss.

1042. SOUSA DE SENA, ARTHUR. Intelligent reflecting surfaces and advanced multiple access techniques for multi-antenna wireless communication systems. 2022. Diss.

1043. MOLINARI, ANDREA. Integration between eLearning platforms and information systems: a new generation of tools for virtual communities. 2022. Diss.

1044. AGHAJANIAN MIANKOUH, SOHEIL. Reactive crystallisation studies of CaCO3 processing via a CO2 capture process: real-time crystallisation monitoring, fault detection, and hydrodynamic modelling. 2022. Diss.

1045. RYYNÄNEN, MARKO. A forecasting model of packaging costs: case plain packaging. 2022. Diss.

1046. MAILAGAHA KUMBURE, MAHINDA. Novel fuzzy k-nearest neighbor methods for effective classification and regression. 2022. Diss.

1047. RUMKY, JANNATUL. Valorization of sludge materials after chemical and electrochemical treatment. 2022. Diss.

1048. KARJUNEN, HANNU. Analysis and design of carbon dioxide utilization systems and infrastructures. 2022. Diss.

1049. VEHMAANPERÄ, PAULA. Dissolution of magnetite and hematite in acid mixtures. 2022. Diss.

1050. GOLOVLEVA, MARIA. Numerical simulations of defect modeling in semiconductor radiation detectors. 2022. Diss.

1051. TREVES, LUKE. A connected future: The influence of the Internet of Things on business models and their innovation. 2022. Diss.

1052. TSERING, TENZIN. Research advancements and future needs of microplastic analytics: microplastics in the shore sediment of the freshwater sources of the Indian Himalaya. 2022. Diss.

1053. HOSEINPUR, FARHOOD. Towards security and resource efficiency in fog computing networks. 2022. Diss.

1054. MAKSIMOV, PAVEL. Methanol synthesis via CO2 hydrogenation in a periodically operated multifunctional reactor. 2022. Diss.

1055. LIPIÄINEN, KALLE. Fatigue performance and the effect of manufacturing quality on uncoated and hot-dip galvanized ultra-high-strength steel laser cut edges. 2022. Diss.

LUT University

ISBN 978-952-335-892-8
ISBN 978-952-335-893-5 (PDF)
ISSN 1456-4491 (Print)
ISSN 2814-5518 (Online)
Lappeenranta 2022